PUCRS

**PROGRAMA DE PÓS-GRADUAÇÃO EM
ENGENHARIA ELÉTRICA**

SAMARA OLIVEIRA PINTO

PHANTOM-BASED STRATEGY FOR THE OPTIMIZATION OF FDG PET BRAIN IMAGING RECONSTRUCTION

Porto Alegre
2022

Pontifícia Universidade Católica
do Rio Grande do Sul

PONTIFÍCIA UNIVERSIDADE CATÓLICA DO RIO GRANDE DO SUL
PROGRAMA DE PÓS-GRADUAÇÃO EM ENGENHARIA ELÉTRICA

SAMARA OLIVEIRA PINTO

PHANTOM-BASED STRATEGY FOR THE OPTIMIZATION OF FDG PET BRAIN IMAGING RECONSTRUCTION

Porto Alegre
2022

SAMARA OLIVEIRA PINTO

PHANTOM-BASED STRATEGY FOR THE OPTIMIZATION OF FDG PET BRAIN IMAGING RECONSTRUCTION

Dissertação apresentada como requisito para a obtenção do título de Mestre em Engenharia Elétrica pelo Programa de Pós-Graduação em Engenharia Elétrica da Pontifícia Universidade Católica do Rio Grande do Sul, área de concentração de Sinais, Sistemas e Tecnologia da Informação, linha de pesquisa em Engenharia Biomédica.

Orientadora: Dra. Ana Maria Marques da Silva
Co-orientador: Dr. Paulo Rauli de Vasconcelos Caribé

Porto Alegre
2022

Ficha Catalográfica

P659p Pinto, Samara Oliveira

Phantom-based strategy for the optimization of FDG PET brain imaging reconstruction / Samara Oliveira Pinto. – 2022.
90.
Dissertação (Mestrado) – Programa de Pós-Graduação em Engenharia Elétrica, PUCRS.

Orientadora: Profa. Dra. Ana Maria Marques Da Silva.
Co-orientador: Prof. Dr. Paulo Rauli de Vasconcelos Caribé.

1. Brain PET. 2. reconstruction optimization. 3. quantification. 4. image quality. I. Da Silva, Ana Maria Marques. II. Caribé, Paulo Rauli de Vasconcelos. III. Título.

Elaborada pelo Sistema de Geração Automática de Ficha Catalográfica da PUCRS
com os dados fornecidos pelo(a) autor(a).
Bibliotecária responsável: Clarissa Jesinska Selbach CRB-10/2051

PHANTOM-BASED STRATEGY FOR THE OPTIMIZATION OF FDG PET BRAIN IMAGING RECONSTRUCTION

CANDIDATA: SAMARA OLIVEIRA PINTO

Esta Dissertação de Mestrado foi julgada para obtenção do título de MESTRE EM ENGENHARIA ELÉTRICA e aprovada em sua forma final pelo Programa de Pós-Graduação em Engenharia Elétrica da Pontifícia Universidade Católica do Rio Grande do Sul.

DRA. ANA MARIA MARQUES DA SILVA – ORIENTADORA

DR. PAULO RAULI DE VASCONCELOS CARIBÉ – COORIENTADOR

BANCA EXAMINADORA

Prof. Dr. Rafael Garibotti

Prof. Dr. Marcelo Tatit Sapienza

“Life is about taking risks. If you never persist, you will never achieve
your dreams.” Mayara Benatti

A vida é sobre correr riscos. Se você nunca persiste, nunca
conquistará seus sonhos. (tradução nossa)

AGRADECIMENTOS

Meus primeiros agradecimentos vão para os meus pais, Soeli e Daniel, que sempre me motivaram e me inspiraram a ser uma pessoa melhor, e a estudar cada vez mais. Só tenho gratidão à Deus por ter me dado a oportunidade de ser filha de pessoas tão dignas e honestas, com valores tão especiais.

Gostaria de expressar meu agradecimento a dedicação dos professores da Pós-Graduação em Engenharia Elétrica que mesmo neste período conturbado de pandemia, não mediram esforços para manter a excelência das aulas, mesmo que online, foram tempos desafiadores e de muito aprendizado.

Agradeço à minha orientadora, prof. Ana Maria Marques da Silva por sempre me guiar por toda minha trajetória acadêmica, como uma ótima mestra e conselheira. Seu apoio foi, sem dúvida, essencial para minha formação acadêmica. Obrigada por sempre acreditar no meu potencial e me apoiar.

Não poderia deixar de agradecer uma pessoa muito especial, que além de ser meu amigo, é meu colega de profissão, Lucas Narciso. Meus mais sinceros agradecimentos por todo apoio, suporte e colaboração, sem você seria impossível realizar esse trabalho.

Gostaria de agradecer ao meu noivo, Bruno Andrade, que sempre me deu todo suporte, amor, carinho e compreensão. Gratidão por sempre estar ao meu lado, me motivando e apoiando todas as minhas escolhas. Agradeço a Deus por ter me dado a oportunidade de compartilhar a minha vida com um ser humano tão especial.

Agradeço aos demais familiares, amigos e colegas que mesmo de longe sempre torceram pelo meu sucesso. *Por fim, a Coordenação de Aperfeiçoamento de Pessoal de Nível Superior (CAPES) pela bolsa integral de estudos que possibilitou minha dedicação exclusiva a este mestrado - Código de Financiamento 001.*

ABSTRACT

Background: Positron emission tomography (PET) imaging with [^{18}F]FDG provides valuable information regarding the underlying pathological processes in neurodegenerative disorders, such as Alzheimer's disease (AD). PET imaging in these populations should be as short as possible to limit head movements and to improve patient comfort. Image reconstruction protocol optimization is usually performed by acquiring images from an anthropomorphic phantom and assessing both image quality and quantification accuracy.

Objective: To develop and validate a phantom-based optimization strategy for [^{18}F]FDG-PET imaging reconstruction to reduce acquisition time while maintaining adequate quantification accuracy and image quality.

Methods: [^{18}F]FDG-PET images of a Hoffman 3D brain phantom were acquired. Optimization strategies were developed to obtain images with no apparent quality loss and adequate quantification accuracy in the analyzed regions. Analytical and iterative reconstruction methods were compared by means of image quality and quantitative accuracy metrics. Lastly, the optimized reconstruction protocol was evaluated in [^{18}F]FDG-PET retrospective data acquired from healthy individuals and AD patients.

Results: Phantom study: OSEM reconstruction algorithm was optimized (4 iterations and 32 subsets). It resulted in remarkably similar images compared to the current clinical settings, with a 50% reduction in scan time (5 min with a post-reconstruction filter of 4 mm). Clinical study: Quantification and image quality metrics were similar between optimized and clinical protocols, and no significant differences between protocols were observed. Two experienced physicians visually assessed the images in terms of noise, contrast, and overall image quality. No difference between protocols was identified by the physicians.

Conclusion: Shortening the acquisition time is therefore possible by optimizing image reconstruction parameters while maintaining adequate quantification accuracy and image quality. The optimized protocol obtained in this study was assessed in human data and presented comparable results to those of the clinical protocol.

Keywords: *Brain PET; reconstruction; optimization; quantification; image quality*

.

RESUMO

Introdução: A imagem de tomografia por emissão de pósitrons (PET) com [^{18}F] FDG fornece informações valiosas sobre os processos patológicos subjacentes em doenças neurodegenerativas, como a doença de Alzheimer (DA). As aquisições de imagens PET nessas populações devem ser as mais curtas possíveis para limitar os movimentos da cabeça e melhorar o conforto do paciente. A otimização de protocolos de reconstrução é usualmente realizada através da análise de imagens adquiridas com fantomas antropomórficos, ambos em termos de qualidade de imagem e acurácia de quantificação.

Objetivo: Desenvolver e validar uma estratégia de otimização baseada em fantoma para reconstrução de imagem [^{18}F]FDG-PET para reduzir o tempo de aquisição, mantendo a precisão de quantificação adequada e qualidade de imagem.

Métodos: Imagens PET adquiridas com [^{18}F]FDG de um fantoma cerebral 3D Hoffman foram adquiridas. Estratégias de otimização foram desenvolvidas, de forma a obter imagens sem perda aparente de qualidade e com precisão de quantificação adequada nas regiões analisadas. Métodos de reconstrução analíticos e iterativos foram comparados por meio de métricas de qualidade de imagem e precisão quantitativa. Por fim, o protocolo otimizado foi testado em dados retrospectivos de PET adquiridos com [^{18}F]FDG de indivíduos saudáveis e pacientes com a DA.

Resultados: Estudo do fantoma: O algoritmo de reconstrução OSEM foi otimizado (4 iterações e 32 subconjuntos), o que resultou em imagens semelhantes em comparação com as configurações clínicas atuais, com uma redução de 50% no tempo de varredura (5 min com um filtro pós-reconstrução de 4 mm). Estudo clínico: As métricas de quantificação e qualidade de imagem foram semelhantes entre o protocolo otimizado e o protocolo clínico, e não foram observadas diferenças significativas entre eles. Dois médicos experientes avaliaram visualmente as imagens em termos de ruído, contraste e qualidade geral da imagem. Nenhuma diferença entre os protocolos foi identificada pelos médicos.

Conclusão: A diminuição do tempo de aquisição é possível através da otimização dos parâmetros de reconstrução da imagem, mantendo a acurácia de quantificação e qualidade de imagem adequadas. O protocolo otimizado obtido nesse trabalho foi implementado em dados clínicos e apresentou resultados comparáveis com aqueles adquiridos com o protocolo clínico.

Palavras-chave: *Imagens de PET cerebrais; reconstrução; otimização; quantificação; qualidade de imagem.*

LIST OF FIGURES

LIST OF TABLES

LIST OF ABREVIATIONS

^{18}F	Flúor-18
AD	Alzheimer’s disease
Bq	Becquerel
Ci	Curie
CSF	Cerebrospinal fluid
CNR	Contrast-to-noise ratio
COV	Coefficient of variant
CT	Computer Tomography
C_{true}	True activity concentration
FBP	Filtered-backprojection
FOV	Field of view
FT	Fourier transform
FWHM	Full-width at half-maximum
GE	General Electronics
GM	Gray matter
kg	Kilogram
LOR	Line-of-response
MADP	Mean absolute percentage difference
mL	Milliliter
ML-EM	Maximum-likelihood expectation-maximization
MMSE	Mini-Mental State Exam
MRI	Magnetic resonance imaging
OSEM	Ordered subset expectation maximization
NEC	Noise-equivalent counts
PET	Positron emission tomography
PSF	Point spread function
PVE	Partial volume effect
RC	Recovery coefficient or contrast recovery
ROI	Region of interest
SNR	Signal-to-ratio
RMSE	Root-mean-square error
SUV	Standardized uptake value

SUVR	Standardized uptake value ratio
TV	Total variation
VOI	Volume of interest
WB	Whole brain
WM	White matter

SUMMARY

1 INTRODUCTION

Nuclear medicine is a medical imaging modality that provides metabolic and functional information *in vivo,* often non-invasively in the format of dynamic or static images, which represent the volumetric distribution of a given radiopharmaceutical (SAHA, 2015). These images relate tracer uptake in the tissue of interest to underlying physiology, such as metabolism. Positron emission tomography (PET) is an imaging modality within nuclear medicine that has extensive applicability in oncology, cardiology, and neurology (BAILEY et al., 2005). PET scans can be combined with magnetic resonance imaging (MRI) or, more commonly, X-ray computed tomography (CT) to provide additional anatomical information required for diagnostic purposes (SAHA, 2015).

For decades, PET brain imaging has been widely used to study brain disorders, such as neurodegenerative diseases, dementia, epilepsy, neurodevelopmental and psychiatric disorders (BANATI et al., 2000; CHAUVEAU et al., 2008; PORTNOW; VAILLANCOURT; OKUN, 2013). Diagnosis of brain disorders with PET is accomplished by using specific radiotracers and analyzing brain activity (PORTNOW; VAILLANCOURT; OKUN, 2013). In addition, PET is a quantitative technique with the potential to assess disease severity and progression (HERHOLZ, 2014). One of the most commonly used radiotracers is [^{18}F]-labeled fluorodeoxyglucose ([^{18}F]FDG), which can be used to identify early signs of neuronal changes (SHOKOUHI; RIDDLE; KANG, 2017). [^{18}F]FDG is an irreversibly bound tracer that provides direct or indirect glucose consumption measurements (i.e., energy production), such as the cerebral metabolic rate of glucose (SAHA, 2015).

In aging, cognitive decline is common, and it is usually aggravated due to the presence of some neurodegenerative diseases, such as Alzheimer's Disease (AD) (HAMDAN; BUENO, 2005). An increase in dementia cases in the elderly population is expected over time, bringing to light the need for better ways for early detection and preventing symptoms. It is estimated that there are around 50 million people with AD in the world (PATTERSON, 2018). In Brazil, there are about 1.2 million cases, most of them still without a medical diagnosis. (ASSOCIAÇÃO BRASILEIRA DE ALZHEIMER, 2021). AD is the most common form of dementia associated with aging, affecting millions of elderly people worldwide. It is characterized by progressive impairment, affecting cognition, memory, and executive functions (HAMDAN; BUENO, 2005).

Although PET is valuable in assessing changes in brain function in a wide range of neurodegenerative diseases (FILIPPI et al., 2012), the first tool implemented in the clinic is a neuropsychological assessment, with mini-mental state exam (MMSE) being the most commonly used test (AREVALO-RODRIGUEZ et al., 2015). However, PET imaging can be effective in diagnosing dementia cases as [^{18}F]FDG PET brain imaging is an early indicator of neuronal changes (SHOKOUHI; RIDDLE; KANG, 2017). In AD, low-uptake regions in the brain are due to glucose metabolism impairment caused by synaptic loss and selective neuronal death (MASTERS et al., 2015). The cognitive decline observed in AD is associated with regional reductions in cortex volume and abnormalities in the connections between brain regions (WEINER et al., 2017). AD patients demonstrate predominant hypoperfusion in the temporoparietal regions, including the precuneus and the posterior cingulate cortex (MINOSHIMA et al., 2001). However, quantification of low-uptake regions is challenging, particularly due to low signal-to-noise ratio (SNR) and partial volume effects (PVEs) that affect the detectability of small lesions (KREMPSER; DE OLIVEIRA; DE ALMEIDA, 2012; LIM; DEWARAJA; FESSLER, 2018).

Illes et al. (2007) suggest that imaging techniques aimed at AD patients should be comfortable, fast, and efficient, as these patients often have difficulties tolerating medical procedures. The ideal imaging technique should include short acquisition protocols that make it easier for patients to remain still during the exam (ILLES et al., 2007). Moreover, head movement during PET acquisition is an issue that clinicians and researchers often address to improve tracer pharmacokinetics quantification accuracy. These movements are particularly relevant in the elderly population, with increased significance in patients with dementia or movement disorders (WARDAK et al., 2010). Thus, a scan time reduction in the AD population is important to limit head movements, with the additional advantage of increasing patient comfort (ILLES et al., 2007; WARDAK et al., 2010). Optimized reconstruction methods are typically required to reduce scan time while maintaining adequate image quality and quantification accuracy in low-uptake regions.

In the literature, there are studies aiming at developing new reconstruction algorithms for low counting PET data (VERHAEGHE; READER, 2010; WALKER et al., 2011). Other studies focus on reducing radiotracer dose and evaluate the reliability of using low activity injections for a range of radioisotopes, such as ^{18}F, ^{11}C, ^{90}Y,^{15}O and, ^{44}Sc (CARLIER et al., 2015; JIAN; PLANETA; CARSON, 2015; LIM; DEWARAJA; FESSLER, 2018; LIMA et al., 2020; WALKER et al., 2011). Moreover, the effect of low counting statistics have been investigated in studies with physical phantom (AKERELE et al., 2018; BOUSSE et al., 2020; CARLIER et al., 2015; JIAN; PLANETA; CARSON, 2015; KASTIS et al., 2010; LIM; DEWARAJA; FESSLER, 2018; LIMA et al., 2020; MURRAY et al., 2010; POLYCARPOU;

TSOUMPAS; MARSDEN, 2012; SHEIKHBAHAEI et al., 2016; TAHAEI; READER; COLLINS, 2019) and simulated data (KASTIS et al., 2015; TAHAEI; READER; COLLINS, 2019), for cardiac (AKERELE et al., 2018; BOUSSE et al., 2020; LIM; DEWARAJA; FESSLER, 2018) and oncological applications (BOUSSE et al., 2020). The optimization of brain PET image reconstruction algorithms in AD with the aim of reducing acquisition time and integrating both quantification accuracy and image quality (i.e., visual analysis performed by experienced physicians) is a valuable research topic; however, to this date, no such study has been found.

The aim of this work is to identify optimized reconstruction parameters of [^{18}F]FDG-PET image reconstruction parameters in order to reduce acquisition time while maintaining adequate quantification accuracy and image quality. For this, [^{18}F]FDG-PET images were acquired of a Hoffman 3D brain phantom, and image quality parameters and quantitative accuracy were evaluated for different reconstruction algorithms and settings. Optimization strategies were developed to obtain images with no apparent quality loss and adequate quantification accuracy. Lastly, clinical [^{18}F]FDG-PET data were retrospectively reconstructed with the optimized reconstruction algorithm and compared to the current clinical practice settings.

2 RATIONALE

Patient motion during image acquisition can cause significant artifacts leading to a image quality reduction, which is a difficult problem for PET imaging systems (YITZHAKY; KOPEIKA, 1997). Such artifacts can affect visual assessment and uptake quantification, which is harmful both to diagnosis and image-guided radiotherapy (SARIKAYA; SARIKAYA, 2021; XU; YUAN; YE, 2011). Motion blur degrades images by affecting quantitation accuracy (e.g., the standard uptake value, or SUV), reducing spatial resolution and tumor to-background contrast, distorting the shape and location of the tumor and overestimating tumor size (NEHMEH et al., 2002; SARIKAYA; SARIKAYA, 2021; VISVIKIS et al., 2004; XU; YUAN; YE, 2011).

Comfortable, fast, and efficient exam acquisition techniques are essential for patients with difficulty tolerating medical procedures, including rapid acquisition protocols (ILLES et al., 2007). Not only reducing PET acquisition time increases patient comfort, but reduces the chances of movement, which, in turn, avoids image blurring and loss of quantification accuracy, as discussed above. However, a consequence of the time reduction is low count data, which increase the noise in the reconstructed image and can impact quantification accuracy. The reliability of quantification can be improved during image reconstruction by implementing iterative reconstruction techniques, such as the ordered-subset expectation-maximization (OSEM), when compared to analytical algorithms (BOELLAARD, 2009; BUVAT, 2007; SAHA, 2015). However, the accuracy of iterative algorithms is affected by low-count statistics (VAN SLAMBROUCK et al., 2015; WALKER et al., 2011) and OSEM suffers from noise-induced bias (BOELLAARD; VAN LINGEN; LAMMERTSMA, 2001).

Studies have proposed new reconstruction algorithms specially designed for low-counting PET images (BOUSSE et al., 2020; BYRNE, 1998; LIM; DEWARAJA; FESSLER, 2018; NUYTS et al., 2002), compared their performances to conventional reconstruction methods (AKERELE et al., 2018; KASTIS et al., 2015; SHEIKHBAHAEI et al., 2016; SHEKARI et al., 2017; TAHAEI; READER; COLLINS, 2019; VERHAEGHE; READER, 2010; WALKER et al., 2011) and evaluated post-reconstruction parameters (POLYCARPOU; TSOUMPAS; MARSDEN, 2012; TAHAEI; READER; COLLINS, 2019). These studies evidence the possibility to optimize PET reconstruction parameters to obtain suitable images for the diagnosis, even with low count statistics (i.e., reduction in injected activity or acquisition time). Thus, this study was carried out to optimize [^{18}F]FDG PET image reconstruction parameters in order to reduce acquisition time while maintaining adequate quantification accuracy and image quality.

2.1 OBJECTIVES

The general objective of this work is to develop and evaluate a phantom-based optimization strategy for [^{18}F]FDG-PET brain imaging reconstruction to allow the acquisition time or dose reduction, while maintaining adequate quantification accuracy and image quality.

The specific objectives are:

- To evaluate the image quality and quantification accuracy of brain PET images reconstructed with different algorithms using a Hoffman 3D brain phantom.
- To evaluate the image quality and quantification of reconstruction settings for clinical [^{18}F]FDG-PET brain imaging using the phantom-based results, with shorter acquisition times.
- To validate the proposed optimized clinical reconstruction settings for retrospective patient data of individuals diagnosed with Alzheimer's disease and healthy controls.

3 THEORETICAL FRAMEWORK

3.1 PET IMAGING

PET is an imaging technique that uses in vivo radiotracers especially used for cancer treatment planning and staging, and cardiac and neurological diagnosis (CHERRY; SORENSON; PHELPS, 2012). In PET, the radionuclide employed emits a positron particle (β^+) that loses its kinetic energy after emission due to the collisions with the nearby atoms. It interacts with an electron after traveling a few millimeters and forms the positronium, with a very short half-life. Then, it annihilates by transforming their masses into energy in the form of two 511 keV gamma photons (CHERRY; SORENSON; PHELPS, 2012). PET acquisition consists of coincidence detection of the almost collinear (~180°) annihilation photons by detectors positioned in a circular ring around the field of view (FOV), where the annihilation site is located based on the time difference between the two detections. A true event to generate the PET image is recorded when it is within the coincidence window interval—usually 6 to 12 ns (CHERRY; SORENSON; PHELPS, 2012). If the true coincidence event is recorded, the PET image can be mathematically reconstructed from the raw data collected during the scanning.

Several physical factors can influence the image quality in PET, such as attenuation, scattering, positron range, and non-collinearity. Positron range is the distance traveled by the positron before the positron-electron annihilation occurs, and it can impact image quality by the mismatch between detected and real emission locations (CHERRY; SORENSON; PHELPS, 2012). Additionally, the two annihilation photons can be emitted with a small non-collinearity ($180 \pm 0.5^\circ$ from each other); consequently, the exact location where the annihilation occurred is unknown (CHERRY; SORENSON; PHELPS, 2012). These effects cause blurring in the reconstructed image and limit the spatial resolution.

Several corrections are necessary before, during, and after the image reconstruction to obtain PET/CT images (BOELLAARD, 2009; TONG; ALESSIO; KINAHAN, 2010b). Normalization, decay, dead time, random coincidences, attenuation, and scattering are the most usually applied corrections. Normalization is the process necessary to correct for variations due to different gains of photomultiplier tubes and disparities in detector efficiency (CHERRY; SORENSON; PHELPS, 2012). Deadtime is the time required for the processing of the two 511 keV photons. During this process, the detection system is unable to process other events, which are usually lost. Therefore, dead time corrections must be applied during data reconstruction. Otherwise, the radioactivity concentration is underestimated for high counting rates, since as the dead time increases with the counting rate (CHERRY; SORENSON; PHELPS, 2012; DAHLBOM, 2017).

The detection of two 511 keV photons in a coincidence window forms the basis of PET imaging. However, it is possible to detect two photons, not from the same annihilation but detected within a line-of-response (LOR). This event, called random coincidence, provides an erroneous location of the annihilation position, which can cause artifacts and increase the noise in the reconstructed image (CHERRY; SORENSON; PHELPS, 2012; SAHA, 2015).

Depending on the photon energy and the radioactive distribution, a percentage of the emitted photons will be attenuated, i.e., will interact with the tissue and will be either fully absorbed or scattered at a certain angle. The attenuation must be corrected because it can cause distortion and increase image noise, information loss, and non-uniformity (BUSHBERG, 2002; CHERRY; SORENSON; PHELPS, 2012). The mathematical methods for attenuation correction depend on a linear attenuation coefficients map (CHERRY; SORENSON; PHELPS, 2012; DAHLBOM, 2017). Commonly, CT is used to generate the attenuation coefficients map used to correct for attenuation in the PET emission data. Scattering occurs when the photon loses energy proportionally to the angle formed between the original and the deflected paths (TARANTOLA; ZITO; GERUNDINI, 2003). It can affect the reconstructed image by the occurrence of artifacts, reducing contrast, and introducing quantification errors (BUVAT, 2007).

All the problems mentioned above show some of the challenges related to PET imaging, and adequate corrections should be incorporated into reconstruction algorithms to provide accurate quantification results. Moreover, quantification accuracy can be affected by both PVE and low SNR. PVE is due to the limited spatial resolution of the PET equipment and corresponds to an apparent loss of activity in a region compared to its surroundings (DE ARAÚJO; ANDRADE; DA SILVA, 2018; KREMPSER; DE OLIVEIRA; DE ALMEIDA, 2012). The low SNR in PET images is due to the limited sensitivity of the detection system (DE ARAÚJO; ANDRADE; DA SILVA, 2018). Low-uptake regions must also be carefully evaluated, as iterative methods include the additional restriction of not allowing for negative values during image reconstruction (GONZÁLEZ; MOINELO, 2010; GREZES-BESSET et al., 2007; JIAN; PLANETA; CARSON, 2015; TORRICO, 2012; WALKER et al., 2011). Such restriction will overestimate the activity concentration of regions with low activity concentration.

3.2 PET IMAGE ACQUISITION

PET images can be acquired dynamically, from the radiopharmaceutical administration to its excretion or stabilization, or statically, which represent the accumulation of events in a fixed time interval. List-mode is one of the ways to acquire data images, where all coincidence events are recorded continuously throughout the acquisition. From the list-mode file, the user can specify how data should be stored in each time frame, allowing post-acquisition flexibility in terms of reconstruction options. This acquisition mode is especially important when the most appropriate temporal sampling has not yet been identified, as in the case of tracers that are not yet consolidated in clinical practice (YODER, K., 2013).

Static images are a (Figure 1A) acquired in a single frame in an acquisition time interval chosen by the user and are mainly used in clinical applications due to their feasibility (i.e., reasonable costs and easy patient management). The main areas of application are in oncological and cardiac imaging (BERTOLDO; RIZZO; VERONESE, 2014). In dynamic PET (Figure 1B), it is possible to observe the behavior of radiotracer uptake in the tissue of interest over time. Usually, the acquisition starts before the administration of the radiopharmaceutical (or together with the injection) so that the entire imaging time is registered in the acquisition (YODER, K., 2013).

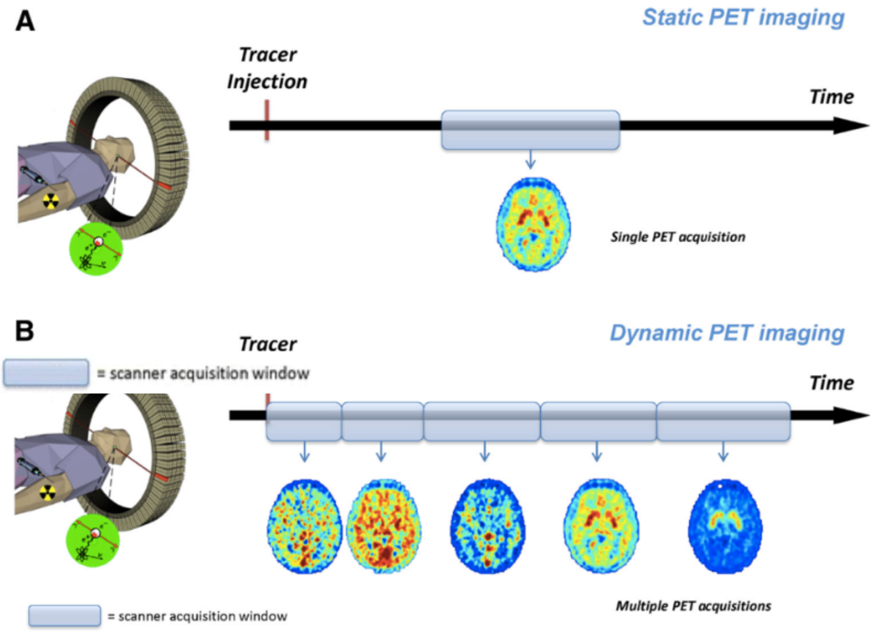

Figure 1: Static and dynamic PET image acquisition. (A) Static PET image. The events are registered over a single fixed time interval. (B) Dynamic images. The events are registered at multiple time intervals, resulting in 4D matrices. Source: This figure was reproduced from Bertoldo; Rizzo; Veronese (2014), *Clin Transl Imaging,* with permission provided by Elsevier and Copyright Clearance Center.

3.3 PET IMAGE RECONSTRUCTION

PET image reconstruction algorithms are commonly divided into three major groups: rebinning, analytical and iterative algorithms (BRINKS; BUZUG, 2007).

3.3.1 ANALYTICAL RECONSTRUCTION ALGORITHMS

Analytical algorithms assume that the PET acquisition data is noise-free and try to find a direct mathematical solution for the image from the known projections (TONG; ALESSIO; KINAHAN, 2010b). The most used analytical method for PET data reconstruction is the filtered-backprojection (FBP), which consists of projecting the raw data across the image matrix. Once a sinogram is created, an image of the tracer distribution can be mathematically obtained, as shown in Figure 2.

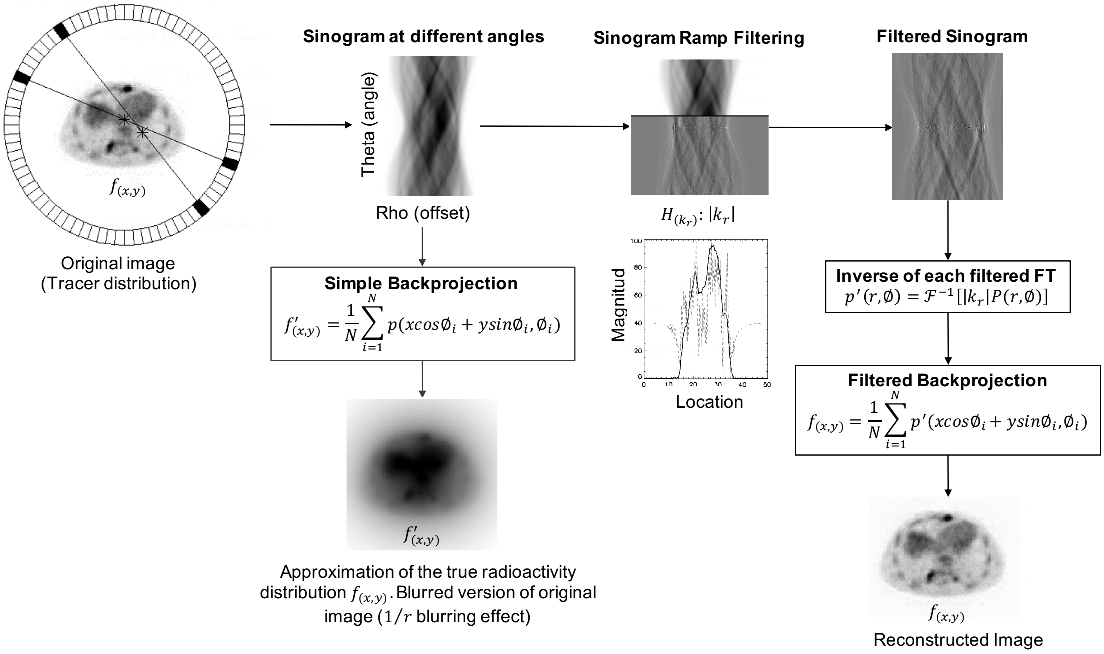

Figure 2: Difference between the simple and the filtered backprojection. Illustration of the difference between the simple and the filtered backprojection. Projections are generated from the scanned object (original image, $f(x,y)$) and combined into sinograms. The simple backprojection results in a blurred approximation ($f'(x,y)$) of the original image. The blurring effect is minimized by applying a ramp filter ($H_{(k_r)}$) using a modified Fourier transform (FT) for each projection ($p'(r,\phi)$). Then, each $p'(r,\phi)$ is backprojected to produce an image that better represents the object. The reconstruction process ends with the inverse FT, returning to the spatial domain. Source: (CARIBE, 2020)

After backprojection, an approximation of the radioactivity distribution within the slice ($f'_{(x,y)}$) is obtained by Eq. (1)

$$f'_{(x,y)} = \frac{1}{N}\sum_{i=1}^{N} p_i(x\cos\phi_i + y\sin\phi_i\,, \phi_i) \tag{1}$$

where p is the i^{th} projection in the angle ϕ_i, and $f'_{(x,y)}$ denotes an approximation to the true radioactivity distribution, $f_{(x,y)}$. The simple backprojection suffers from the blurring effect, resulting in unsatisfactory tomographic images where the final image is a blurred approximation of the original image (CHERRY; SORENSON; PHELPS, 2012). This can be minimized by applying a ramp filter ($H_{(k_r)}$) to the data, usually combined with another smoothing filter, which is then backprojected to produce an image that better represents the object. First, the ramp filter, $H_{(k_r)}$ which is given by $P'H_{(k_r)} = |k_r|PH_{(k_r)}$ is applied in the Fourier space by a modified Fourier transform (FT) for each projection ($p'(r,\phi)$) .Then, the inverse FT is performed to obtain $f_{(x,y)}$ (Eq. (2) (CHERRY; SORENSON; PHELPS, 2012).

$$p'(r,\phi) = \mathcal{F}^{-1}\{|k_r|P(r,\phi)\} \tag{2}$$

where $P_{(K_r,\emptyset)}$ is the FT of the unfiltered projection, and $|k_r|$ is applying a ramp filter.

3.3.2 ITERATIVE RECONSTRUCTION ALGORITHMS

Iterative reconstruction methods use information from both the PET system and physical processes to incorporate the required corrections into the reconstruction algorithm (SAHA, 2015). Iterative methods are based on the attempt to maximize (or minimize) a cost function that determines the similarity (or difference) between the estimated and the best images obtained by the algorithm. The goal is achieved after a given number of iterations composed of analytical processes (TARANTOLA; ZITO; GERUNDINI, 2003).

OSEM is an iterative algorithm widely used in PET, which is an advanced version of the maximum-likelihood expectation-maximization (ML-EM) method (HUDSON; LARKIN, 1994). OSEM consists of a method that organizes the data into subsets of projections uniformly distributed throughout the scanned volume, allowing for a faster convergence (TONG; ALESSIO; KINAHAN, 2010b). In OSEM, image is updated for each subset during each iteration. Therefore, the number of updates is the product of iterations and projections subsets. As the number of updates increases, the spatial resolution increases; however, with increasing noise, requiring an optimization process where the smoothing filter, number of iterations, and number of subsets are properly balanced to obtain optimal image quality (SLOMKA et al., 2009). The number of chosen subsets determines the convergence acceleration; however, the greater the iterations-subsets product, the greater the noise in the final reconstructed image (TONG; ALESSIO; KINAHAN, 2010b). Thus, it is necessary to optimize the number of subsets and iterations when OSEM is applied to PET data, as the algorithm might never converge to a solution, while the noise increases with each iteration (HUDSON; LARKIN, 1994). Figure 3 shows the workflow of the OSEM reconstruction method.

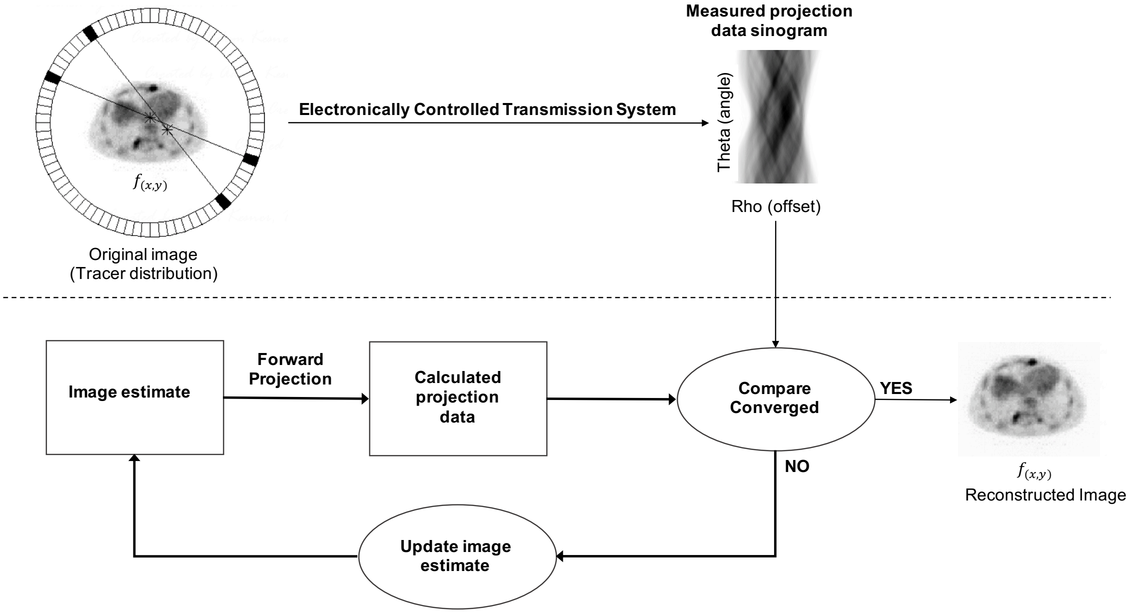

Figure 3: Iterative reconstruction scheme. First, an initial image is estimated, and its projections are calculated by forwarding the projection. Then, they are compared to the measured profiles (from the original image) until the reconstruction algorithm converges, and the reconstructed image is generated. Source: (CARIBE, 2020)

The OSEM technique divides the data into several subsets following a certain order, in which Eq. (3) is applied.

$$\hat{f}_j^{(k+1)} = \frac{\hat{f}_j^{(k)}}{\sum_{m\in S_o} h_{m,j}} \sum_{i\in S_o} h_{ij} \frac{p_i}{\sum_n h_{i,n}\, \hat{f}_n^{(k)}} \tag{3}$$

where f is the image under reconstruction, k is the iteration number, i the LOR index, j, m, n the voxel indices, S_o the subset and h is the system matrix. The ratio $p_i/\left(\sum_n h_{in}\, \hat{f}_n^{(k)}\right)$ represents the comparison between estimated and measured projections, where the denominator is the forward projection that gives an estimate of the measured data (p_i). Thus, the term $\sum_{i\in S_o} h_{ij}\left(p_i/\left(\sum_n h_{in}\, \hat{f}_n^{(k)}\right)\right)$ represents the error of the backprojection into the image space.

Lastly, the backprojected data is normalized by $\sum_{m \in S_o} h_{mj}$. The backprojection is only performed for the projection data belonging to a subset S_o and a different subset is selected at each update (CARIBE, 2020).

Although iterative methods provide better image quality, resolution, and less noise, when compared to analytical methods, they introduce an overestimation in the quantification regions where the activity concentration is less than 4 μCi/ml (148 kBq/ml) (GONZÁLEZ; MOINELO, 2010; LIM; DEWARAJA; FESSLER, 2018; TORRICO, 2012). When these regions correspond to areas of hypometabolism in PET brain images, this quantification error can be significant and impact the diagnosis of certain brain disorders (GREZES-BESSET et al., 2007; VERHAEGHE; READER, 2010).

3.3.3 REBINNING RECONSTRUCTION ALGORITHMS

Rebinning algorithms convert the 3-D data into sets of 2-D sinograms, and then analytical or iterative reconstruction algorithms are applied. This process significantly reduces data storage and computing requirements. However, one limitation of rebinning algorithms is the occurrence of spatial distortion and noise amplification (BRINKS; BUZUG, 2007; TONG; ALESSIO; KINAHAN, 2010b). The most accurate rebinning algorithm commercially available nowadays is the Fourier rebinning, or FORE (TARANTOLA; ZITO; GERUNDINI, 2003).

3.3.4 POINT SPREAD FUNCTION CORRECTION

Measuring the point spread function (PSF) of the system and accounting for it in the reconstruction algorithm can improve the spatial resolution of the final image (RAPISARDA et al., 2010). In PET, the spatial resolution is limited by the size of each crystal element, and the circular geometry of the detector ring introduces a spatial distortion away from the center of the detector (CHERRY; SORENSON; PHELPS, 2012). Photons produced in the center of the scanner are detected and localized with a smaller error than those produced on the edges of the FOV, as the photon strikes the crystals at an angle and is likely to travel to a neighboring crystal, contributing to the spatial distortion (AKAMATSU et al., 2016; VENNART et al., 2017). General Electronics (GE) have corrected for this spatial distortion using the methodology proposed by Alessio et al. (ALESSIO et al., 2010) and measuring a point source at several million points across the FOV and then incorporating the measured response into the sinogram space (ALESSIO et al., 2010; VENNART et al., 2017) (TONG; ALESSIO; KINAHAN, 2010a). The GE “Sharp IR” (commercial name) software provides a PSF correction algorithm, which includes a more accurate projection of the detector geometry.

3.4 IMAGE QUANTIFICATION

Quantitative [^{18}F]FDG-PET is increasingly being recognized as an important tool for diagnosis, determination of prognosis, and response monitoring in oncology, due to its accurate and less observer-dependent measurement when compared to visual inspection alone (BOELLAARD, 2009). Various quantitative measures can be derived from [^{18}F]FDG-PET studies (HOEKSTRA et al., 2000); however, in the analysis of static images, only semiquantitative information can be obtained (YODER, K., 2013). The most common semiquantitative measure is SUV (in g/mL, Eq. (4)), which represents the [^{18}F]FDG uptake within a region, measured over a certain time interval after administration, normalized by the injected dose per body weight (i.e., it takes into account distribution throughout the whole body) (BOELLAARD, 2009). The use of SUV is valid with the assumption that the radioactive material was distributed evenly throughout the body (YODER, K., 2013).

$$SUV = \frac{C_{VOI}}{A_{inj}/m_{subj}} \tag{4}$$

where C_{VOI} is the activity concentration in the region under analysis, A_{inj} the injected activity, and m_{subj} the subject weight.

Another form of semiquantification is the ratio of SUV values, namely SUVR (Eq. (5)), between the tissue of interest and the reference region (BAILEY et al., 2005).

$$SUVR = \frac{SUV_{ROI}}{SUV_{REF}} = \frac{C_{ROI}}{A_{inj}/m_{subj}} \bigg/ \frac{C_{REF}}{A_{inj}/m_{subj}} = \frac{C_{ROI}}{C_{REF}} \tag{5}$$

where C_{REF} is the activity concentration in the reference region.

Beyond SUV and SUVR, other quantification parameters are used to describe the differences between the true activity and the measurements extracted from images. Specifically for phantom experiments, the measured-to-true activity concentration ratio, also known as contrast recovery or recovery coefficient (RC), is given by Eq. (6). It represents the fraction of the true activity concentration (C_{true}, in Bq/mL) present in the final image, which is calculated as the injected activity divided by the volume of water in the phantom, after correcting for decay and residual activity in the syringe.

$$RC = \frac{C_{VOI}}{C_{true}} \tag{6}$$

where C_{VOI} is the measured activity concentration (in Bq/mL) in a volume-of-interest (VOI).

In brain images, the gray-to-white matter activity concentration ratio is calculated using Eq. (7). This measurement is referred to as contrast, and WM is considered the background region.

$$Contrast = \frac{C_{GM}}{C_{WM}} \tag{7}$$

where C_{GM} and C_{WM} are the GM and WM mean activity concentrations, respectively.

Finally, quantification bias describes the difference between measured and expected activity concentrations. In this work, the percentage difference relative to the expected activity concentration at full statistics count-level (10 min) was used to estimate bias (YAN et al., 2016), as given by Eq. (8):

$$Bias(\%) = 100 * \frac{C_{meas} - C_{exp}}{C_{exp}} \tag{8}$$

where C_{exp} and C_{meas} represent the expected and measured activity concentration in a VOI.

3.5 IMAGE QUALITY

Image quality can be assessed using metrics such as coefficient of variation (COV), SNR, and contrast-to-noise ratio (CNR). Data variability can be measured by the COV, which is calculated as the ratio between the STD and the mean activity concentration. SNR and CNR are given by Eqs. (9) and (10), respectively. The latter is related to the visual ability to detect a small lesion (CARLIER et al., 2015).

$$SNR = \frac{C_{GM} - C_{WM}}{STD_{WM}} \tag{9}$$

$$CNR = \frac{RC}{COV} \tag{10}$$

where STD_{WM} is the WM standard deviation, which is considered the background region.

Although the idea that noise increases while contrast decreases with higher number of iterations and lower filter is a known fact, the analysis performed in our study shows the tendency of both parameters and provides knowledge to understand the effect of these two components in the CNR of the image. We have selected the CNR value as the most important parameter and the maximization of this metric was performed to optimize the reconstruction parameters. This approach has been used previously in the literature. (AKAMATSU et al., 2012; PRIETO et al., 2015).

Lastly, diagnostic accuracy can be improved by constructing Z-score maps, showing patterns of significant deficits (FÄLLMAR et al., 2016) The Z-score defines the deviation of a sample with respect to the mean of a distribution.

4 STATE OF THE ART

To establish state of the art related to the optimization of brain [^{18}F]FDG PET image reconstruction parameters using different algorithms, a bibliographic search for full papers was carried out in two databases: PubMed and Web of Science. We used as filters: inclusion of complete papers published in the last twelve years (since 2009) in English. The keywords used for both databases were: ((PET) AND (FDG) AND ((brain) OR (Hoffman) OR (cerebral)) AND ((quantification) OR (image quality)) AND ((optimization) OR (time reduction) OR (dose reduction)) NOT (SPECT) NOT (kinetic modeling) NOT (input function) NOT (deep learning)). A total of 52 articles were found in PubMed, and 31 articles were found in Web of Science. Excluding repeated articles, a total of 60 articles were deeply analyzed. A spreadsheet was created, where unrelated articles were discarded. To this date, 16 articles have been included in the state-of-the-art section (Table *1*).

Several authors have been developing and evaluating new reconstruction algorithms specially designed for optimizing PET images (ELLIS; READER, 2018), comparing the performance of different reconstruction methods using PSF to conventional reconstruction methods (NAGAKI; ONOGUCHI; MATSUTOMO, 2014; PRIETO et al., 2015; REYNÉS-LLOMPART et al., 2018; VANHOUTTE et al., 2019; WAMPL et al., 2017), assessing optimization strategies in evaluation and treatment of childhood epilepsy (SHKUMAT; VALI; SHAMMAS, 2020), investigating dose reduction (FÄLLMAR et al., 2016; SAGARA et al., 2021), evaluating new dedicated brain PET scanners (CABRERA-MARTÍN et al., 2021), or implementing different optimizations in a multicentre study (IKARI et al., 2016).

The image reconstruction methods usually are validated by performing phantom experiments (AKAMATSU et al., 2016; IKARI et al., 2016; PRIETO et al., 2015; REYNÉS-LLOMPART et al., 2018; SORET et al., 2020; VANHOUTTE et al., 2019; WAMPL et al., 2017), using simulated (ELLIS; READER, 2018), or clinical data (AKAMATSU et al., 2016; BEHR et al., 2018; CABRERA-MARTÍN et al., 2021; ELLIS; READER, 2018; FÄLLMAR et al., 2016, 2018; NAGAKI; ONOGUCHI; MATSUTOMO, 2014; REYNÉS-LLOMPART et al., 2018; SAGARA et al., 2021; SCHILLER et al., 2019; SHKUMAT; VALI; SHAMMAS, 2020; SORET et al., 2020; VANHOUTTE et al., 2019; WAMPL et al., 2017), and/or assessing image quality by experienced physicians (BEHR et al., 2018; CABRERA-MARTÍN et al., 2021; FÄLLMAR et al., 2018; REYNÉS-LLOMPART et al., 2018; SCHILLER et al., 2019; SHKUMAT; VALI; SHAMMAS, 2020; SORET et al., 2020). Lastly, some studies used ^{11}C in addition to ^{18}F (AKAMATSU et al., 2016; IKARI et al., 2016; PRIETO et al., 2015).

These studies presented different metrics for image evaluation, such as coefficient of variation (COV), recovery coefficient (RC), contrast-to-noise ratio (CNR), background variability (BV), noise-equivalent counts (NEC), standardized uptake value (SUV), standardized uptake value ratio (SUVR), root-mean-square error (RMSE), full-width at half-maximum (FWHM), mean absolute percentage difference (MADP), total variation (TV), bias, contrast, noise, spatial resolution, uniformity, true and random coincidence rates, random fraction, and Z-score.

Finally, the most relevant studies selected in this state of the art are described in more details in sub-section 4.1.

4.1 MOST RELEVANT STUDIES

Nagaki et al. (2014) investigated the rate count performance of PET scanners and the image quality with different combinations of high-resolution image reconstruction algorithms in [^{18}F]FDG PET brain. They analyzed the true and random coincidence rates, random fraction, and the NEC patient in brain and liver bed positions. The brain cortex image quality was quantitatively evaluated with respect to spatial resolution, contrast, and SNR. The results indicate that a high-resolution image reconstruction algorithm combined with baseline OSEM, PSF, and TOF, and without Gaussian filtering, is optimal for better image quality in [^{18}F]FDG PET brain. They acquired data from the Hoffman 3D phantom and reconstructed the images with TOF and PSF modeling. They concluded that the PSF is most effective for enhancing the image quality of the brain by improving the spatial resolution and SNR. Furthermore, the TOF improves SNR when incorporated into OSEM + PSF. Although using clinical PET data, the study did not perform any visual evaluation by clinicians.

Prieto et al. (2015) studied the influence of reconstruction algorithms and parameters on the PET image quality of brain phantoms, as well as the impact of an optimized reconstruction in clinical PET/CT brain studies. CNR, RC, and noise were calculated for different reconstruction algorithms, and they simulated the uptake of four different tracers: [^{18}F]FDG, [^{11}C]FMZ, [^{11}C]MET, and [^{18}F]FDOPA, using the 2D multi-compartment Hoffman phantom. The best algorithm for each tracer was selected by visual inspection. The maximization of CNR determined the optimal parameters for each reconstruction. The limitation of this study is that a single acquisition was used for all the reconstructions. Therefore, the uncertainty of the data has not been measured, and statistical analysis was not feasible. Moreover, the authors did not analyze clinical brain PET data.

Fällmar et al. (2016) proposed a protocol for [^{18}F]FDG PET brain with reduced radiation dose and preserved quantitative characteristics. The study consisted of performing two PET/CT image acquisitions on separate occasions, first with a normal dose, then with a low dose, and finally with an ultra-low dose. MRI data were acquired for all subjects. Images were spatially and intensity normalized. SUVR was calculated using an automated atlas, and values from the normal- and low-dose images were compared pairwise. No clinically significant bias was found in any of the three groups. The conclusion is that 0.75 MBq/kg (56 MBq for a 75-kg subject) is a sufficient [^{18}F]FDG dose for evaluating SUVR in brain PET scans in adults with or without neurodegenerative disease, resulting in a reduction of total PET/CT effective dose from 4.54 to 1.15 mSv. The ultra-low dose (0.5 mSv) could be useful in research studies requiring serial PET in healthy controls or children. Limitations of this study include the relatively small group size ($n = 22$) and the absence of normal-dose reproducibility. Additionally, absolute quantification, such as the cerebral metabolic rate of glucose, may result in a more accurate correlation. Thus, establishing the accuracy of low-dose protocols for the purpose of absolute quantification requires further studies. Finally, the study compared relatively large VOIs; therefore, the ability to detect small lesions with low-dose was not evaluated. Even with clinical PET images, they did not perform a visual evaluation of the image quality by physicians.

Behr et al. (2018) performed quantitative and visual assessments of the PET images acquired on TOF PET/MR and non-TOF PET/CT. The list-mode data acquired on a 3T PET/MRI scanner were reconstructed with a reduction of up to 94% of the original acquisition time. Semiquantitative measurements, such as SUV_{max} and SUV_{mean}, of normal tissues and lesions detected, were compared. Qualitative assessments between PET/CT and PET/MR images were performed by 3 physicians. A Likert-type scale between 1 and 5 was used: 1 for non-diagnostic, 3 for equivalent to PET/CT, and 5 for superior quality. The researchers found a significant difference between SUV_{max}, $SUV_{mean,}$ and SUV_{peak}. The SUV_{mean} values for normal tissues were lower in images acquired with 4, 2, 1, 0.5, and 0.25 min/bed on the PET/MR, while SUV_{max} and SUV_{peak} values in lesions were higher. The authors concluded that the high-sensitivity TOF PET showed comparable but still better visual image quality, even at a reduced activity concentration in comparison to the lower-sensitivity non-TOF PET. They obtained a seven-fold reduction in either injection dose (for the same scan time) or total scan time (for the same injected dose) to cover the whole body without compromising diagnostic performance. In terms of limitations to the study, the comparison of scanners with different spatial resolution, some acquisitions were not made 60 min post-injection, and the small patient population size. Lastly, the relative number of lesions was small, and bone or liver metastases were not included.

Soret et al. (2020) retrospectively simulated the reduction of injected [^{18}F]FDG activity in 100 patients (previously assessed for cognitive impairment) with simultaneous PET/MRI. A list-mode acquisition was used to generate a 20-min image set as a reference (PET_{STD}) and to simulate a low-dose injection with a 10-min image (PET_{LD}; 50% dose reduction). They tested the reproducibility between PET_{LD} and PET_{STD} in a blinded visual interpretation performed by two nuclear physicians who were asked to classify metabolic patterns and a quantitative analysis conducted with ROI. Moreover, voxel-wise comparisons between patients suggestive of AD and frontotemporal dementia (FTD) were performed. The intra-operator agreement was high between the PET_{STD} and PET_{LD} visual assessments for both readers (κ of 0.92 and 0.99), and SUVR values were strongly reproducible (intraclass correlation coefficient of 0.95). The voxel-wise and regional comparisons between AD vs. FTD metabolic profiles yielded very similar results with both PET_{STD} and PET_{LD}. The authors concluded that [^{18}F]FDG dose reduction is possible when performing 20-min brain PET/MRI without modifying diagnostic performance and quantitative assessments. Limitations of this study include the retrospective nature and the lack of quantification measurements.

Although previous studies evaluated quantification and/or image quality in the assessment of [^{18}F]FDG PET brain reconstruction algorithms, our study combined both analyses optimizing a reconstruction method with a physical phantom and validating the optimized parameters with clinical data. Our study aims to evaluate the accuracy and the image quality simultaneously, presenting a strategy to optimize the reconstruction algorithms using a physical brain phantom. We validated the optimized reconstruction parameters with retrospective clinical data of patients with AD and healthy individuals. Additionally, both sets of images were randomly and blindly presented to two experienced physicians. Image quality was scored (1-5; score 3 represented clinical image quality) in terms of image noise, contrast, and overall image quality.

Table 1: State of the art.

Authors (year)	**Tracer**	**Equipment**	**Types of Images**	**Reconstruction Algorithms**	**Evaluation Metrics**	**Visual Evaluation**	**Results/Conclusion**
NAGAKI; ONOGUCHI; MATSUTOMO, 2014	[^{18}F]FDG	PET/CT Biograph mCT (Siemens).	23 patients who underwent clinical whole-body for cancer screening	OSEM, GF, PSF, and TOF: OSEM, OSEM + GF, OSEM + TOF, OSEM + GF+TOF, OSEM + PSF, and OSEM + PSF + TOF models. For OSEM, OSEM + GF, and OSEM +PSF (3i24s). For OSEM + TOF, OSEM + GF+ TOF, and OSEM +PSF + TOF (2i21s). Smoothing filter GF 4 mm FWHM	Spatial resolution contrast SNR coincidence rates of true and random, random fraction, and the NEC patient in brain and liver bed positions.	No	♦ PSF improved spatial resolution and SNR by 11 and 53%, respectively ($P<0.01$), and TOF improved SNR by ~23% ($P<0.01$). ♦ Combining PSF and TOF is optimal for a better SNR. ♦ High true coincidence rates produce lower noise and improve image quality. ♦ PSF provides a significant improvement of higher spatial resolution and SNR, and TOF provides cumulative effect of SNR with the faster iterative convergence.
PRIETO et al., 2015	[^{18}F]FDG, [^{11}C]FMZ [^{11}C]MET, [^{18}F]FDOPA	PET/CT Biograph mCT (Siemens)	Phantom Hoffman	OSEM, OSEM + TOF, OSEM + PSF and OSEM + PSF + TOF.	CNR Contrast Noise	No	♦ Best algorithm selected by visual inspection. ♦ Maximization of CNR determined the optimal reconstruction parameters. ♦ In Hoffman 3D phantom, both noise and contrast increased with increasing number of iterations and decreased with increasing FWHM. ♦ Visual analysis of Hoffman 2D brain phantom suggested OSEM+PSF+TOF is the optimum algorithm (MET or FDOPA), and OSEM+TOF (FMZ).
IKARI et al., 2016	[^{18}F]FDG [^{18}F]-florbetapir [^{18}F]-flutemetamol [^{11}C]-PiB	Phantom data were acquired on 19 PET cameras from 15 PET centers that participated in the J-ADNI2 project Advance (GE) Eminence (Shimadzu) HeadtomeV (Shimadzu)	Phantom Hoffman and a cylindrical phantom	FORE + OSEM, 4i14s FORE + OSEM, 4i16s FORE + OSEM, 4i20s FORE + OSEM, 6i16s 3D-iteration, 4i16s 3D-iteration, 3i18s+PSF 3D-iteration, 3i32s+TOF	spatial resolution GM/WM contrast uniformity noise	No	♦ Multicenter study. Reconstruction parameters based on ADNI, J-ADNI, and other research and clinical trials or optimized based on phantom parameters. ♦ Phantom test criteria: (i) 8 mm FWHM or better resolution and (ii) GM/WM %contrast ≥55 % with the Hoffman 3D phantom and (iii) SD of 51 small ROIs ≤0.0249 (5% variation) for uniformity and (iv) image noise (SD/mean) ≤15 % for a large ROI with the uniform phantom.

		Biograph Hi-Rez (Siemens) Biograph True Point (Siemens) ECAT Accel (Siemens) Discovery690 (GE) HeadtomeV (Shimadzu)		HDE, FORE-DRAMA, filter cycle = 0, 4i			
FÄLLMAR et al., 2016	[^{18}F]FDG	PET/CT Discovery ST (GE) PET ECAT Exact HR (Siemens) 3T MRI scanner (Philips)	22 clinical data: 8 patients with neurodegenerative disorders and 14 controls normal-dose and 5 controls low-dose	OSEM 2i21s	SUVR Mean absolute differences per region	No	♦ 0.75 MBq/kg is a sufficient [^{18}F]FDG dose for SUVRs in brain PET with or without neurodegenerative diseases. ♦ ˜Reduction of PET/CT effective dose from 4.54 to 1.15 mSv. Ultra-low dose (0.5 mSv) could be useful in serial PET in healthy controls or children. ♦ [^{18}F]FDG dose can be reduced, without loss of diagnostic accuracy, by a factor of 4 in clinical practice and by a factor of 10 for multiple scans. ♦ Reduction of radiation burden to patients and staff.
AKAMATSU et al., 2016	[^{18}F]FDG [^{11}C]-PiB [^{18}F]-florbetapir [^{18}F]-flutemetamol	PET/CT Discovery-690 (GE)	Phantom Hoffman and a cylindrical pool phantom and 7 Human images 1 or 2 subjects for each tracer	OSEM with a variable number of iterations (1–16) and subsets (4–24). A Gaussian post-filter was applied to have FWHM of 0–8 mm.	spatial resolution GM/WM contrast, uniformity COV(%) SUVR	No	♦ Phantom images were reconstructed with 4i16s without post-smoothing for ^{18}F-condition. ♦ Optimal reconstruction got sufficient image quality (60-80 iterative updates with OSEM). ♦ Stable SUVR is a quantitative metric of amyloid deposition, supporting the feasibility of phantom criteria for standardization and harmonization [^{18}F]FDG and amyloid PET brain imaging for multicenter studies.
WAMPL et al., 2017	[^{18}F]FDG [^{18}F]FET	PET/CT Biograph-True-Point-True-View and PET/MR Biograph MR	Phantom and PET/CT 8 patients PET/MR 16 patients	3D-OSEM+PSF	RC SUV$_{max}$ RC$_{A50}$ SUV$_{A50}$,	No	♦ RCmax (phantom) and SUV$_{max}$ (patients) increased significantly when reducing the frame duration. ♦ Significantly lower deviations were observed for RC$_{A50}$ and SUV$_{A50}$.

			Both oncology patients				♦ For hybrid aminoacid brain imaging, frame duration (or injected activity) can be reduced to 30% STD used in clinical routine without significant changes on accuracy if adequate reconstruction settings and quantitative measures are used.
FÄLLMAR et al., 2018	[18F]FDG	Discovery ST (GE)	18 patients Control/AD/bvFTD/LBD/CBD	OSEM; 2 iterations, 21 subsets)	Z-scores	Readers viewed 2 sets of Z-maps (ND and LD from each subject). Readers analyzed consistency with the clinical diagnosis and subjective quantification between images (scale 0-5).	♦ Bland-Altman analysis showed a slight constant bias (0.206). ♦ Performance between normal- and low-dose were equal, both showing 72% sensitivity, 83% specifici,ty and 78% accuracy. ♦ Kappa values for inter-reader agreement were 0.778 for ND and 0.571 for LD. R ♦ In differential diagnoses, correct diagnoses were given in 67% of ND assessments, and in 56% of LD assessments (P=0.49).
ELLIS; READER, 2018	[18F]FDG	PET/CT Biograph mCT (Siemens)	Simulated data: brain tumor datasets and 1 patient with head and neck cancer	MLEM DS-PML DE-PML DTV-PML OSEM – real case	RMSE COV Bias SD TV	No	♦ Used a simultaneous difference-image-based PML reconstruction method previously published. ♦ Priors are designed to encourage longitudinal images with differences in: (a) low entropy (DE-PML), and (b) high sparsity in spatial gradients (DTV-PML). ♦ Proposed algorithms (DE-PML and DTV-PML) were compared with standard reconstructions (MLEM). ♦ Using any of the three priors with an appropriate penalty strength produced images with noise levels equivalent to standard reconstructions with increased counts levels. ♦ In tumors, methods produce subtly different results in tumor quantitation and reconstruction RMSE. ♦ In simulations, DE-PML produced tumor means in agreement with MLEM, while DTV-PML produced lowest errors due to noise reduction within the tumor. ♦ Appropriate choice of penalty term and strength allows noise reduction while

							maintaining reconstruction performance, in terms of quantitation of mean intensity via DE-PML, or in terms of tumor RMSE via DTV-PML.
REYNÉS-LLOMPART et al., 2018	$[^{18}F]$FDG	Discovery IQ (GE)	NEMA NU-2-2012 and 15 patients (five brain scans and 10 torso acquisitions)	OSEM+PSF 4i12s and a 4.8 mm FWHM filtering	RC BV Noise Contrast CNR COV SUV_{max} SUV_{mean}	Two nuclear medicine physicians. Reviewer ranked 0 to 4 (non-diagnostic to excellent) the lesion conspicuity and image quality in liver, mediastinum, lung, bone marrow, and overall scan. For brain, reviewer ranked with the same criteria the gyri and basal ganglia, and the overall image quality.	♦ Q.Clear quantification and optimization in patient studies depends on the activity concentration and lesion size. ♦ β increase represents a decrease in lesion contrast and noise. ♦ Increase in SNR, and similar steady CNR in phantom. ♦ As activity concentration or the sphere size increase, the optimal β increases. Similar results for clinical data. ♦ In subjective assessment, the optimal β for torso is 300-400, and from 100-200 for brain. ♦ Recommended torso β has texture indices coefficients of variation < 10%. ♦ Increase of CNR and SNR of Q.Clear depends on conditions and penalization factor. ♦ For Q.Clear in a BGO scanner, β equal to 350 for ^{18}F oncology and 200 for brain PET is the optimal value.
BEHR et al., 2018	$[^{18}F]$FDG	PET/CT Discovery VCT (GE) or Biograph Hi-Rez (Siemens). PET/ MRI SIGNA (GE).	15 patients scheduled for a clinically indicated whole-body $[^{18}F]$FDG PET/CT.	OSEM + TOF 2i28s	SUV_{max} SUV_{mean} SUV_{peak}	One physician with 30 y experience, one junior physician, and one nuclear medicine resident. Images were reviewed on OsiriX v8.0. MIP, axial, sagittal, and coronal and fused images. Scores between 1 (non-diagnostic), and 5 (significantly better quality than	♦ High-sensitivity TOF PET is comparable but has better visual image quality at reduced activity in comparison to lower-sensitivity non-TOF PET. ♦ Seven times reduction in either injection dose for the same time or total scan time for the same injected dose. ♦ Did not result in poorer lesion detection or visual image quality degradation ♦ Further dose/acquisition time reduction is possible with extended scan time for sub-mSv clinically acceptable [18F]FDG PET. ♦ Comparable visual quality and lesion SUV are possible in reduced PET acquisition (or reduced injected dose) when using high-sensitivity (23.3 cps/kBq) 400 ps TOF PET in comparison to lower-sensitivity (8.4 and 4.9 cps/kBq) non-TOF PET.

						PET/CT and/or new lesions)	♦ The images acquired with the TOF PET/MRI have better overall image quality when compared to f PET/CT.
VANHOUTTE et al., 2019	[^{18}F]FDG	PET/CT Biograph mCT-Flow (Siemens) PET/RM 3T Achieva scanner (Philips)	NEMA NU-2-body phantom and 35 early-onset Alzheimer's disease (EOAD) patients	OSEM + TOF 2i21s OSEM + TOF 6i21s OSEM + TOF + PSF 8i21s	RC RMSE MADP FWHM	No	♦ TOF has superior performance than TOF + PSF. ♦ EQ·PET' (Siemens) allows optimal lesion detection with harmonized SUV from a single dataset. ♦ EQ·PET succeeded in finding the optimal smoothing that minimized RMSE metrics calculated on human brain [^{18}F]FDG-PET of EOAD patients. ♦ EQ·PET minimize reconstruction-induced variabilities between brain [^{18}F]FDG-PET images. ♦ Moderate variabilities remained after harmonizing PSF reconstructions with standard non-PSF OSEM reconstructions, suggesting precautions should be taken when using PSF modeling.
SCHILLER et al., 2019	[^{18}F]FDG	PET/CT Gemini TF 64 3 - dimensional TOF (Philips)	AD (n = 13) patients and FTD (n = 12) patients	Vendor-specific line-of-response row-action maximum-likelihood algorithm with 3i33s.	Average values of SD within diagnostically VOIs from AAL template: frontal, temporal, and parietal regions, precuneus, and posterior cingulate cortex.	Three experienced readers, providing diagnostic certainty with positive and negative values for AD and FTD.	♦ SUVR was calculated as the average of each regional activity normalized by the mean activity of the cerebellar cortex using PMOD. ♦ VOI-based analyses using these normalized uptakes selected brain regions for the diagnosis of AD and FTD: the temporal, parietal, and frontal lobes and the precuneus and posterior cingulate cortex. ♦ Means and SDs were extracted and examined in terms of their dependence on reduced acquisition times. ♦ A reduction of acquisition time may be reduced by a factor of 4, and the

							administered activity may be reduced to 50 MBq (effective dose < 1 mSv).
SHKUMAT; VALI; SHAMMAS, 2020	[18F]FDG	PET/CT SiPM Discovery MI; (GE)	25 pediatric patients (0.5-16 years old) with epilepsy	OSEM (8i34s, filtro de corte Z de 4,5 mm, β = 0), and Q.Clear with varied penalization factor (β=200,β=350,β=500) use BSREM algorithm	No quantitative measures	Two pediatric nuclear medicine physicians. Reconstruction score for quality (noise, spatial resolution, artifacts), clinical parameters (cortex image quality, basal ganglia and thalamus), and overall (clinical acceptability).	♦ Clinical evaluation of pediatric ^{18}F-brain PET image quality is adequate at 40% reductions of count density using BSREM with a penalization factor β=350-500.
SORET et al., 2020	[18F]FDG	PET/ MRI SIGNA (GE).	Phantom Hoffman and 100 patients assessed for cognitive impairment or suspected neurodegenerative dementia	OSEM-3D+ TOF+PSF generate a 20-min image set as a reference (PETSTD -20min) and to simulate a low-dose injection with a 10-min image (PET$_{LD}$-10min).	SNR$_{WM}$ SNR$_{GM}$ SUV$_{WM}$ SUV$_{GM}$ SUV$_{GM}$/ SUV$_{WM}$ SUVR	Two nuclear medicine physicians	♦ 50 % reduction in [18F]FDG injected dose can be achieved for brain PET/MR imaging without loss of either diagnostic performance or change in duration of acquisition. ♦ Intra-operator agreement was high between the PETSTD and PET$_{LD}$ visual assessments (kappa 0.92 and 0.99). ♦ SUVR were strongly reproducible (intraclass correlation coefficient 0.95). ♦ The voxel-wise and regional comparisons between AD vs. FTD profiles yielded very similar results with PET$_{STD}$ and PET$_{LD}$. ♦ SPM analysis with PET$_{STD}$ revealed a significant metabolic decrease in precuneus, posterior cingulate, and bilateral posterior associative cortex in AD group (p G 0.05). With PET$_{LD}$, an additional but small cluster (0.24 ml) in the right parietal.
CABRERA-MARTÍN et al., 2021	[18F]FDG	whole-body PET/CT CareMiBrain (Oncovision)	40 patients with initial approach to diagnosis and monitoring of dementia	MLEM	CRC SNR Noise	Two nuclear medicine physicians analyzed in two steps (presence or not of a	♦ The study time was reduced from 25 min to < 10 min. ♦ Improvements allow reconstruction with a 0.5 mm, voxel size, achieving spatial resolution < 1.6 mm.

		and PET/CT Biograph True Point (Siemens)				pathology). Second step comparing the image quality (scores from 1 to 5).	♦ Improvements in the dynamic response of the equipment and in the general performance of the process. ♦ 20% increase in performance, raising the saturation point of the system and improving the zone of linear response of the equipment. ♦ Reduction of the processing time by up to 40% and in the ready mode format by 66%. ♦ Improvements in the search for coincidences, correction of the photopeak position, spectrums more stable and correctly centered, improvement of random estimation, and correction of dead time.
SAGARA et al., 2021	[^{18}F]FDG	PET/CT Discovery IQ (GE)	1,231 patients 624 cases with a fixed injection dose and 607 cases with an optimized injection dose based on body weight.	OSEM and Q. Clear	NEC density	No	♦ Effective radiation dose [^{18}F]FDG was calculated using 0.019 mSv/MBq conversion factor, ICRP 106. ♦ Body weight-based injection dose optimization decreased the effective dose by 11%, from 4.54 ± 0.1 mSv to 4.05 ± 0.8 mSv ($p < 0.001$). ♦ Image quality by NEC density was significantly improved by 10%, from 0.39 ± 0.1 to 0.43 ± 0.2 ($p < 0.001$). NEC density deteriorates when the effective dose is decreased. ♦ Body weight-based FDG injection dose optimization contributed to the reduction of effective dose and image quality improvement (50 and 69 kg). ♦ Optimization was not useful for subjects ≥ 70 kg. Image quality improved by extending the acquisition time rather than adjusting the injection dose. ♦ They did not examine the effects of dose optimization on the visual evaluation nor the interpretation of images.
This work	[^{18}F]FDG	PET/CT Discovery 600 (GE)	35 subjects 18 AD patients and 17 healthy individuals and	FBP, FORE+FBP, OSEM, OSEM+PSF	CNR SNR Noise SUVR RC COV	Two nuclear medicine physicians. Scores between 1 (non-diagnostic), and 5 (better	♦ Developed image reconstruction optimization strategy. ♦ Optimized OSEM reconstruction parameters. ♦ Reduction of the acquisition time or dose by up to 50%.

	the Hoffman phantom		Bias Contrast Z-score	image quality than clinical images)	♦ Similar quantification accuracy and image quality obtained with clinical and optimized protocols. ♦ Validation of optimized reconstruction method in retrospective human `PET data with the visual assessment of experienced clinicians. ♦ Optimized protocol produced similar image quality in visual assessment. ♦ PSF correction reduced overall image quality.

*AAL: Automated anatomical labeling; BSREM : Block sequential regularized expectation maximization; BV: Background variability; bvFTD: Behavioural variant frontotemporal dementia; CB: Corticobasal degeneration; CRC: contrast recovery coefficient; COV: Coefficient of variation; DE-PML: Difference image entropy prior - penalized maximum likelihood; DS-PML: Sparse difference images - penalized maximum likelihood; DTV-PML: Difference image total variation prior - penalized maximum likelihood; EOAD: early-onset Alzheimer's disease; FDOPA: fluoro-l-dopa; FMZ: Flumazenil; FWHM: Full-width at half-maximum; GE: General Electric Healthcare; GF: Gaussian filter; GM: Gray matter; i: iterations; LD: low-dose; LBD: Lewy body dementia; MET: Methionine; MADP: mean absolute percentage difference; MLEM: Maximum likelihood expectation-maximization; ND: Normal-dose; NEC density: Noise equivalent count density; OSEM: 3D-ordered subsets expectation maximization; PML: Penalized maximum likelihood; PSF: Point spread function; RC: recovery contrast; RC_{A50}: recovery contrast at the mean value of a 3D-so-contour region at 50% adapted to background; RMSE: root mean-squared error; s: subsets; SD: Standard Deviation; SUV: standard uptake value; SUV_{A50}: standard uptake value at the mean value of a 3D-so-contour region at 50% SUVR: standard uptake value reference; STD: standard; TOF: time-of-flight; TV: total variation; WM: White matte

5 MATERIALS AND METHODS

This study was conducted by acquiring images from the Hoffman 3D brain phantom and using retrospective human data from the Brain Institute (BraIns) at PUCRS, Porto Alegre, Brazil. Data were acquired in a PET/CT scanner (General Electric Medical System, Discovery 600; bismuth germanium oxide detector crystals). The study protocol for the retrospective human data was approved by the Ethics Committee (CAAE: 00919018.6.0000.5336) and all participants signed a written informed consent form in accordance with the Declaration of Helsinki. The following sections describe the materials and methods used in this work.

5.1 SPECIFICATION

The block diagram presented in Figure 4 shows the different stages of this research project. First, PET images of a Hoffman 3D anthropomorphic brain phantom were reconstructed using different algorithms: the analytical methods FBP and FORE, and the iterative method OSEM, as summarized in Table 2. The OSEM iterative reconstruction method is commercially known as Vue-Point HD®, and consists of the implementation of the 3D-ML-OSEM algorithm with all the corrections incorporated during the iterative process (GE HEALTHCARE, 2008). Image reconstruction parameters were optimized based on quantitative accuracy parameters (see Section 3.4) and image quality (see Section 3.5). Our focus was on the optimization strategy to produce images with reduced acquisition time while maintaining adequate quantification accuracy and image quality.

After a set of optimized reconstruction parameters were obtained, retrospective [^{18}F]FDG-PET data of participants with AD and healthy individuals were used to validate the optimized protocol. Finally, the images reconstructed with the optimized parameters were compared to the ones obtained with the clinical protocol (Table 2). All images were reconstructed with an image matrix of 192 × 192 voxels (300 mm FOV), 16-bits per pixel, resolution of 0.640 pixels/mm, pixel size of 1.56 × 1.56 mm, and 47 axial slices of 3.27 mm thickness.

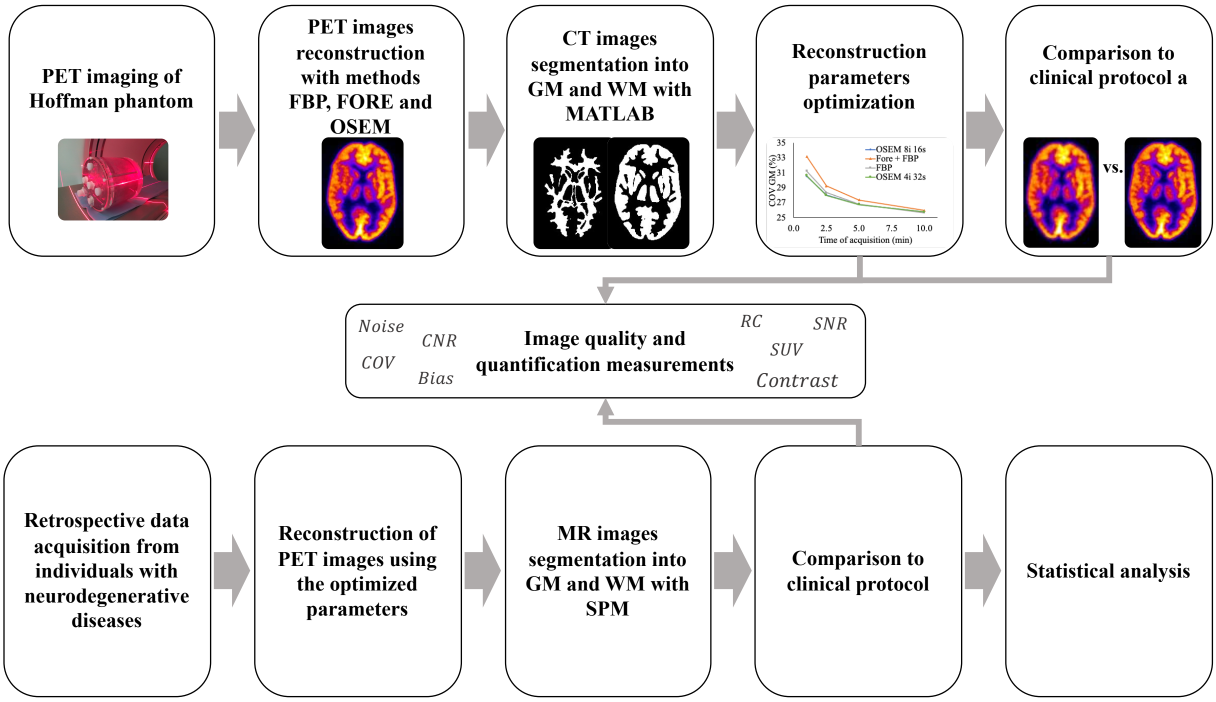

Figure 4: Block diagram showing the workflow of this study. The first stage (top row) will involve acquiring [^{18}F]FDG-PET images of a Hoffman 3D brain phantom, reconstructed using different reconstruction methods. Then, the reconstruction parameters will be optimized by comparing to the clinical protocol. In the second stage (bottom row), retrospective FDG-PET data will be reconstructed using the optimized parameters. Results from the optimized and clinical protocol were compared. Data were extracted from gray matter (GM) and white matter (WM) using masks generated in-house with MATLAB®. Source: (The Author, 2021)

5.2 BRAIN PHANTOM ACQUISITIONS

The Hoffman 3D anthropomorphic brain phantom (Figure 5) consists of 40 acrylic slices (variable thickness, maximum of 3.0 mm) simulates the activity distribution in brain regions. The different acrylic thicknesses produce a gray-to-white matter ratio (contrast) of 4:1. [^{18}F]FDG-PET data were acquired in list-mode for 10 min after the injection of 37 MBq of [^{18}F]FDG. Images were reconstructed with the clinical settings (Table 2), as recommended by the manufacturer and used for clinical brain images at BraIns. Attenuation correction was applied using a CT-based map acquired prior to the PET imaging. Further corrections required for quantification (detector normalization, data rebinning, decay, dead-time, scatter, and random incidences) were applied. Static PET images are presented in a single frame and represent the average radioactive concentration for a given time interval.

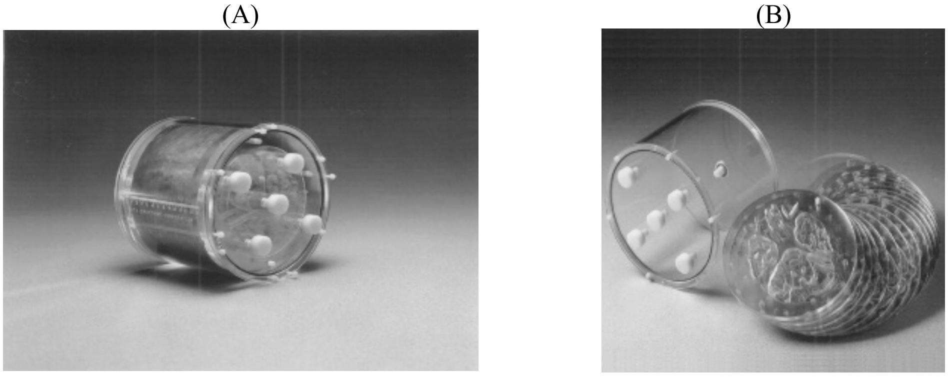

Figure 5: (A) Hoffman 3D brain phantom consists of (B) a cylinder with 40 independent cross-sections. Source:(ELSE SOLUTIONS S.R.L, 2020)

Static PET images were generated with 1 min (90% reduction), 2.5 min (75%), 5 min (50%), and 10 min post acquisition start to assess the impact of reducing the exam duration or injected dose. Additionally, images were reconstructed with 4 iterations and 32 subsets (128 updates), which has the advantage of reducing the noise by halving the number of iterations, henceforth referred to as the optimized reconstruction settings. If more iterations are needed, the noise in the OSEM images will be higher (RIDDELL et al., 2001). Finally, different values of the smoothing filter full-width half-maximum (FWHM) were used (1 to 10 mm) to find out, which resulted in similar images to those reconstructed with the clinical protocol for the range of acquisition times. Image quality and quantitative accuracy were analyzed, aiming to optimize [^{18}F]FDG-PET brain image reconstruction parameters. The optimization strategy focuses on producing images without significant quality loss while maintaining adequate quantitative accuracy in brain regions of low dose or short acquisition time.

5.3 OPTIMIZATION OF THE RECONSTRUCTION PARAMETERS

PET images were reconstructed with different parameters and algorithms available in the workstation to optimize the reconstruction parameters. First, [^{18}F]FDG-PET images from the brain Hoffman simulator were reconstructed as follows: (i) OSEM (8 iterations, 16 subsets, 3.0-mm FWHM post-reconstruction smoothing filter, clinical protocol); (ii) FORE+FBP (enhanced Hanning smoothing filter, 4.8 mm cut-off frequency); and (iii) FBP (enhanced Hanning smoothing filter). We changed only the acquisition time: 10 min, 5 min, 2.5 min, and 1 min. In this phase, the type of algorithm (analytical or iterative) and acquisition time were evaluated by quantification and image quality measurements and by comparing to the clinical protocol.

Table 2: Different [^{18}F]FDG-PET protocols used in this study. Source: (The Author, 2021).

Protocol	**Clinical**	**Research**		**Optimization**	
Reconstruction Algorithm	OSEM	OSEM	FBP	FORE	OSEM
Iterations	8	8	N/A	N/A	4 and 8
Subsets	16	16	N/A	N/A	32 and 16
Iterations-subsets product	128	128	N/A	N/A	128
Acquisition time (min)	10	8	1, 2.5, 5, and 10	1, 2.5, 5, and 10	1, 2.5, 5, and 10
Smoothing filter FWHM (mm)	3	3	4.8	4.8	0-10 (step 1)

In the iterative reconstruction algorithm OSEM is possible to change the number of subsets and iterations. In this study, [^{18}F]FDG-PET images were reconstructed with OSEM with 4 iterations and 32 subsets, as we kept the iterations-subsets product (updates) fixed to 128 (the same as the clinical protocol). Static images were generated for 10 min, 5 min, 2.5 min, and 1 min acquisition times. For these settings, different values of the smoothing filter FWHM (1 to 10 mm) were used. Quantification and image quality measurements were obtained, and results were compared to the clinical OSEM (8 iterations and 16 subsets with Gaussian filter FWHM = 3 mm) reconstruction.

The second step of optimizing the image reconstruction parameters was the evaluation of the PSF correction on image quantification. Images already optimized were compared with the parameters obtained in the previous step (algorithm, time, and smoothing filter FWHM optimization) and images were analyzed with and without the PSF correction. Finally, these sets of reconstruction parameters were used in the validation step with human data.

5.3.1 DATA EXTRACTION

Data was extracted from GM and WM regions using masks segmented from the original CT. A morphological erosion operation was applied to extract the central part of each mask and avoid partial volume effect errors.

5.3.2 QUANTIFICATION ACCURACY AND IMAGE QUALITY

Quantification accuracy was evaluated by RC, gray-to-white matter activity concentration ratio (contrast), and bias. Image quality was assessed by means of the COV, SNR, and CNR. The measurements were obtained by automatically generating volumes-of-interest (VOIs) in the structural image (CT) and transferring them to the static PET images.

5.4 CONTEXT OF THE RETROSPECTIVE STUDIES

Retrospective [^{18}F]FDG-PET data from participants with AD ($n = 18$; average weight, 66.5 ± 13.5 kg; age, 72.1 ± 7.2 years; injected activity, 240 ± 50 MBq; 12/8 female/male participants) and healthy individuals ($n = 17$; average weight, 68.7 ± 11.3 kg; age, 68.7 ± 13.1 years; injected activity, 357 ± 75 MBq; 12/5 female/male participants) were obtained from the BraIns database. All participants underwent neuropsychological tests to estimate their cognitive performance, which were chosen based on relevant studies on cognition in the elderly and early diagnosis of AD, as follows:

- Mini-Mental State Examination (FOLSTEIN; FOLSTEIN; MCHUGH, 1975) validated for the Brazilian population (BRUCKI et al., 2003)
- Rey's Auditory-Verbal Learning Test (IVNIK et al., 1999) with the version validated for Portuguese (MALLOY-DINIZ et al., 2007);
- Boston Naming Test (KAPLAN, EDITH; GOODGLASS, HAROLD; WEINTRAUB, 1983), validated for Portuguese (MIOTTO et al., 2010);
- Verbal Fluency Test for Categories, validated in Brazil (BRUCKI et al., 2003);
- Test of Colored Trails (D'ELLA L.F.; SATZ P.; UCHIYAMA C.L.; WHITE T., 2010).

In the original studies, individuals 50 years or older were included. The inclusion criteria also included literacy and the ability to understand and sign the informed consent form. The exclusion criteria included impossibility to obtain vascular access for percutaneous injection, carriers of malignant neoplasms, autoimmune diseases or hematological diseases, people with other neurological or psychiatric diseases, patients with acute or decompensated heart failure, liver failure, moderate kidney failure, pregnant women, and participation in another clinical trial (BORELLI et al., 2019).

5.5 HUMAN DATA ACQUISITIONS

PET images were reconstructed with the OSEM optimized parameters. MRI data were acquired with a GE Healthcare Signa HDxt 3.0T scanner). High-resolution structural images (T_1-weighted) were acquired with BRAVO^{TM} sequence (BRAin VOlume; repetition time, 2400 ms; echo time, 16 ms; FOV, 220 mm; 1 mm^3 isotropic voxels; matrix size, 512×512×196 pixels; voxel size, 0.47×0.47×1.00 mm^3).

Participants were instructed to follow a low glucose diet 24 hours prior to the [^{18}F]FDG scan as well as fasting for 4-hours prior to imaging. Before injection, the participants were made to rest for 30 min, and capillary glucose was measured 10 min prior to the PET scan, with acceptable levels ranging between 70 and 120 mg/dL, before imaging acquisition (BORELLI et al., 2019). AD patients and healthy volunteers followed slightly diverging protocols on the day of the study. The healthy participants rested in a low-light environment for 30 min, and a 60-min list-mode scan was acquired immediately after a bolus injection of [^{18}F]FDG. The AD patients also rested in a low-light environment, but there was a 50 min interval between bolus injection and image acquisition when a 10-min list-mode scan was performed.

In this study, the PET images were reconstructed with the optimized parameters were compared to those obtained with the research protocol. All semi and quantification metrics, as well as image quality estimates, were obtained for GM, WM, and whole brain. Finally, mean, and maximum SUV values were extracted from 33 volumes-of-interest (VOIs) and compared across reconstruction settings, as well as between the two groups. These VOIs included hypometabolic regions identified in the original study by two experienced physicians (see section 4.5).

5.5.1 RETROSPECTIVE DATA POST-PROCESSING

Anatomical MR images were coregistered to the PET with the SPM12 (http://www.fil.ion.ucl.uk/spm). Coregistration corresponds to the spatial alignment by rigid body transformation (translation and rotation in all axes) between PET and MR images (COLLIGNON et al., 1995), in which the PET image is set as a reference to avoid quantification errors. In addition, anatomical images were segmented into GM, WM, and cerebrospinal fluid (CSF). Lastly, PET and MR images were normalized to the MNI space (152-subjects atlas, Montreal Neurological Institute). Activity concentration measurements from the PET images were extracted from GM, WM (80% threshold), whole brain (WB), and 33 VOIs using the automated anatomical labeling atlas (Wake Forest University Pickatlas, http://fmri.wfubmc.edu/cms/software), as follows: superior, middle, inferior, and medial frontal lobe; anterior cingulate; superior, middle and inferior occipital lobe; superior and inferior parietal lobe; precuneus; superior, superior pole, middle, middle pole, and inferior temporal lobe; and cerebellum. Except for the cerebellum, all VOIs were separated into left and right.

The semiquantification methods used in this study with static [^{18}F]FDG PET were the SUV, and SUVR, considering the pons as the reference region.

Data extraction was performed using the MATLAB® program. Differences between groups (AD and controls) were evaluated using the *Student's t test* in the analyzes of the time interval and in the cross-sectional analyses.

5.5.2 QUANTITATIVE ACCURACY AND IMAGE QUALITY

Quantification accuracy was evaluated by gray-to-white matter activity concentration ratio (contrast) and bias. Image quality was assessed by means of the coefficient of variation (COV) and SNR.

5.5.3 Z-SCORE

Z-score maps were generated based on the following equation:

$$Z = \frac{SUVR_{AD} - \overline{SUVR}}{\sigma} \tag{11}$$

where $SUVR_{AD}$ represents the SUVR map from a given AD patient, and $\overline{SUVR}$ and σ the mean and standard deviation SUVR images from the group of healthy individuals, respectively.

5.5.4 VISUAL ASSESSMENT

The subjective PET image quality was assessed by two nuclear physicians (13 and 5 years of experience in nuclear medicine). The reading order of the images was randomized to reduce subjective bias. The sample size was 35 participants, including healthy controls (*n* = 17) and AD patients (*n* = 18). Each dataset was reconstructed with four different settings, namely optimized and research protocols, with and without the PSF correction. Image quality was scored using 3 features: image noise, contrast, and overall impression of image quality. A Likert-type scale (ARNOLD; MCCROSKEY; PRICHARD, 1967) was used for evaluating PET images using a 5-point scale as follows:

1. The score of 1 was given to the image with nondiagnostic quality, excessive noise, or unfavorable contrast;
2. The score of 2 was given to the image with acceptable quality but with sub-optimal noise and contrast;
3. The score of 3 was given if the image with quality equivalent to the clinical routine in the institution. In other words, the image quality is substantially equivalent to the regular image quality established in the clinical brain [^{18}F]FDG PET routine;

4. The score of 4 was given to the image with quality superior to the average image quality; and
5. The score of 5 was given to the image with excellent quality, optimal noise, and contrast, and free of the artifacts, which provides optimal image quality for the diagnosis with full confidence.

Evaluators were blind to subject name, patient treatment, subject history, or reconstruction parameters. Figure 6 shows how the table is presented to the nuclear physicians for the visual assessment of the PET images. The quality parameters were evaluated in scores (1-5) using four reconstructions carried out for each one of the 35 participants. Paired *t*-test was used to identify differences between metrics.

	C001 / AD001			
	RECON 1	RECON 2	RECON 3	RECON 4
Image noise				
Contrast				
Overall quality				

Figure 6: Visual assessment form for the four reconstructions carried out for each participant from the blind study. Source: (The Author, 2021).

6 RESULTS AND DISCUSSION

6.1 OPTIMIZATION STUDY

6.1.1 PHANTOM SEGMENTATION

Brain VOIs were automatically created from the CT image (Figure 7A) using in-house MATLAB scripts (R2020a, *The MathWorks, Inc.*) by segmenting the GM (270 cm^3; Figure 7B) and WM (160 cm^3; Figure 7C) compartments of the Hoffman 3D brain phantom. The CT acquisition has a total of 47 slices, from which slices 12 to 28 (center of the phantom) were used to create the masks used in the data extraction. The results presented in the optimization study were extracted using the eroded versions of these masks.

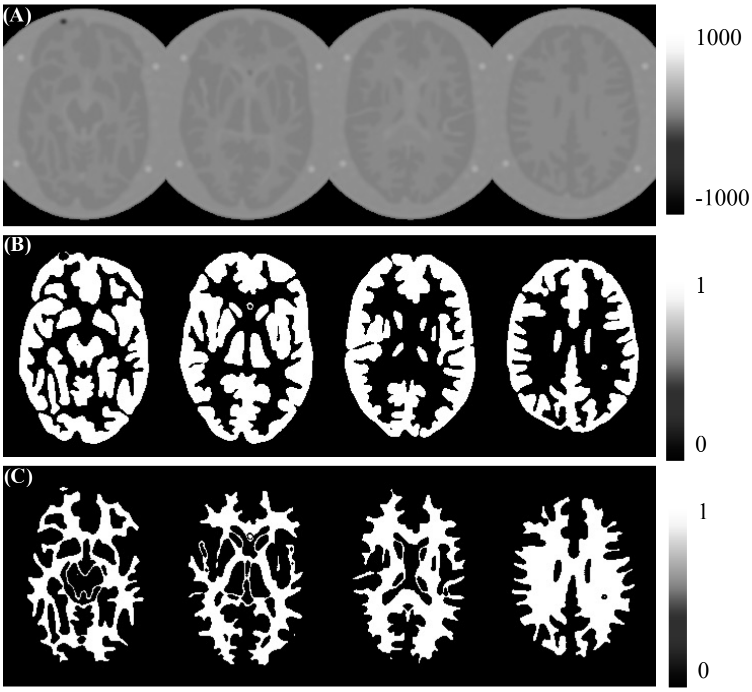

Figure 7: (A) CT image, (B) GM and (C) WM masks (binary images) obtained by segmenting (A) using in-house MATLAB scripts. Source: (The Author, 2021).

6.1.2 COMPARISON BETWEEN RECONSTRUCTION ALGORITHMS

Quantification and image quality metrics were successfully extracted from images reconstructed with all three algorithms for GM and WM. The reconstruction method OSEM presented the highest SNR (Figure 8A), with the lowest quantification bias (Figure 8B) and COV_{GM} (Figure 8C), when compared to FORE+FBP and FBP, for all acquisition times. Furthermore, SNR of images reconstructed with OSEM was constant (approx. 3%) for acquisition times ranging from 2.5 min to 10 min. For all reconstruction methods, SNR and COV_{GM} estimates for the 5-min reconstructions are similar to those obtained from the 10-min images, with less than 5% difference. Quantification bias decreases with the acquisition time, but all three methods presented values lower than 0.7% for 5 min. Finally, the COV is less affected by the reconstruction method than by acquisition time. These results suggest that 5 min would be an adequate choice of acquisition time when compared to the current clinical settings available on the site.

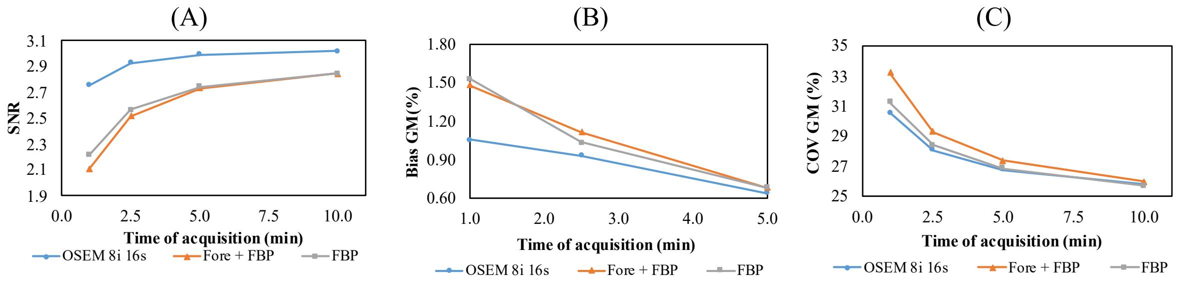

Figure 8: SNR, bias and COV measurements. Results of (A) SNR, (B) GM bias (%) and (C) GM- COV (%) measurements for the reconstruction methods (OSEM, FORE+FBP, and FBP), as a function of the acquisition time. Source: (The Author, 2020).

Table 3 shows the remaining results of contrast, RC_{GM} and RC_{WM}, for the three reconstruction methods (OSEM, FORE+FBP, and FBP). For all reconstruction methods and acquisition times, contrast remains almost stable (approx. 2.4). For comparison, Leemans et al. (2015) obtained values of contrast ranging from 2.7 to 3.5 for images reconstructed using OSEM (1 to 12 iterations, 32 subsets, and 45 min acquisition time), which were directly proportional to the number of iterations. Moreover, Habert et al. (2016) obtained mean contrast of 3.0 ± 0.3 across 22 PET centers (range: 2.3 to 3.8; three time frames of 5 min each) for different equipments and reconstruction methods (HABERT et al., 2016; LEEMANS et al., 2015). The lower contrast obtained by this study was likely due to the shorter image acquisition, as well as differences in equipment and in vendor-specific reconstruction algorithms. Moreover, RC results did not vary with acquisition time or reconstruction method (approx. 0.89 for GM and 0.37 for WM). Lastly, when considering both quantification measurements and image quality metrics, the OSEM reconstruction algorithm presented better overall results, especially for acquisition times ≤ 5 min, in agreement with previous studies (AKAMATSU et al., 2016; AKERELE et al., 2018; CARLIER et al., 2015; IKARI et al., 2016; JIAN; PLANETA; CARSON, 2015; KASTIS et al., 2015; MURRAY et al., 2010; NAGAKI; ONOGUCHI; MATSUTOMO, 2014; PRIETO et al., 2015; SHEKARI et al., 2017; SORET; BACHARACH; BUVAT, 2007; VANHOUTTE et al., 2019; VERHAEGHE; READER, 2010; WALKER et al., 2011). Thus, OSEM was further optimized and later implemented in the human study.

Table 3: Result of contrast, RC_{GM} and RC_{WM}, for the reconstruction methods (OSEM, FORE+FBP, and FBP) and acquisition times of 10 min, 5 min, 2.5 min and 1 min. RC measurement was obtained for GM and WM. Source: (The Author, 2021).

Time (min)	Contrast			RC_{GM}			RC_{WM}		
	OSEM 8i 16s	**FORE+ FBP**	**FBP**	**OSEM 8i 16s**	**FORE+ FBP**	**FBP**	**OSEM 8i 16s**	**FORE+ FBP**	**FBP**
10.0	2.40	2.39	2.36	0.880	0.875	0.874	0.366	0.366	0.370
5.0	2.42	2.41	2.38	0.887	0.882	0.881	0.366	0.365	0.369
2.5	2.42	2.42	2.38	0.890	0.886	0.884	0.368	0.367	0.371
1.0	2.42	2.44	2.42	0.891	0.889	0.889	0.368	0.364	0.367

6.1.3 OSEM OPTIMIZATION

As OSEM was identified as the best method amongst the reconstruction algorithms in the phantom study, it was further optimized in terms of the iterations-subsets product and smoothing filter size. Figure 9 shows the results of CNR for the images reconstructed using OSEM with 4 iterations and 32 subsets, for a range of smoothing filter (Gaussian) FWHMs (0 = no filter to 10 mm) and acquisition times. For comparison, CNR with the clinical settings (OSEM with 8 iterations and 16 subsets with Gaussian filter FWHM = 3 mm) is shown as a single star point. Prieto et al. (2015) used the maximization of CNR to determine the optimal reconstruction parameters. Similarly, CNR, in Figure 9, is maximum when the smoothing filter FHWM ranges from 3 to 6 mm and is comparable to the clinical protocol for all smoothing filter sizes (dashed line) for the 5-min acquisition time. Lastly, when aiming for a 50% scan time reduction, images smoothed with a post-reconstruction filter FWHM of 4 mm yielded the maximum CNR (3.4, approximately 2% less than the current clinical settings).

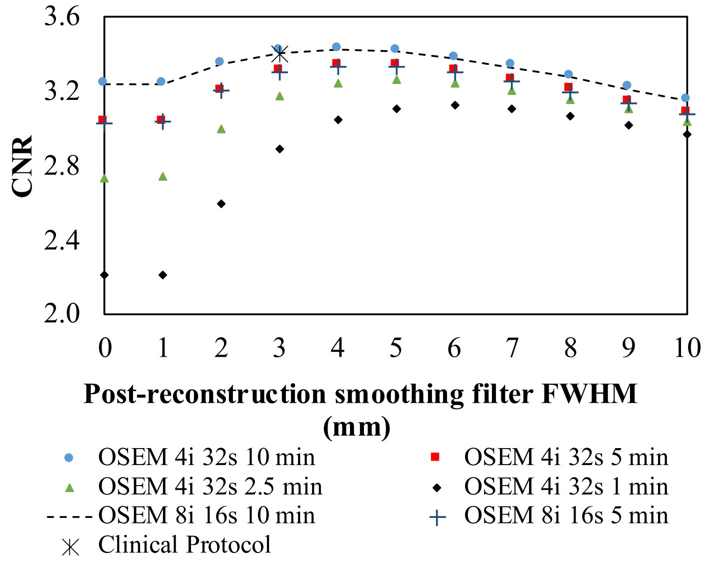

Figure 9: CNR results for the OSEM reconstruction method plotted as a function of the post-reconstruction smoothing filter FWHM. The star point represents the clinical protocol result, while the dashed line represents the

results for the clinical protocol for the range of smoothing filter sizes. For comparison purposes, the + sign represents the clinical protocol when a 50% reduction in time was applied. Source: (The Author, 2021).

Noise decreases as the smoothing filter FWHM increases (PRIETO et al., 2015), and it is comparable to the clinical protocol when the smoothing filter FWHM is greater than 3 mm for an acquisition time of 10-min (Figure 10). In addition, comparable noise levels were observed when the smoothing filter size was greater than 4 mm for acquisition times of 2.5 and 5 min. Gaussian filtering is commonly implemented for noise reduction in low-count [^{18}F]FDG PET (BOELLAARD, 2009; NAGAKI; ONOGUCHI; MATSUTOMO, 2014); however, smoothing reduces spatial resolution and increases apparent blurring.

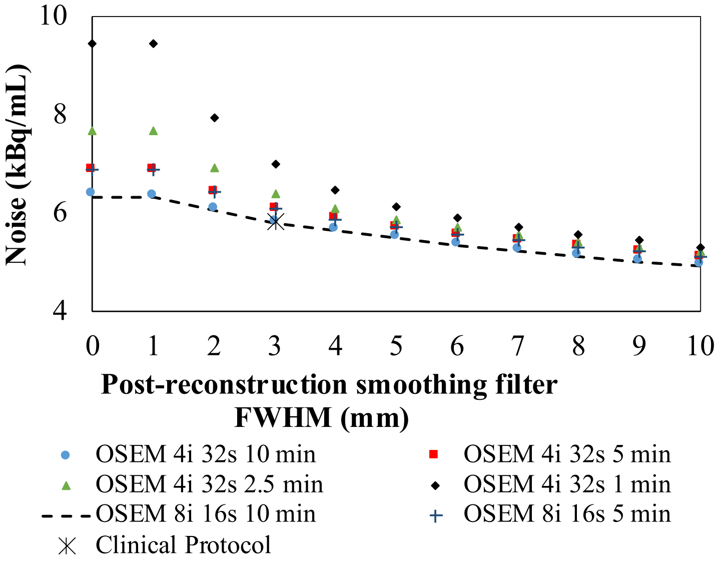

Figure 10: Noise results (kBq/mL) for the OSEM iterative reconstruction method (4 iterations, 32 subsets), plotted as a function of post-reconstruction smoothing filter FWHM. The star point represents the clinical protocol result, while the dashed line represents the results for the clinical protocol for the range of smoothing filter sizes. For comparison purposes, the + sign represents the clinical protocol when a 50% reduction in time was applied. Source: (The Author, 2021).

Table 4 presents the results of contrast, RC, COV, SNR and bias for acquisition times of 5 and 10 min. Although noise and contrast increased with the number of iterations in the study by Prieto et al (2015), these metrics were comparable when 8 (clinical protocol) and 4 iterations were used in this study. This discrepancy is most likely due to the fixed number of updates implemented here. Estimates of contrast, RC, COV_{GM} and SNR for the 5-min reconstruction smoothed with a 4-mm FWHM filter were comparable to those obtained with the clinical protocol (shaded rows). Contrast, RC_{GM} and COV decrease as the smoothing filter size increases, but no improvement in the latter was observed for smoothing filter sizes greater than 5 mm. It is known that RC_{GM} decreases with the smoothing filter FWHM due to the spill-out effect (DU et al., 2013), which causes an overestimation of activity in neighboring regions, such as the WM; therefore, RC_{WM} increases with the smoothing filter FWHM (spill-in effect). Moreover, the SNR was comparable to the clinical protocol when the smoothing filter size is less than 4 mm. Lastly, the smallest quantification bias was observed for 4 and 3 mm for acquisition times of 5 and 10 min, respectively.

Table 4: Result of contrast, RC_{GM}, RC_{WM}, COV_{GW}, COV_{WM} SNR and bias obtained from the images reconstructed with the clinical protocol and with 4 iteration and 32 subsets, for a range of post-reconstruction smoothing filter FWHM (0 to 10 mm), and acquisition times of 5, and 10 min. Source: (The Author, 2021).

Algorithm	*Smoothing filter FWHM (mm)*	*Contrast*	*RC_{GM}*	*RC_{WM}*	*COV_{GM} (%)*	*COV_{WM} (%)*	*SNR*	*Bias (%)*
OSEM 10 min 8i 16s	3	2.40	0.880	0.366	25.8	46.4	3.02	Not applicable
OSEM 10 min 4i 32s	No filter	2.49	0.898	0.360	27.7	49.3	3.03	2.09
	1	2.49	0.898	0.360	27.7	49.3	3.03	2.08
	2	2.46	0.892	0.363	26.5	47.8	3.05	1.33
	3	2.41	0.882	0.366	25.8	46.4	3.04	0.297
	4	2.35	0.871	0.371	25.3	45.2	2.99	–0.985
	5	2.30	0.863	0.376	25.0	44.8	2.89	–1.88
	6	2.20	0.843	0.383	24.8	42.8	2.80	–4.20
	7	2.12	0.827	0.391	24.7	41.8	2.67	–5.97
	8	2.03	0.811	0.399	24.7	40.8	2.53	–7.77
	9	1.95	0.796	0.408	24.7	39.8	2.39	–9.58
	10	1.87	0.780	0.416	24.7	38.9	2.24	–11.4
OSEM 5 min 4i 32s	No filter	2.51	0.904	0.360	29.7	51.6	2.93	2.80
	1	2.51	0.904	0.360	29.7	51.5	2.93	2.80
	2	2.48	0.898	0.362	27.9	49.4	2.99	2.03
	3	2.43	0.888	0.366	26.8	47.6	3.00	0.965
	4	2.37	0.877	0.370	26.2	46.1	2.97	–0.341
	5	2.30	0.863	0.376	25.8	44.8	2.89	–1.88
	6	2.21	0.848	0.383	25.6	43.6	2.79	–3.60
	7	2.13	0.832	0.391	25.4	42.5	2.66	–5.39
	8	2.05	0.816	0.399	25.4	41.4	2.52	–7.21
	9	1.96	0.800	0.408	25.4	40.5	2.38	–9.04
	10	1.88	0.784	0.416	25.4	39.6	2.24	–10.8

Like the quantitative analysis, maintaining the iterations-subsets product constant in the optimization study (4 iterations and 32 subsets; Figure 11B) when compared to the clinical protocol (8 iterations and 16 subsets; Figure 11A) resulted in no noticeable differences in terms of image quality for the same scan time (10 min). In fact, the uniform percentual voxel-wise difference image (Figure 11C) presented an average difference of 0.3 ± 1.0% for GM (0.2 ± 1.0% for WB). When a 50% reduction was applied to the scan time (5 min), a post-reconstruction smoothing filter FWHM of 4 mm produced images with remarkable similarity (Figure 11D) to the clinical protocol—the percentual voxel-wise difference map is shown in (Figure 11E) and average difference was –0.5 ± 6.3% for GM (0.5 ± 6.9% for WB).

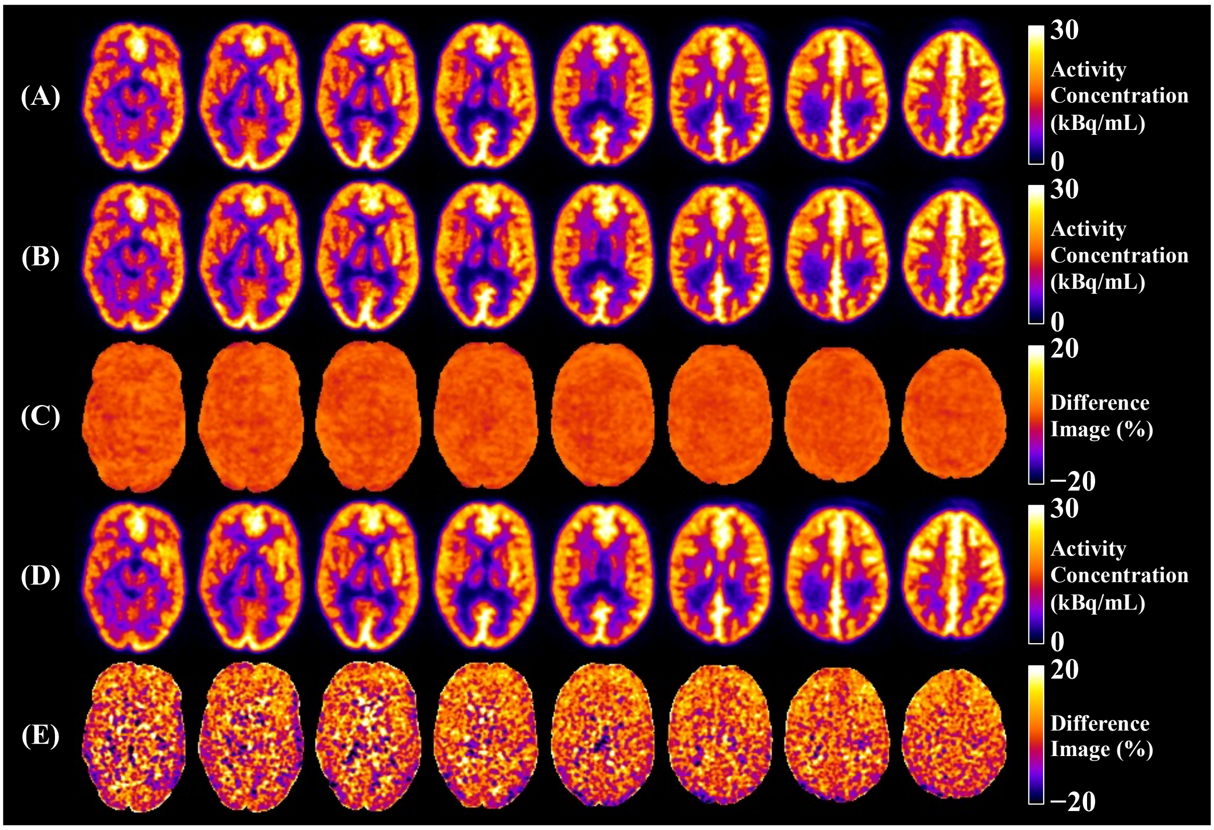

Figure 11: Visual comparison of [^{18}F]FDG-PET images of the Hoffman 3D brain simulator reconstructed with (A) the clinical protocol and (B) the optimized protocol (4 iterations and 32 subsets) for the same acquisition time. (D) Image reconstructed with the optimized protocol for a 50% reduction in scan time (5 min), in which a 4-mm post-reconstruction smoothing filter FWHM was found to produce the optimal results. Respective percentual difference between (A) and (B) and between (A) and (D) are shown in (C) and (E), respectively. Source: (The Author, 2021).

Finally, the optimized protocol parameters are summarized in Table 5.

Table 5: Parameters of the optimized protocol.

Protocol	Optimized Protocol
Reconstruction Algorithm	OSEM
Iterations	4
Subsets	32
Iterations-subsets product	128
Acquisition time (min)	5
Smoothing filter FWHM (mm)	4

6.1.4 COMPARISON BETWEEN CLINICAL AND RESEARCH PROTOCOLS

In our original study (BORELLI et al., 2019), images were reconstructed with the research protocol (Table 6), where the image acquisition time was 8 min. Comparisons of quantification and image quality metrics (Table 7) between the clinical (10 min) and research (8 min) protocols failed to identify substantial differences. Thus, in the human study, the research protocol was used instead of the clinical settings.

Table 6: Parameters of the research protocol. Source: (The Author, 2021).

Protocol	Research Protocol
Reconstruction Algorithm	OSEM
Iterations	8
Subsets	16
Iterations-subsets product	128
Acquisition time (min)	8
Smoothing filter FWHM (mm)	3

Table 7: Results of the research and clinical protocols.Source: (The Author, 2021).

Metrics	Clinical protocol	Research protocol
Contrast	2.40	2.41
RC_{GM}	0.880	0.882
RC_{WM}	0.366	0.366
COV_{GM} **(%)**	25.8	26.1
COV_{WM} **(%)**	46.4	46.9
SNR	3.02	3.01
CNR	3.41	3.38
Noise (kBq/mL)	5.81	5.90
Bias (%)	Not applicable	0.30

6.1.5 PSF CORRECTION

The PSF correction involves incorporating a spatially invariant modification into the OSEM reconstruction (AKERELE et al., 2018), which is expected to increase contrast (i.e., gray-to-white matter ratio). In this study, images reconstructed with the PSF correction presented higher noise than the clinical protocol for the range of smoothing filters (Figure 12A).

When compared to the reconstruction without the PSF correction, the noise was 9.5% higher for a 4-mm smoothing filter FWHM. In addition, there was a decrease in CNR after including the PSF correction in the reconstruction steps (Figure 12B; 3.7% lower for a smoothing filter size of 4 mm), even with the observed increase in contrast (2.37 to 2.59; Table 4; Table 8). Our results agree with Prieto et al. (2015), which reported that images reconstructed with the PSF correction presented significantly higher contrast and were less sensitive to the smoothing filter than their uncorrected counterpart.

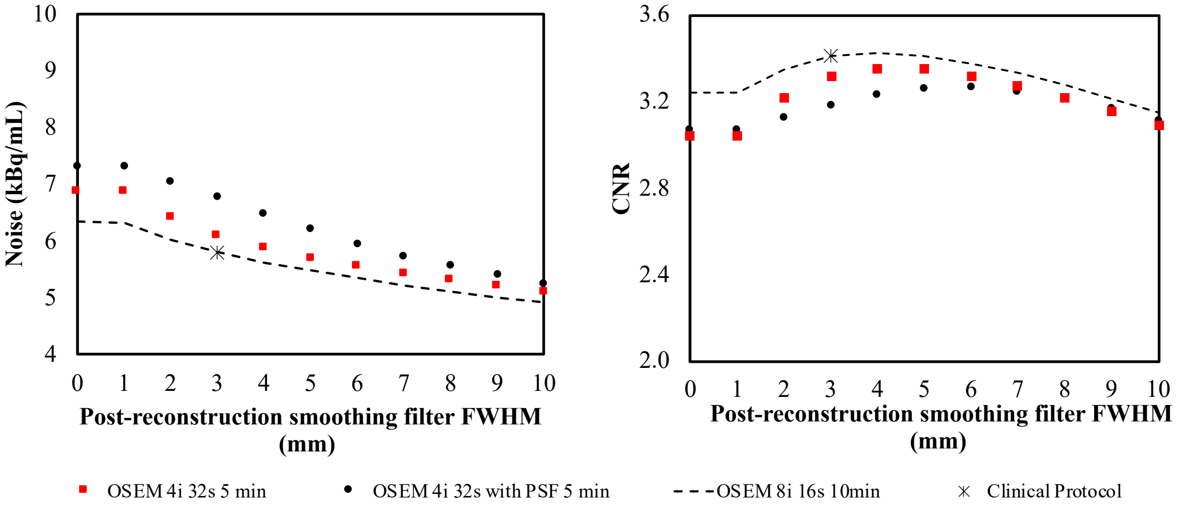

Figure 12: Results of noise and CNR extracted from images reconstructed with the optimized reconstruction method and incorporated the PSF correction ,for a range of post-reconstruction smoothing filter FWHM (0 to 10 mm), and acquisition times of 5- and 10-min. Source: (The Author, 2021).

Table 8 presents the remaining quantification and image quality metrics. No major differences with the clinical protocol were identified.

Table 8: Results of contrast, RC, COV, SNR and bias obtained from images reconstructed with the optimized reconstruction method and incorporated the PSF correction, for a range of post-reconstruction smoothing filter FWHM (0 to 10 mm), and acquisition times of 5 and 10 min. Source: (The Author, 2021).

Algorithm	*Smoothing filter FWHM (mm)*	*Contrast*	*RC_{GM}*	*RC_{WM}*	*COV_{GM} (%)*	*COV_{WM} (%)*	*SNR*	*Bias (%)*
OSEM 10 min 8i 16s	3	2.63	0.908	0.346	28.09	49.28	3.30	3.23
OSEM 5 min 4i 32s	4	2.59	0.905	0.350	28.00	48.90	3.25	2.82

Figure 13 shows a comparison between the clinical (Figure 13A) and the optimized (Figure 13B) protocols when the PSF correction was implemented (difference image is presented in Figure 13C). Previous studies observed that the PSF correction is most effective for enhancing the image quality in the brain by improving the spatial resolution, contrast and COV (NAGAKI; ONOGUCHI; MATSUTOMO, 2014; TONG; ALESSIO; KINAHAN, 2010a). In fact, the inclusion of the PSF correction have been found to visually improve COV and enhance the GM edges (NAGAKI; ONOGUCHI; MATSUTOMO, 2014). The same findings were observed in our study (Figure 13A-B). Conversely, Snyder et al. (1987) observed the production of ring artifacts (SNYDER et al., 1987).

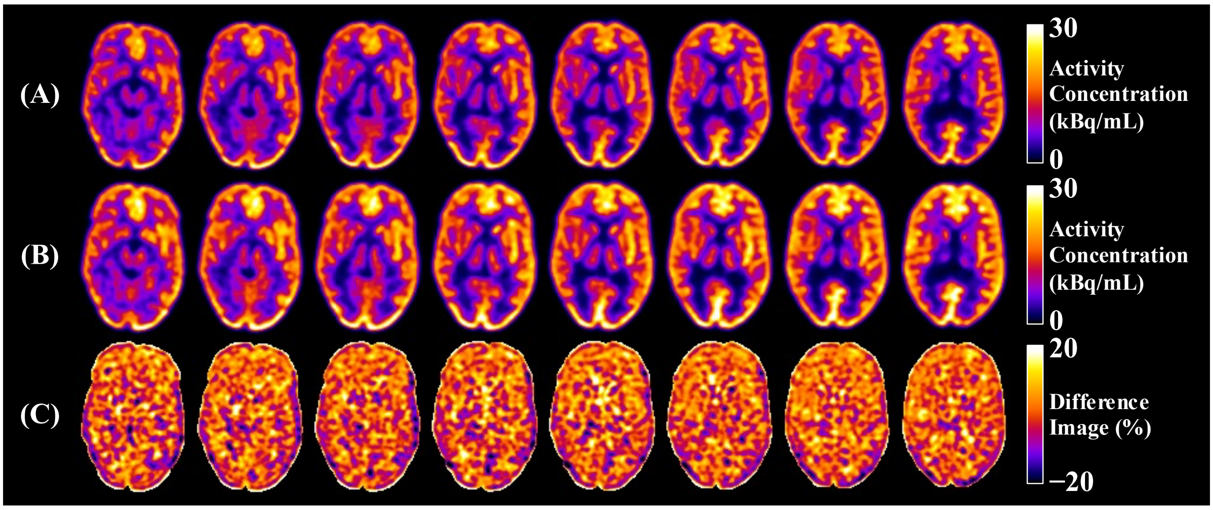

Figure 13: Visual comparison of [^{18}F]FDG-PET images of the Hoffman 3D brain simulator reconstructed with the (A) clinical (10 min) and (B) optimized (5 min) protocols for the same acquisition time. Both images were reconstructed with the PSF correction. Percentual difference between (A) and (B) is shown in (C). Source: (The Author, 2021).

6.2 HUMAN STUDY

Following the optimization study with phantom data, the optimized reconstruction protocol was implemented in human data composed of healthy individuals and AD patients. The next sections describe the main findings of the human study.

6.2.1 QUANTIFICATION OF HUMAN DATA

Quantification and image quality measurements were successfully extracted from all healthy individuals ($n = 17$) and AD patients ($n = 18$), and average values are shown in Table 9. In addition, Table 10 summarizes results obtained with the inclusion of the PSF correction. Except for bias, all measurements extracted from images reconstructed with the optimized protocol were significantly lower than the respective measurements from the research protocol

($p < 0.01$), although the differences were small (i.e., 1 to 2% for contrast, SUVR and COV_{GM}, for both groups; and SNR difference of 2 and 4% for healthy individuals and AD patients, respectively). These results are in agreement with previous studies (NAGAKI; ONOGUCHI; MATSUTOMO, 2014; REYNÉS-LLOMPART et al., 2018).

Table 9: Results of contrast, SUVR, COV, SNR and bias extracted from images reconstructed with the optimized and research protocols for the two groups (healthy individuals, $n = 17$; and AD patients, $n = 18$). Source: (The Author, 2021).

Metrics	**Healthy Individuals**		**AD Patients**	
	Optimized protocol	Research protocol	Optimized protocol	Research protocol
Contrast	1.67 ± 0.18 [a]	1.70 ± 0.18	1.52 ± 0.14 [a]	1.55 ± 0.15
SUVR	1.60 ± 0.12 [a]	1.62 ± 0.12	1.60 ± 0.34 [a]	1.62 ± 0.35
COV_{GM} (%)	20.6 ± 3.6 [a]	20.8 ± 3.7	22.4 ± 3.1 [a]	22.7 ± 3.2
SNR	2.64 ± 0.72 [a]	2.70 ± 0.74	1.86 ± 0.56 [a]	1.93 ± 0.58
Bias (%)	−1.62 ± 0.74	-	−1.42 ± 0.45	-

[a] Significantly different than the respective measurement from research image reconstruction ($p < 0.01$).

Table 10: Results of contrast, SUVR, COV, SNR and bias extracted from images reconstructed with the optimized and research protocols with PSF correction for the two groups (healthy individuals, $n = 17$; and AD patients, $n = 18$). Source: (The Author, 2021).

Metrics	**Healthy Individuals**		**AD Patients**	
	Optimized protocol	Research protocol	Optimized protocol	Research protocol
Contrast	1.78 ± 0.19 [a]	1.82 ± 0.20	1.62 ± 0.17 [a]	1.66 ± 0.18
SUVR	1.62 ± 0.12 [a]	1.64 ± 0.13	1.62 ± 0.35 [a]	1.64 ± 0.36
COV_{GM} (%)	21.9 ± 3.5 [a]	22.5 ± 3.6	24.0 ± 3.2 [a]	24.5 ± 3.2
SNR	2.83^{o} ± 0.73 [a]	2.90 ± 0.75	2.05^{o} ± 0.61 [a]	2.10 ± 0.63
Bias (%)	−1.82 ± 0.31	-	−1.41 ± 0.44	-

[a] Significantly different than the respective measurement from research image reconstruction ($p < 0.01$).

6.2.2 SUVR

Given the strong dependency of SUV to image resolution and noise (BOELLAARD et al., 2004), its normalization to a reference region (i.e., SUVR) reduces the influences due to differences in scanner performance and reconstruction protocol (HUTTON et al., 2015). In this study, images were converted to SUVR (Eq. (5)) by dividing the activity concentration in each voxel to that of the reference, i.e., the pons (NUGENT et al., 2020). No significant differences in SUV were observed for the pons between healthy individuals (SUV of 4.6 ± 0.6 g/mL and 4.6 ± 0.6 g/mL for the research and optimized protocols, respectively) and AD patients (SUV of 5.0 ± 0.9 g/mL and 5.0 ± 0.9 g/mL for the research ($p = 0.14$) and optimized ($p = 0.12$) protocols, respectively).

Table 11 presents average SUVR values for the 33 regions for both groups. The values are similar to those reported by Soret et al. (2020). Significance was observed for all regions ($p < 0.05$) when comparing the two groups, except for the occipital lobe (both left and right hemispheres) and left superior temporal lobe.

Table 11: SUVR measurements extracted from images reconstructed with research (top rows) and optimized (bottom rows) protocols for healthy individuals ($n = 17$) and AD patients ($n = 18$). Only the cerebellum was not separated into left and right hemispheres. Source: (The Author, 2021).

SUVR				
VOIs	**Healthy Individuals**		**AD Patients**	
	Left	**Right**	**Left**	**Right**
Research protocol				
Superior Frontal Lobe	1.42 ± 0.14	1.41 ± 0.13	1.26 ± 0.12[a]	1.30 ± 0.12[a]
Middle Frontal Lobe	1.54 ± 0.14	1.49 ± 0.14	1.35 ± 0.17[a]	1.34 ± 0.17[a]
Inferior Frontal Lobe	1.48 ± 0.16	1.37 ± 0.14	1.32 ± 0.18[a]	1.24 ± 0.15[a]
Medial Frontal Lobe	1.40 ± 0.16	1.44 ± 0.14	1.23 ± 0.10[a]	1.31 ± 0.11[a]
Anterior Cingulate	1.45 ± 0.15	1.39 ± 0.13	1.28 ± 0.13[a]	1.29 ± 0.13[a]
Superior Occipital Lobe	1.39 ± 0.15	1.43 ± 0.14	1.32 ± 0.23	1.36 ± 0.22
Mid Occipital Lobe	1.56 ± 0.15	1.46 ± 0.13	1.43 ± 0.30	1.35 ± 0.24
Inferior Occipital Lobe	1.61 ± 0.17	1.43 ± 0.15	1.48 ± 0.33	1.32 ± 0.26
Superior Parietal Lobe	1.29 ± 0.15	1.12 ± 0.15	1.12 ± 0.26[a]	0.97 ± 0.21[a]
Inferior Parietal Lobe	1.56 ± 0.13	1.42 ± 0.14	1.31 ± 0.27[a]	1.23 ± 0.29[a]
Precuneus	1.57 ± 0.12	1.61 ± 0.11	1.37 ± 0.25[a]	1.43 ± 0.26[a]
Superior Temporal Lobe	1.56 ± 0.11	1.45 ± 0.13	1.39 ± 0.23[a]	1.33 ± 0.22
Superior Temporal Pole	1.07 ± 0.12	0.99 ± 0.11	0.87 ± 0.12[a]	0.87 ± 0.12[a]
Middle Temporal Lobe	1.50 ± 0.12	1.45 ± 0.12	1.30 ± 0.24[a]	1.28 ± 0.23[a]
Middle Temporal Pole	1.06 ± 0.19	1.02 ± 0.14	0.89 ± 0.16[a]	0.87 ± 0.12[a]
Inferior Temporal	1.39 ± 0.16	1.35 ± 0.13	1.20 ± 0.23[a]	1.16 ± 0.18[a]
Cerebellum	1.26 ± 0.07		1.24 ± 0.08	
Optimized protocol				
Superior Frontal Lobe	1.42 ± 0.13	1.41 ± 0.13	1.25 ± 0.12[a]	1.29 ± 0.13[a]
Middle Frontal Lobe	1.54 ± 0.14	1.48 ± 0.14	1.34 ± 0.16[a]	1.34 ± 0.17[a]
Inferior Frontal Lobe	1.48 ± 0.16	1.36 ± 0.13	1.32 ± 0.17[a]	1.24 ± 0.15[a]
Medial Frontal Lobe	1.40 ± 0.16	1.44 ± 0.14	1.23 ± 0.10[a]	1.31 ± 0.11[a]
Anterior Cingulate	1.44 ± 0.15	1.38 ± 0.13	1.27 ± 0.13[a]	1.29 ± 0.13[a]
Superior Occipital Lobe	1.39 ± 0.15	1.42 ± 0.15	1.31 ± 0.23	1.36 ± 0.22
Mid Occipital Lobe	1.55 ± 0.15	1.46 ± 0.13	1.41 ± 0.29	1.35 ± 0.23
Inferior Occipital Lobe	1.61 ± 0.17	1.43 ± 0.15	1.46 ± 0.32	1.32 ± 0.25
Superior Parietal Lobe	1.29 ± 0.15	1.13 ± 0.16	1.11 ± 0.25[a]	0.97 ± 0.21[a]
Inferior Parietal Lobe	1.56 ± 0.13	1.42 ± 0.14	1.31 ± 0.26[a]	1.23 ± 0.29[a]
Precuneus	1.57 ± 0.12	1.60 ± 0.11	1.36 ± 0.24[a]	1.43 ± 0.25[a]
Superior Temporal Lobe	1.56 ± 0.11	1.45 ± 0.13	1.38 ± 0.22[a]	1.33 ± 0.21
Superior Temporal Pole	1.06 ± 0.12	0.99 ± 0.11	0.86 ± 0.12[a]	0.87 ± 0.11[a]
Middle Temporal Lobe	1.50 ± 0.12	1.45 ± 0.12	1.29 ± 0.23[a]	1.28 ± 0.22[a]
Middle Temporal Pole	1.06 ± 0.19	1.01 ± 0.13	0.88 ± 0.15[a]	0.87 ± 0.12[a]
Inferior Temporal	1.39 ± 0.16	1.34 ± 0.13	1.20 ± 0.23[a]	1.16 ± 0.17[a]
Cerebellum	1.26 ± 0.07		1.23 ± 0.08	

[a] Statistically different than respective measurements from healthy individuals ($p < 0.05$).

Significant differences between the research and optimized protocols were observed, as identified by the Bland-Altman plot, for controls (–0.002 ± 0.011, $p < 0.01$; Figure 14A) and AD patients (–0.007 ± 0.013, $p < 0.01$; Figure 14B).

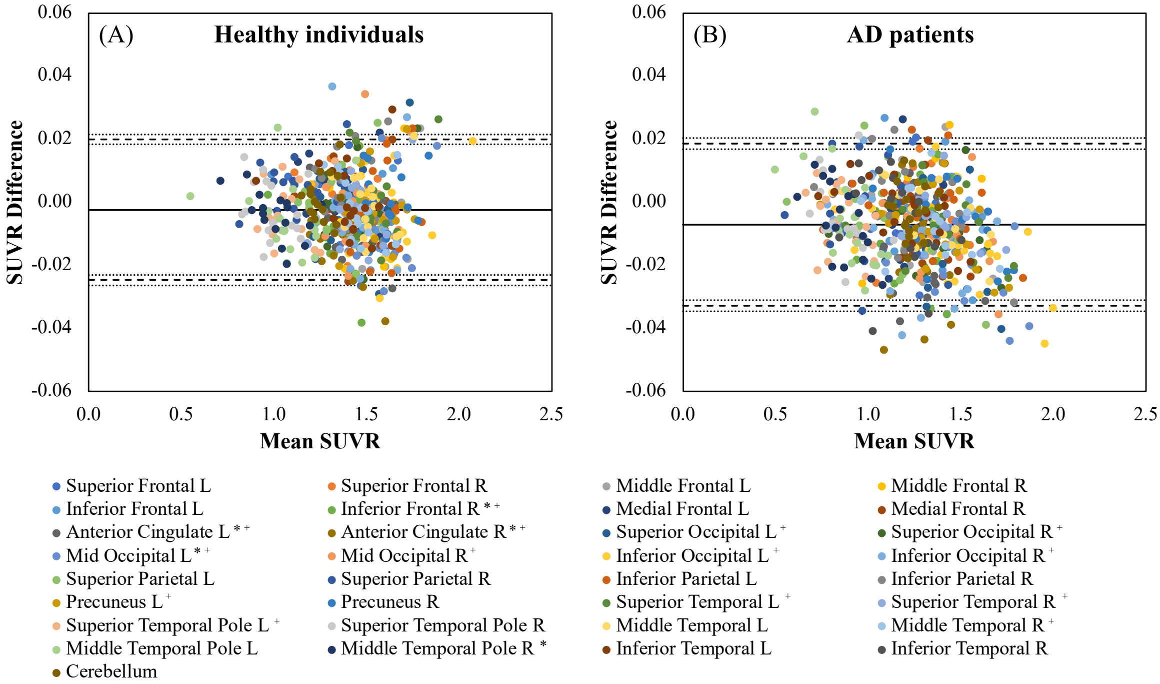

Figure 14: Bland-Altman plots between research and optimized protocols for (A) healthy individuals ($n = 17$) and (B) AD patients ($n = 18$). The mean is represented by the solid line, while the dashed lines represent the limits of agreement (±2 standard deviations), each with its own 95% confidence intervals (dotted lines). Mean SUVR difference across VOIs was -0.002 ± 0.011 for healthy individuals (significance was indicated by the * symbol, $p < 0.05$) and -0.007 ± 0.013 for AD patients (significance was indicated by the + symbol, $p < 0.05$). Source: (The Author, 2021).

Table 12 present average SUVR values when the PSF correction was included. Significant differences between the research and optimized protocols with the PSF correction were observed, as identified by the Bland-Altman plot, for controls (-0.003 ± 0.011, $p < 0.01$; Figure 15A) and AD patients (-0.007 ± 0.014, $p < 0.01$; Figure 15B).

Table 12: SUVR measurements extracted from images reconstructed with the research (top rows) and optimized (bottom rows) protocols for healthy individuals ($n = 17$) and AD patients ($n = 18$) when the PSF correction was included in the reconstruction algorithm. Only the cerebellum was not separated into left and right hemispheres. Source: (The Author, 2021).

SUVR				
VOIs	**Healthy Individuals**		**AD Patients**	
	Left	**Right**	**Left**	**Right**
Research protocol				
Superior Frontal Lobe	1.43 ± 0.14	1.42 ± 0.14	1.26 ± 0.12[a]	1.30 ± 0.12[a]
Middle Frontal Lobe	1.56 ± 0.15	1.50 ± 0.15	1.36 ± 0.17[a]	1.34 ± 0.17[a]
Inferior Frontal Lobe	1.48 ± 0.17	1.37 ± 0.14	1.32 ± 0.18[a]	1.24 ± 0.15[a]
Medial Frontal Lobe	1.39 ± 0.16	1.43 ± 0.15	1.23 ± 0.1[a]	1.31 ± 0.11[a]
Anterior Cingulate	1.43 ± 0.16	1.37 ± 0.14	1.27 ± 0.13[a]	1.29 ± 0.13[a]
Superior Occipital Lobe	1.40 ± 0.16	1.44 ± 0.15	1.34 ± 0.24	1.36 ± 0.22
Mid Occipital Lobe	1.59 ± 0.15	1.50 ± 0.13	1.46 ± 0.31	1.35 ± 0.25
Inferior Occipital Lobe	1.64 ± 0.17	1.47 ± 0.16	1.50 ± 0.34	1.32 ± 0.27
Superior Parietal Lobe	1.30 ± 0.16	1.13 ± 0.17	1.13 ± 0.26[a]	0.97 ± 0.22[a]
Inferior Parietal Lobe	1.58 ± 0.14	1.42 ± 0.14	1.32 ± 0.27[a]	1.23 ± 0.30[a]
Precuneus	1.56 ± 0.12	1.59 ± 0.11	1.35 ± 0.25[a]	1.43 ± 0.25[a]
Superior Temporal Lobe	1.55 ± 0.11	1.44 ± 0.13	1.39 ± 0.22[a]	1.33 ± 0.21
Superior Temporal Pole	1.05 ± 0.12	0.98 ± 0.12	0.85 ± 0.12[a]	0.87 ± 0.12[a]
Middle Temporal Lobe	1.51 ± 0.12	1.46 ± 0.13	1.30 ± 0.24[a]	1.28 ± 0.23[a]
Middle Temporal Pole	1.08 ± 0.20	1.02 ± 0.14	0.90 ± 0.17[a]	0.87 ± 0.13[a]
Inferior Temporal	1.41 ± 0.17	1.36 ± 0.14	1.21 ± 0.24[a]	1.16 ± 0.18[a]
Cerebellum	1.25 ± 0.07		1.23 ± 0.08	
Optimized protocol				
Superior Frontal Lobe	1.43 ± 0.14	1.42 ± 0.13	1.26 ± 0.12[a]	1.30 ± 0.12[a]
Middle Frontal Lobe	1.55 ± 0.15	1.50 ± 0.15	1.35 ± 0.17[a]	1.34 ± 0.17[a]
Inferior Frontal Lobe	1.48 ± 0.16	1.36 ± 0.14	1.31 ± 0.18[a]	1.24 ± 0.15[a]
Medial Frontal Lobe	1.39 ± 0.16	1.43 ± 0.14	1.22 ± 0.10[a]	1.31 ± 0.11[a]
Anterior Cingulate	1.43 ± 0.15	1.36 ± 0.13	1.26 ± 0.13[a]	1.29 ± 0.13[a]
Superior Occipital Lobe	1.40 ± 0.16	1.44 ± 0.15	1.33 ± 0.23	1.36 ± 0.22
Mid Occipital Lobe	1.58 ± 0.15	1.49 ± 0.14	1.44 ± 0.31	1.35 ± 0.24
Inferior Occipital Lobe	1.63 ± 0.17	1.46 ± 0.16	1.49 ± 0.33	1.32 ± 0.27
Superior Parietal Lobe	1.30 ± 0.16	1.14 ± 0.17	1.12 ± 0.26[a]	0.97 ± 0.21[a]
Inferior Parietal Lobe	1.57 ± 0.14	1.42 ± 0.14	1.32 ± 0.27[a]	1.23 ± 0.30[a]
Precuneus	1.56 ± 0.12	1.58 ± 0.11	1.34 ± 0.24[a]	1.43 ± 0.25[a]
Superior Temporal Lobe	1.55 ± 0.12	1.44 ± 0.13	1.38 ± 0.22[a]	1.33 ± 0.21
Superior Temporal Pole	1.05 ± 0.12	0.98 ± 0.11	0.84 ± 0.12[a]	0.87 ± 0.11[a]
Middle Temporal Lobe	1.51 ± 0.12	1.45 ± 0.12	1.29 ± 0.23[a]	1.28 ± 0.22[a]
Middle Temporal Pole	1.08 ± 0.20	1.02 ± 0.14	0.90 ± 0.15[a]	0.87 ± 0.12[a]
Inferior Temporal	1.40 ± 0.17	1.36 ± 0.14	1.21 ± 0.23[a]	1.16 ± 0.17[a]
Cerebellum	1.25 ± 0.07		1.22 ± 0.08	

[a] Statistically different than respective measurements from healthy individuals ($p < 0.05$).

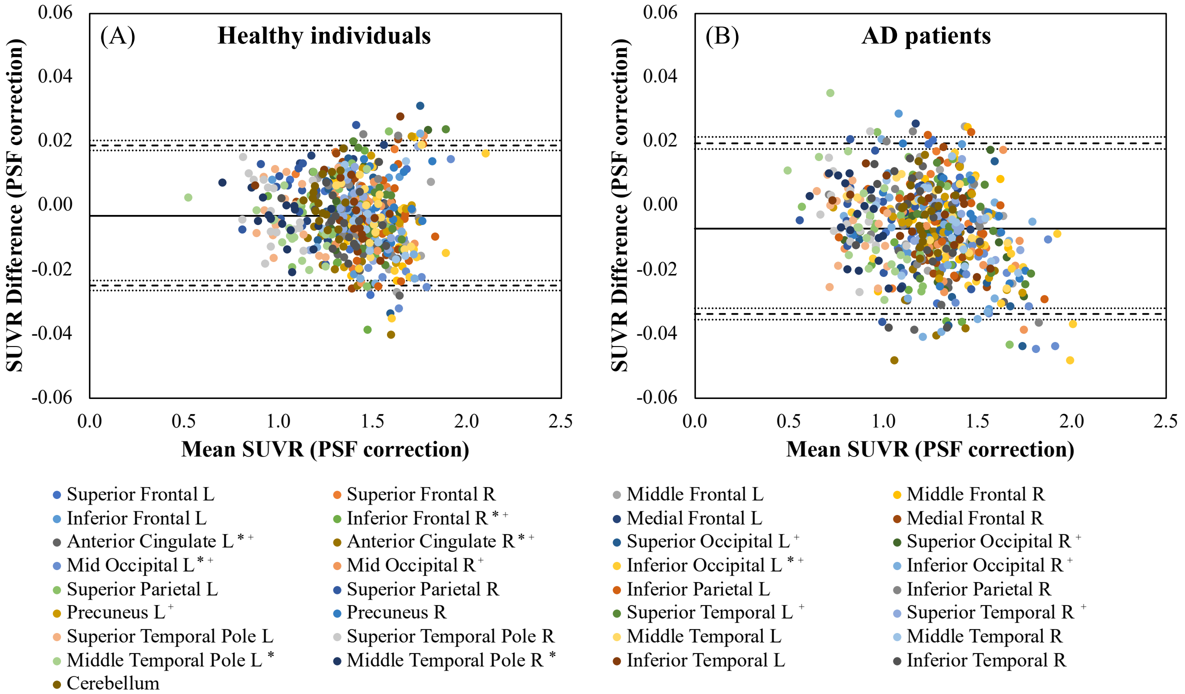

Figure 15: Bland-Altman plots between research and optimized protocols for (A) healthy individuals (*n* = 17) and (B) AD patients (*n* = 18), age paired group, when the PSF correction was included in the reconstruction algorithm. The mean is represented by the solid line, while the dashed lines represent the limits of agreement (±2 standard deviations), each with its own 95% confidence intervals (dotted lines). Mean SUVR difference across VOIs was –0.003 ± 0.011 for healthy individuals (significance was indicated by the * symbol, $p < 0.05$) and –0.007 ± 0.014 for AD patients (significance was indicated by the + symbol, $p < 0.05$). Source: (The Author, 2021).

6.2.3 Z-SCORE

Figure 16A shows Z-score values obtained with the optimized protocol when compared to the research protocol (threshold < –1.96). Diagnostic accuracy can be improved by constructing Z-score maps, which show patterns of significant deficits and have been an increasingly important part of the clinical evaluation (FÄLLMAR et al., 2016). These maps are obtained by spatially normalizing the image from a given individual and comparing it to an average image from a healthy control database (FÄLLMAR et al., 2016). The resulting parametric map can highlight cortical areas with statistically significant deficits, which optimizes the pattern recognition to the reader and facilitates differential diagnosis. FDG-based Z-maps have been shown to improve diagnostic accuracy in neurodegenerative diseases (DRZEZGA, 2009). Therefore, it is fundamental that the optimization of reconstruction methods results in minimal impact in these measurements.

In our study, the average regression line between Z-scores obtained with the optimized protocol and those of the research protocol was $y = 1.07x + 0.001$, and a significant ($p < 0.01$) and strong correlation (average Pearson correlation coefficient of 0.99 ± 0.02) was observed. Fallmar et al. (2016) presented a similar graph when a low dose was used; however, the Z-scores presented a higher variability than ours (Figure 16). This discrepancy could be explained by the approx. 40% dose reduction in our study (in the form of acquisition time reduction) when compared to a 75% dose reduction proposed by Fallmar et al. (2016). The respective Bland-Altman plot is shown in Figure 16B. A small but significant bias in Z-score values was observed in our study (–0.02, $p < 0.01$), similar to the results reported by Fallmar et al. (2016), in which a significant bias was observed when a dose reduction was implemented.

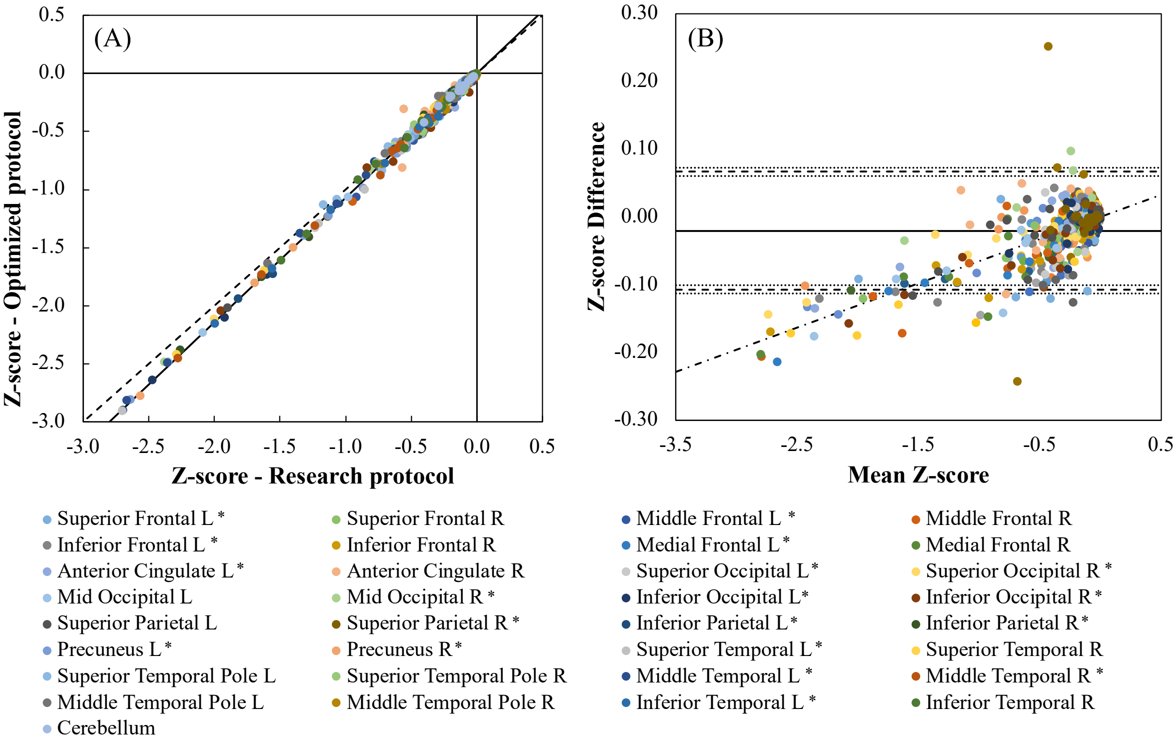

Figure 16: Z-score values obtained with the images reconstructed with the optimized protocol when compared to respective measurements from the research protocol (A; healthy individuals, $n = 17$; and AD patients, $n = 18$). Average regression line presented mean slope of 1.07 ± 0.04 (mean intercept of 0.001 ± 0.007, $R^2 = 0.98 \pm 0.04$; Pearson correlation coefficient, 0.99 ± 0.02). (B) Respective Bland-Altman plots between research and optimized protocols. The mean is represented by the solid line, while the dashed lines represent the limits of agreement (±2 standard deviations), each with its own 95% confidence intervals (dotted lines). Mean Z-score difference across VOIs was –0.020 ± 0.044 (significance was indicated by the * symbol, $p < 0.05$). A significant correlation between differences and mean was observed (dot-dashed line, $y = 0.065x$, $R^2 = 0.53$; Pearson correlation coefficient of 0.73, $p < 0.01$). Source: (The Author, 2021).

When the PSF correction was incorporated into the reconstruction algorithm, similar Z-scores were obtained when comparing the optimized and the research protocol (Figure 17B). Average regression line from the 33 VOIs presented mean slope of 1.09 ± 0.05 (respective mean intercept of –0.003 ± 0.006; $R^2 = 0.99 \pm 0.02$; Pearson correlation coefficient, 0.99 ± 0.02, $p < 0.01$). The respective Bland-Altman plot is presented in Figure 17B.

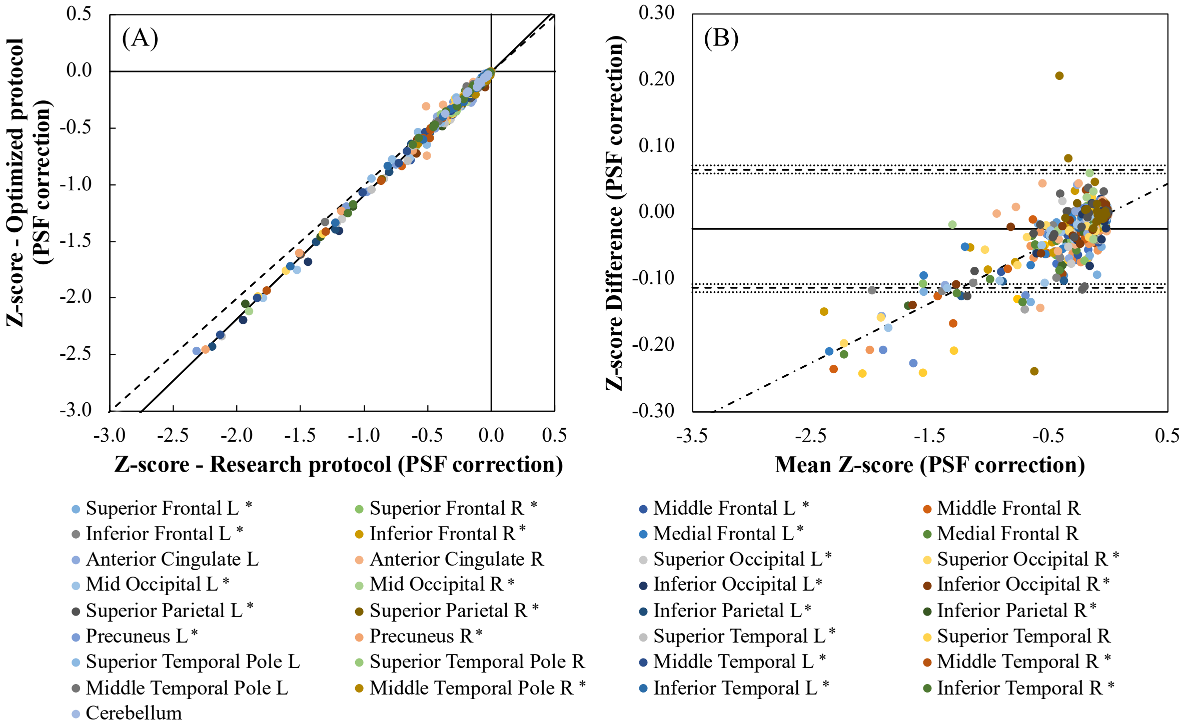

Figure 17: Z-score values obtained with the images reconstructed with the optimized protocol when compared to respective measurements from the research protocol (A; healthy individuals, $n = 17$; and AD patients, $n = 18$), age paired group, when the PSF correction was included in the reconstruction. Average regression line presented mean slope of 1.09 ± 0.05 (mean intercept of –0.002 ± 0.006, $R^2 = 0.99 \pm 0.02$; Pearson correlation coefficient, 0.99 ± 0.02). (B) Respective Bland-Altman plots between research and optimized protocols. The mean is represented by the solid line, while the dashed lines represent the limits of agreement (±2 standard deviations), each with its own 95% confidence intervals (dotted lines). Mean Z-score difference across VOIs was –0.023 ± 0.045 (significance was indicated by the * symbol, $p < 0.05$). A significant correlation between differences and mean was observed (dot-dashed line, $y = 0.09x - 0.001$, $R^2 = 0.63$; Pearson correlation coefficient of 0.80, $p < 0.01$). Source: (The Author, 2021).

6.2.4 VISUAL ASSESSMENT

The last step of our study was to visually assess the reconstructed images, which two experienced physicians carried out in a blind analysis. For each image, the evaluators assigned scores ranging from 1 to 5 (where 3 represented a score of an image with diagnostic quality) to the images in terms of noise, contrast, and general image quality. Summary of results can be found in Table 13.

Table 13: Results of visual assessment for images reconstructed with the optimized and research protocols. Scores (1-5) are presented as mean ± SD (healthy individuals, $n = 17$; AD patients, $n = 18$). Source: (The Author, 2021).

Evaluators	**Metrics**	**Healthy Individuals**		**AD Patients**	
		Optimized protocol	Research protocol	Optimized protocol	Research protocol
Physician 1	Noise	3.6 ± 0.5	3.6 ± 0.6	3.2 ± 0.4	3.1 ± 0.6
	Contrast	3.6 ± 0.5	3.6 ± 0.6	3.1 ± 0.6	3.1 ± 0.6
	Overall	3.6 ± 0.5	3.6 ± 0.6	3.2 ± 0.4	3.1 ± 0.6
Physician 2	Noise	2.2 ± 0.7	2.2 ± 0.5	2.3 ± 0.6	2.2 ± 0.5
	Contrast	2.8 ± 0.6	2.8 ± 0.4	3.1 ± 0.6	2.9 ± 0.5
	Overall	2.7 ± 0.6	2.7 ± 0.5	2.9 ± 0.7	2.7 ± 0.5

Overall, no differences in noise, contrast, and overall image quality were observed when comparing optimized and research protocols; however, the second physician tended to assign lower scores to all three metrics.

Figure 18 presents the images reconstructed with the research (columns in the left) and optimized (columns in the right) protocols from two representative subjects from each group. The remarkable similarity between the images presented in Figure 18 suggests that implementing the optimized protocol when necessary is feasible, representing a 40% imaging time reduction compared to the research protocol (8 min).

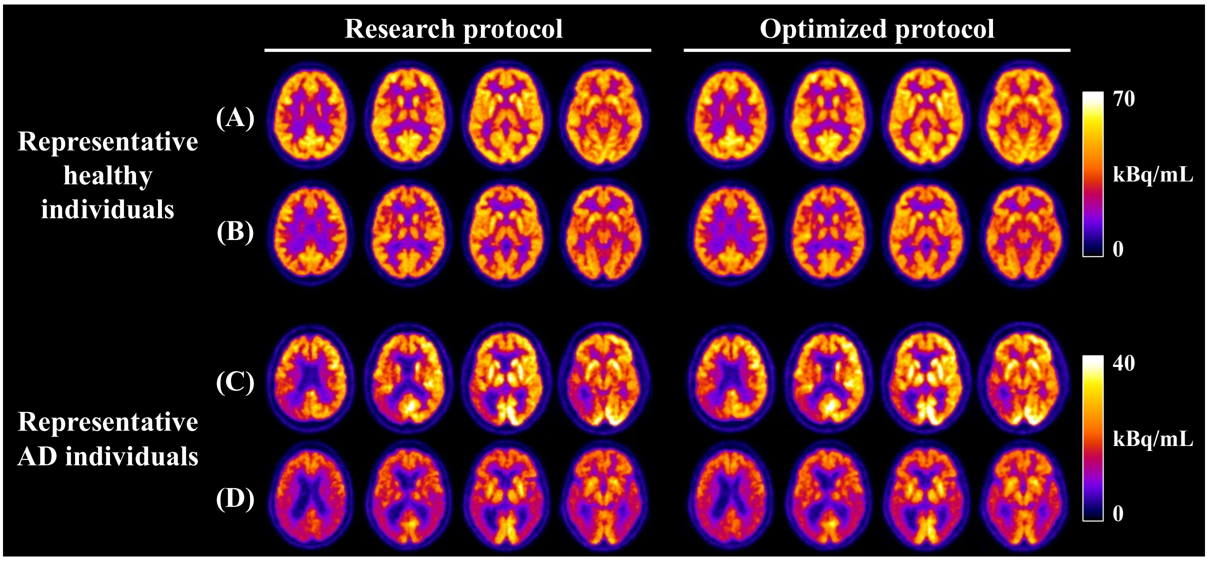

Figure 18: Images reconstructed with the research protocol from two representative subjects from each group (A-B, healthy individuals; C-D, AD patients). For comparison, respective images reconstructed with the optimized protocol are shown on the right columns. Images were normalized to the MNI space with SPM12. Source: (The Author, 2021).

Images reconstructed with both protocols with PSF correction were visually assessed (Table 14). Although no significant differences in scores were observed between the optimized and research protocols, a significantly lower score was assigned to all metrics for the images reconstructed with the PSF correction compared to respective uncorrected images ($p < 0.03$). Our study found that the use of PSF should be avoided in the clinical setting for [^{18}F]FDG, in agreement with the results presented by Prieto et al. (2015). Finally, Figure 19 presents images reconstructed with the research (columns in the left) and optimized (columns in the right) protocols with the PSF correction from two representative subjects from each group.

Table 14: Results of visual assessment for images reconstructed with the optimized and research protocols, both with the PSF correction. Scores (1-5) are presented as mean ± SD (healthy individuals, $n = 17$; AD patients, $n = 18$). Source: (The Author, 2021).

Evaluators	**Metrics**	**Healthy Individuals**		**AD Patients**	
		Optimized protocol (PSF correction)	Research protocol (PSF correction)	Optimized protocol (PSF correction)	Research protocol (PSF correction)
Physician 1	Noise	2.6 ± 0.5	2.5 ± 0.5	1.4 ± 0.6	1.3 ± 0.6
	Contrast	2.6 ± 0.5	2.5 ± 0.5	1.6 ± 0.6	1.4 ± 0.6
	Overall	2.6 ± 0.5	2.5 ± 0.5	1.6 ± 0.6	1.4 ± 0.6
Physician 2	Noise	3.1 ± 0.8	3.4 ± 0.6	2.3 ± 0.6	3.2 ± 0.7
	Contrast	2.1 ± 0.4	2.0 ± 0.0	3.1 ± 0.6	2.1 ± 0.5
	Overall	2.2 ± 0.5	2.0 ± 0.0	2.9 ± 0.7	2.1 ± 0.3

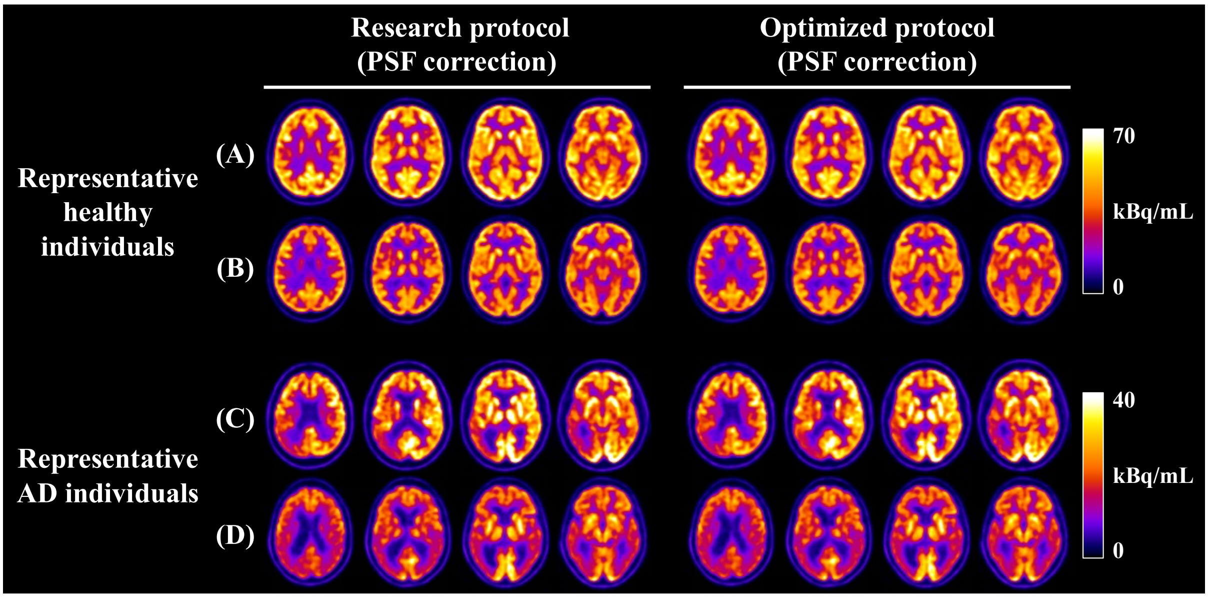

Figure 19: Images reconstructed with the research protocol with the PSF from two representative subjects from each group (A-B, healthy individuals; C-D, AD patients). For comparison, respective images reconstructed with the optimized protocol are shown on the right columns. Images were normalized to the MNI space with SPM12. Source: (The Author, 2021).

7 CONCLUSION

In this study, we proposed a reconstruction optimization strategy aiming to reduce acquisition time (or dose). For this, we acquired [^{18}F]FDG-PET data of an anthropomorphic brain phantom and performed a series of optimization steps followed by a validation study in retrospective [^{18}F]FDG-PET data acquired from healthy individuals and AD patients.

Our strategy to analyze the effect of the time acquisition reduction in image quality and quantification accuracy metrics in the Hoffman 3D brain phantom resulted in optimized reconstruction parameters for the iterative method OSEM with a 50% reduction in acquisition time. The optimized protocol performed similarly to the protocol currently implemented in practice. If the acquisition time remains the same, our results could represent an optimization both in dose costs and radiation protection. Such reduction in acquisition time represents an increase in patient comfort and can help limiting head movements. Finally, although the implementation of the PSF correction improved the spatial resolution of the reconstructed images, this correction proved to degrade image quality, as observed in the visual assessment performed by the experienced nuclear physician.

Our results are in accordance to previous studies that have shown the feasibility of reducing the dose and scanning time in neurological PET imaging studies without affecting diagnostic performance and quantitative assessments (SCHILLER et al., 2019; SHKUMAT; VALI; SHAMMAS, 2020; SORET et al., 2020). In a study with patients with AD and frontotemporal dementia, Schiller et al. (2019) suggested the potential to reduce the typical 10 min acquisition time by a factor of 4 without compromising the quality of diagnosis (SCHILLER et al., 2019). Soret et al. (2020) showed that the advantage of dose reduction is a significant decrease in the patient effective dose, which is non-negligible in longitudinal follow-up studies and research protocols involving healthy volunteers (SORET et al., 2020). Lastly, Shkumat, Vali, and Shammas (2020) showed the feasibility of time (or dose) reduction in the acquisition of [^{18}F]FDG-PET images in studies involving diagnosis, evaluation, and treatment of childhood epilepsy while maintaining the confidence of obtaining diagnostic-quality images (SHKUMAT; VALI; SHAMMAS, 2020).

This study has a few of limitations. First, a single acquisition was used for all reconstructions in the phantom study with a limited number of contrast ratios. Repeating the phantom acquisition and using different phantoms would increase the robustness of the results presented in this study, as the uncertainty of the data has not been measured and statistical analysis was not feasible. Second, different acquisition times were used for the clinical (10 min.) and research (8 min.) protocols. Although differences between clinical and research protocols were not observed, it would be important to confirm our results using human data reconstructed with 10 minutes. Third, the number of updates (iterations-subsets product) was fixed. Future studies could be performed to investigate the impact of different numbers of updates in the reconstructed image. Finally, the retrospective [^{18}F]FDG-PET/CT data collected in a single hospital limits the reach of our results, given that different services have different equipment and clinical protocols. The strategy implemented here could be used by other services to optimize their protocols specifically for their equipment and clinical protocols. Further studies with data from different scanners are needed to confirm our results, and its widespread applicability.

8 REFERENCES

AKAMATSU, G. et al. Improvement in PET/CT Image Quality with a Combination of Point-Spread Function and Time-of-Flight in Relation to Reconstruction Parameters. **Journal of Nuclear Medicine**, v. 53, n. 11, p. 1716–1722, nov. 2012.

AKAMATSU, G. et al. Optimization of image reconstruction conditions with phantoms for brain FDG and amyloid PET imaging. **Annals of Nuclear Medicine**, v. 30, n. 1, p. 18–28, 4 jan. 2016.

AKERELE, M. I. et al. Validation of the physiological background correction method for the suppression of the spill-in effect near highly radioactive regions in positron emission tomography. **EJNMMI Physics**, v. 5, n. 1, p. 34, 5 dez. 2018.

ALESSIO, A. M. et al. Application and Evaluation of a Measured Spatially Variant System Model for PET Image Reconstruction. **IEEE Transactions on Medical Imaging**, v. 29, n. 3, p. 938–949, mar. 2010.

AREVALO-RODRIGUEZ, I. et al. Mini-Mental State Examination (MMSE) for the detection of Alzheimer's disease and other dementias in people with mild cognitive impairment (MCI). **Cochrane Database of Systematic Reviews**, 5 mar. 2015.

ARNOLD, W. E.; MCCROSKEY, J. C.; PRICHARD, S. V. O. The Likert-type scale. **Today's Speech**, v. 15, n. 2, p. 31–33, abr. 1967.

ASSOCIAÇÃO BRASILEIRA DE ALZHEIMER. **O que é Alzheimer**. Disponível em: <http://abraz.org.br/web/sobre-alzheimer/o-que-e-alzheimer/>. Acesso em: 20 out. 2021.

BAILEY, D. L. et al. **Positron Emission Tomography**. London: Springer-Verlag, 2005. v. 2

BANATI, R. B. et al. The peripheral benzodiazepine binding site in the brain in multiple sclerosis. **Brain**, v. 123, n. 11, p. 2321–2337, nov. 2000.

BEHR, S. C. et al. Quantitative and Visual Assessments toward Potential Sub-mSv or Ultrafast FDG PET Using High-Sensitivity TOF PET in PET/MRI. **Molecular Imaging and Biology**, v. 20, n. 3, p. 492–500, 30 jun. 2018.

BERTOLDO, A.; RIZZO, G.; VERONESE, M. Deriving physiological information from PET images: from SUV to compartmental modelling. **Clinical and Translational Imaging**, v. 2, n. 3, p. 239–251, 1 jun. 2014.

BOELLAARD, R. et al. Effects of noise, image resolution, and ROI definition on the accuracy of standard uptake values: a simulation study. **Journal of nuclear medicine : official publication, Society of Nuclear Medicine**, v. 45, n. 9, p. 1519–27, set. 2004.

BOELLAARD, R. Standards for PET Image Acquisition and Quantitative Data Analysis. **Journal of Nuclear Medicine**, v. 50, n. Suppl_1, p. 11S-20S, 1 maio 2009.

BOELLAARD, R.; VAN LINGEN, A.; LAMMERTSMA, A. A. Experimental and clinical evaluation of iterative reconstruction (OSEM) in dynamic PET: quantitative characteristics and effects on kinetic modeling. **Journal of nuclear medicine : official publication, Society of Nuclear Medicine**, v. 42, n. 5, p. 808–17, maio 2001.

BORELLI, W. V. et al. Neural correlates of exceptional memory ability in SuperAgers: A multimodal approach using FDG-PET, PIB-PET, and MRI. **bioRxvi**, n. 666438, 2019.

BOUSSE, A. et al. PET Reconstruction With Non-Negativity Constraint in Projection Space: Optimization Through Hypo-Convergence. **IEEE Transactions on Medical Imaging**, v. 39, n. 1, p. 75–86, jan. 2020.

BRINKS, R.; BUZUG, T. M. Image reconstruction in positron emission tomography (PET): the 90th anniversary of Radon's solution / Bildrekonstruktion in der Positronen-Emissions-Tomographie (PET): zum 90. Jahrestag von Radons Lösung. **Biomedizinische Technik/Biomedical Engineering**, v. 52, n. 6, p. 361–364, dez. 2007.

BRUCKI, S. M. D. et al. Sugestões para o uso do mini-exame do estado mental no Brasil. **Arquivos de Neuro-Psiquiatria**, v. 61, n. 3B, p. 777–781, set. 2003.

BUSHBERG, J. T. **The essential physics of medical imaging**. [s.l.] Lippincott Williams & Wilkins, 2002.

BUVAT, I. Quantification in emission tomography: Challenges, solutions, and performance. **Nuclear Instruments and Methods in Physics Research Section A: Accelerators, Spectrometers, Detectors and Associated Equipment**, v. 571, n. 1–2, p. 10–13, 2007.

BYRNE, C. L. Accelerating the EMML algorithm and related iterative algorithms by rescaled block-iterative methods. **IEEE Transactions on Image Processing**, v. 7, n. 1, p. 100–109, 1998.

CABRERA-MARTÍN, M. N. et al. Validation technique and improvements introduced in a new dedicated brain positron emission tomograph (CareMiBrain). **Revista Española de**

Medicina Nuclear e Imagen Molecular (English Edition), v. 40, n. 4, p. 239–248, jul. 2021.

CARIBE, P. R. R. V. **Evaluation of Image Quality and Reconstruction Parameters in Recent PET-CT and PET-MR Systems**. [s.l.] Ghent University, 2020.

CARLIER, T. et al. 90 Y -PET imaging: Exploring limitations and accuracy under conditions of low counts and high random fraction. **Medical Physics**, v. 42, n. 7, p. 4295–4309, 22 jun. 2015.

CHAUVEAU, F. et al. Nuclear imaging of neuroinflammation: a comprehensive review of [11 C] PK11195 challengers. **European journal of nuclear medicine and molecular imaging**, v. 35, n. 12, p. 2304–2319, 2008.

CHERRY, S. R.; SORENSON, J. A.; PHELPS, M. E. **Physics in nuclear medicine e-Book**. [s.l.] Elsevier Health Sciences, 2012.

COLLIGNON, A. et al. Automated multi-modality image registration based on information theory. **Information processing in medical imaging**, v. 3, n. 6, p. 263–274, 1995.

D’ELLA L.F.; SATZ P.; UCHIYAMA C.L.; WHITE T. **Teste das trilhas coloridas**. 1 ed ed. [s.l: s.n.].

DAHLBOM, M. **Physics of PET and SPECT Imaging**. [s.l.] CRC Press, 2017.

DE ARAÚJO, A. S.; ANDRADE, M. A.; DA SILVA, A. M. M. Efeito de Volume Parcial na Quantificação de Imagens PET de Indivíduos Idosos Saudáveis. **Revista Brasileira de Física Médica**, 2018.

DRZEZGA, A. Diagnosis of Alzheimer’s disease with [18F]PET in mild and asymptomatic stages. **Behavioural neurology**, v. 21, n. 1, p. 101–15, 2009.

DU, Y. et al. Compensation for spill-in and spill-out partial volume effects in cardiac PET imaging. **Journal of Nuclear Cardiology**, v. 20, n. 1, p. 84–98, 14 fev. 2013.

ELLIS, S.; READER, A. J. Penalized maximum likelihood simultaneous longitudinal PET image reconstruction with difference-image priors. **Medical Physics**, v. 45, n. 7, p. 3001–3018, 23 jul. 2018.

ELSE SOLUTIONS S.R.L. **Hoffman 3D Brain**. Disponível em: <https://www.elsesolutions.com/en/prodotti/nuclear-medicine/quality-control/phantoms/hoffman-3d-cerebrale/>. Acesso em: 22 jul. 2020.

FÄLLMAR, D. et al. Validation of true low-dose 18F-FDG PET of the brain. **American**

journal of nuclear medicine and molecular imaging, v. 6, n. 5, p. 269–276, 2016.

FÄLLMAR, D. et al. Z-score maps from low-dose 18F-FDG PET of the brain in neurodegenerative dementia. **American journal of nuclear medicine and molecular imaging**, v. 8, n. 4, p. 239–246, 2018.

FILIPPI, M. et al. EFNS task force: the use of neuroimaging in the diagnosis of dementia. **European Journal of Neurology**, v. 19, n. 12, p. 1487–1501, dez. 2012.

FOLSTEIN, M. F.; FOLSTEIN, S. E.; MCHUGH, P. R. "Mini-mental state". **Journal of Psychiatric Research**, v. 12, n. 3, p. 189–198, nov. 1975.

GE HEALTHCARE. **VUE Point HD: Bringing accuracy to PET reconstruction.** Waukesha: [s.n.].

GONZÁLEZ, J. C.; MOINELO, J. M. U. Aplicación de simulaciones Monte Carlo para el análisis de información CT y su uso en PET y Dosimetria. **Universidad Complutense de Madrid, Madrid**, 2010.

GREZES-BESSET, L. et al. **Simulation-based evaluation of NEG-ML iterative reconstruction of low count PET data**. 2007 IEEE Nuclear Science Symposium Conference Record. **Anais**...IEEE, 2007

HABERT, M.-O. et al. Optimization of brain PET imaging for a multicentre trial: the French CATI experience. **EJNMMI Physics**, v. 3, n. 1, p. 6, 5 dez. 2016.

HAMDAN, A. C.; BUENO, O. F. A. Relações entre controle executivo e memória episódica verbal no comprometimento cognitivo leve e na demência tipo Alzheimer. **Estudos de Psicologia**, v. 10, n. 1, p. 63–71, 2005.

HERHOLZ, K. The role of PET quantification in neurological imaging: FDG and amyloid imaging in dementia. **Clinical and Translational Imaging**, v. 2, n. 4, p. 321–330, 16 ago. 2014.

HOEKSTRA, C. J. et al. Monitoring response to therapy in cancer using [18 F]-2-fluoro-2-deoxy- d -glucose and positron emission tomography: an overview of different analytical methods. **European Journal of Nuclear Medicine and Molecular Imaging**, v. 27, n. 6, p. 731–743, 29 maio 2000.

HUDSON, H. M.; LARKIN, R. S. Accelerated image reconstruction using ordered subsets of projection data. **IEEE transactions on medical imaging**, v. 13, n. 4, p. 601–609, 1994.

HUTTON, C. et al. Quantification of 18F-florbetapir PET: comparison of two analysis methods. **European Journal of Nuclear Medicine and Molecular Imaging**, v. 42, n. 5, p. 725–732, 5 abr. 2015.

IKARI, Y. et al. Phantom criteria for qualification of brain FDG and amyloid PET across different cameras. **EJNMMI Physics**, v. 3, n. 1, p. 23, 6 dez. 2016.

ILLES, J. et al. Prospects for Prediction: Ethics Analysis of Neuroimaging in Alzheimer's Disease. **Annals of the New York Academy of Sciences**, v. 1097, n. 1, p. 278–295, 1 fev. 2007.

IVNIK, R. J. et al. Testing normal older people three or four times at 1- to 2-year intervals: Defining normal variance. **Neuropsychology**, v. 13, n. 1, p. 121–127, 1999.

JIAN, Y.; PLANETA, B.; CARSON, R. E. Evaluation of bias and variance in low-count OSEM list mode reconstruction. **Physics in Medicine and Biology**, v. 60, n. 1, p. 15–29, 7 jan. 2015.

KAPLAN, EDITH; GOODGLASS, HAROLD; WEINTRAUB, S. **The Boston naming test**. 2nd Editio ed. Philadelphia: Lea & Febiger, 1983.

KASTIS, G. A. et al. **Evaluation of a spline reconstruction technique: Comparison with FBP, MLEM and OSEM**. IEEE Nuclear Science Symposuim & Medical Imaging Conference. **Anais**...IEEE, out. 2010Disponível em: <http://ieeexplore.ieee.org/document/5874412/>

KASTIS, G. A. et al. The SRT reconstruction algorithm for semiquantification in PET imaging. **Medical Physics**, v. 42, n. 10, p. 5970–5982, 22 set. 2015.

KREMPSER, A. R.; DE OLIVEIRA, S. M. V.; DE ALMEIDA, S. A. Avaliação do efeito de volume parcial na quantificação de atividade em imagens de PET/CT. **Revista Brasileira de Física Médica**, v. 6, n. 2, p. 35–40, 2012.

LEEMANS, E. L. et al. Qualitative and Quantitative Evaluation of Blob-Based Time-of-Flight PET Image Reconstruction in Hybrid Brain PET/MR Imaging. **Molecular Imaging and Biology**, v. 17, n. 5, p. 704–713, 30 out. 2015.

LIM, H.; DEWARAJA, Y. K.; FESSLER, J. A. A PET reconstruction formulation that enforces non-negativity in projection space for bias reduction in Y-90 imaging. **Physics in**

Medicine & Biology, v. 63, n. 3, p. 035042, 6 fev. 2018.

LIMA, T. V. M. et al. First Phantom-Based Quantitative Assessment of Scandium-44 Using a Commercial PET Device. **Frontiers in Physics**, v. 8, 10 jul. 2020.

MALLOY-DINIZ, L. F. et al. The Rey Auditory-Verbal Learning Test: applicability for the Brazilian elderly population. **Revista Brasileira de Psiquiatria**, v. 29, n. 4, p. 324–329, 3 ago. 2007.

MASTERS, C. L. et al. Alzheimer’s disease. **Nature Reviews Disease Primers**, v. 1, n. 1, p. 15056, 17 dez. 2015.

MINOSHIMA, S. et al. Alzheimer’s disease versus dementia with Lewy bodies: Cerebral metabolic distinction with autopsy confirmation. **Annals of Neurology**, v. 50, n. 3, p. 358–365, set. 2001.

MIOTTO, E. C. et al. Development of an adapted version of the Boston Naming Test for Portuguese speakers. **Revista Brasileira de Psiquiatria**, v. 32, n. 3, p. 279–282, 30 abr. 2010.

MURRAY, I. et al. Time-of-flight PET/CT using low-activity protocols: potential implications for cancer therapy monitoring. **European Journal of Nuclear Medicine and Molecular Imaging**, v. 37, n. 9, p. 1643–1653, 29 ago. 2010.

NAGAKI, A.; ONOGUCHI, M.; MATSUTOMO, N. Clinical validation of high-resolution image reconstruction algorithms in brain 18F-FDG-PET. **Nuclear Medicine Communications**, v. 35, n. 12, p. 1224–1232, dez. 2014.

NEHMEH, S. A. et al. Effect of respiratory gating on reducing lung motion artifacts in PET imaging of lung cancer. **Medical Physics**, v. 29, n. 3, p. 366–371, 21 fev. 2002.

NUGENT, S. et al. Selection of the optimal intensity normalization region for FDG-PET studies of normal aging and Alzheimer’s disease. **Scientific Reports**, v. 10, n. 1, p. 9261, 9 dez. 2020.

NUYTS, J. et al. Reducing loss of image quality because of the attenuation artifact in uncorrected PET whole-body images. **Journal of Nuclear Medicine**, v. 43, n. 8, p. 1054–1062, 2002.

PATTERSON, C. **World Alzheimer Report 2018 - The state of the art of dementia research: New frontiers**. London: [s.n.].

POLYCARPOU, I.; TSOUMPAS, C.; MARSDEN, P. K. Analysis and comparison of two methods for motion correction in PET imaging. **Medical Physics**, v. 39, n. 10, p. 6474–6483, 3 out. 2012.

PORTNOW, L. H.; VAILLANCOURT, D. E.; OKUN, M. S. The history of cerebral PET scanning: From physiology to cutting-edge technology. **Neurology**, v. 80, n. 10, p. 952–956, 5 mar. 2013.

PRIETO, E. et al. Brain PET imaging optimization with time of flight and point spread function modelling. **Physica Medica**, v. 31, n. 8, p. 948–955, dez. 2015.

RAPISARDA, E. et al. Image-based point spread function implementation in a fully 3D OSEM reconstruction algorithm for PET. **Physics in Medicine and Biology**, v. 55, n. 14, p. 4131–4151, 21 jul. 2010.

REYNÉS-LLOMPART, G. et al. Phantom, clinical, and texture indices evaluation and optimization of a penalized-likelihood image reconstruction method (Q.Clear) on a <scp>BGO PET</scp> / <scp>CT</scp> scanner. **Medical Physics**, v. 45, n. 7, p. 3214–3222, 8 jul. 2018.

RIDDELL, C. et al. Noise reduction in oncology FDG PET images by iterative reconstruction: a quantitative assessment. **Journal of nuclear medicine : official publication, Society of Nuclear Medicine**, v. 42, n. 9, p. 1316–23, set. 2001.

SAGARA, H. et al. Optimization of injection dose in 18F-FDG PET/CT based on the 2020 national diagnostic reference levels for nuclear medicine in Japan. **Annals of Nuclear Medicine**, v. 35, n. 11, p. 1177–1186, 21 nov. 2021.

SAHA, G. B. **Basics of PET imaging: physics, chemistry, and regulations**. [s.l.] Springer, 2015.

SARIKAYA, I.; SARIKAYA, A. PET/CT Image Artifacts Caused by the Arms. **Journal of Nuclear Medicine Technology**, v. 49, n. 1, p. 19–22, mar. 2021.

SCHILLER, F. et al. Limits for Reduction of Acquisition Time and Administered Activity in 18 F-FDG PET Studies of Alzheimer Dementia and Frontotemporal Dementia. **Journal of Nuclear Medicine**, v. 60, n. 12, p. 1764–1770, dez. 2019.

SHEIKHBAHAEI, S. et al. Impact of point spread function reconstruction on quantitative 18F-FDG-PET/CT imaging parameters and inter-reader reproducibility in solid tumors. **Nuclear Medicine Communications**, v. 37, n. 3, p. 288–296, mar. 2016.

SHEKARI, M. et al. Quantification of the impact of TOF and PSF on PET images using the noise-matching concept: clinical and phantom study. **Nuclear Science and Techniques**, v. 28, n. 11, p. 167, 30 nov. 2017.

SHKUMAT, N. A.; VALI, R.; SHAMMAS, A. Clinical evaluation of reconstruction and acquisition time for pediatric 18F-FDG brain PET using digital PET/CT. **Pediatric Radiology**, v. 50, n. 7, p. 966–972, 3 jun. 2020.

SHOKOUHI, S.; RIDDLE, W.; KANG, H. A new data analysis approach for measuring longitudinal changes of metabolism in cognitively normal elderly adults. **Clinical Interventions in Aging**, v. Volume 12, p. 2123–2130, dez. 2017.

SLOMKA, P. J. et al. Advances in technical aspects of myocardial perfusion SPECT imaging. **Journal of Nuclear Cardiology**, v. 16, n. 2, p. 255–276, 26 abr. 2009.

SNYDER, D. L. et al. Noise and Edge Artifacts in Maximum-Likelihood Reconstructions for Emission Tomography. **IEEE Transactions on Medical Imaging**, v. 6, n. 3, p. 228–238, set. 1987.

SORET, M. et al. Dose Reduction in Brain [18F]FDG PET/MRI: Give It Half a Chance. **Molecular Imaging and Biology**, v. 22, n. 3, p. 695–702, 8 jun. 2020.

SORET, M.; BACHARACH, S. L.; BUVAT, I. Partial-Volume Effect in PET Tumor Imaging. **Journal of Nuclear Medicine**, v. 48, n. 6, p. 932–945, 1 jun. 2007.

TAHAEI, M. S.; READER, A. J.; COLLINS, D. L. Two novel PET image restoration methods guided by PET-MR kernels: Application to brain imaging. **Medical Physics**, v. 46, n. 5, p. 2085–2102, 12 maio 2019.

TARANTOLA, G.; ZITO, F.; GERUNDINI, P. PET instrumentation and reconstruction algorithms in whole-body applications. **Journal of Nuclear Medicine**, v. 44, n. 5, p. 756–769, 2003.

TONG, S.; ALESSIO, A. M.; KINAHAN, P. E. Noise and signal properties in PSF-based fully 3D PET image reconstruction: an experimental evaluation. **Physics in Medicine and Biology**, v. 55, n. 5, p. 1453–1473, 7 mar. 2010a.

TONG, S.; ALESSIO, A. M.; KINAHAN, P. E. Image reconstruction for PET/CT scanners: past achievements and future challenges. **Imaging in Medicine**, v. 2, n. 5, p. 529–545, out. 2010b.

TORRICO, E. V. **Caracterización, mejora y diseño de escáneres PET preclinicos**. Madri: Universidad Complutense de Madrid, 2012.

VAN SLAMBROUCK, K. et al. Bias Reduction for Low-Statistics PET: Maximum Likelihood Reconstruction With a Modified Poisson Distribution. **IEEE Transactions on Medical Imaging**, v. 34, n. 1, p. 126–136, jan. 2015.

VANHOUTTE, M. et al. Using EQ·PET to reduce reconstruction-dependent variations in [18 F]FDG-PET brain imaging. **Physics in Medicine & Biology**, v. 64, n. 17, p. 175002, 28 ago. 2019.

VENNART, N. J. et al. Optimization of PET/CT image quality using the GE 'Sharp IR' point-spread function reconstruction algorithm. **Nuclear Medicine Communications**, v. 38, n. 6, p. 471–479, jun. 2017.

VERHAEGHE, J.; READER, A. J. AB-OSEM reconstruction for improved Patlak kinetic parameter estimation: a simulation study. **Physics in Medicine and Biology**, v. 55, n. 22, p. 6739–6757, 21 nov. 2010.

VISVIKIS, D. et al. **Evaluation of respiratory motion effects in comparison with other parameters affecting PET image quality**. IEEE Symposium Conference Record Nuclear Science 2004. **Anais**...IEEE, dez. 2004

WALKER, M. D. et al. Bias in iterative reconstruction of low-statistics PET data: benefits of a resolution model. **Physics in Medicine and Biology**, v. 56, n. 4, p. 931–949, 21 fev. 2011.

WAMPL, S. et al. Quantification accuracy of neuro-oncology PET data as a function of emission scan duration in PET/MR compared to PET/CT. **European Journal of Radiology**, v. 95, p. 257–264, out. 2017.

WARDAK, M. et al. Movement Correction Method for Human Brain PET Images: Application to Quantitative Analysis of Dynamic 18F-FDDNP Scans. **Journal of Nuclear Medicine**, v. 51, n. 2, p. 210–218, 1 fev. 2010.

WEINER, M. W. et al. Recent publications from the Alzheimer's Disease Neuroimaging Initiative: Reviewing progress toward improved AD clinical trials. **Alzheimer's & Dementia**, v. 13, n. 4, p. e1–e85, abr. 2017.

XU, Q.; YUAN, K.; YE, D. Respiratory motion blur identification and reduction in ungated thoracic PET imaging. **Physics in Medicine and Biology**, v. 56, n. 14, p. 4481–4498, 21 jul. 2011.

YAN, J. et al. A method to assess image quality for Low-dose PET: analysis of SNR, CNR, bias and image noise. **Cancer Imaging**, v. 16, n. 1, p. 26, 26 dez. 2016.

YITZHAKY, Y.; KOPEIKA, N. S. Identification of Blur Parameters from Motion Blurred Images. **Graphical Models and Image Processing**, v. 59, n. 5, p. 310–320, set. 1997.

YODER, K., K. Basic PET Data Analysis Techniques. In: **Positron Emission Tomography - Recent Developments in Instrumentation, Research and Clinical Oncological Practice**. [s.l.] InTech, 2013. p. 63–80.

APPENDIX A

Paper “Optimization of reconstruction parameters in [^{18}F]FDG-PET brain images aiming scan time reduction” published in Revista Brasileira de Física Médica, 2020.

Optimization of reconstruction parameters in [^{18}F]FDG-PET brain images aiming scan time reduction

Otimização de parâmetros de reconstrução de imagens PET cerebrais adquiridas com [^{18}F]FDG visando a redução do tempo de exame

Samara Pinto[1], Paulo R. R. V. Caribe[1,2], Lucas Narciso[1,3], Ana Maria Marques da Silva[1]
[1]Medical Image Computing Laboratory (MEDICOM), PUCRS, Porto Alegre, Brazil
[2]Medical Imaging and Signal Processing (MEDISIP), Ghent University, Ghent, Belgium
[3]Department of Medical Biophysics, Western University, London, Canada

Abstract

Iterative image reconstruction methods are widely used in PET due to their better image quality when compared to analytical methods. However, inaccurate quantification occurs in low activity concentration regions, which leads to biased quantification of PET images. The diagnosis of some neurodegenerative diseases, such as Alzheimer’s disease, is based on identifying such low-uptake regions. Furthermore, PET imaging in these populations should be as short as possible to limit head movements and improve patient comfort. This work aims to identify optimized reconstruction parameters of [^{18}F]FDG-PET brain images aiming to reduce image acquisition time with minimal impact on quantification. For this, [^{18}F]FDG-PET images of a Hoffman 3D brain phantom were acquired. Analytical and iterative reconstruction methods were compared utilizing image quality and quantitative accuracy metrics. OSEM reconstruction algorithm was optimized (4 iterations and 32 subsets). It resulted in remarkably similar images compared to the current clinical settings, with a 50% reduction in scan time (5 min with a post-reconstruction filter of 4 mm). Future clinical studies are needed to confirm the results presented here.

Keywords: *brain PET; reconstruction; optimization; quantification; image quality; Hoffman*

Resumo

Os métodos de reconstrução de imagens PET mais empregados são os iterativos, pois proporcionam uma imagem de melhor qualidade comparada com os métodos analíticos. No entanto, uma quantificação inadequada ocorre em regiões de baixa concentração de atividade, que levam a erros de quantificação das imagens PET. O diagnóstico de algumas doenças neurodegenerativas, como a doença de Alzheimer, é baseado na identificação de regiões de baixa captação. Além disso, o exame de PET para essas populações devem ser o mais curto possível, para limitar movimentos e melhorar o conforto do paciente. Este trabalho tem como objetivo identificar parâmetros de reconstrução otimizados de imagens cerebrais PET com [^{18}F]FDG visando reduzir o tempo de aquisição com mínimo impacto na quantificação. Para tanto, foram adquiridas imagens PET do fantoma cerebral 3D Hoffman, com [^{18}F]FDG. Métodos de reconstrução analíticos e iterativos foram comparados para analisar a qualidade da imagem e as métricas de exatidão quantitativa. O algoritmo de reconstrução OSEM foi otimizado (4 iterações e 32 subsets) e resultou em imagens notavelmente similares àquelas obtidas com o padrão clínico atual, para uma redução de 50% no tempo de exame (5 min, com um filtro de pós-reconstrução de 4 mm). Estudos clínicos futuros são necessários para confirmar os resultados apresentados aqui.

Palavras-chave: *PET cerebral; reconstrução; otimização; quantificação; qualidade de imagem; Hoffman*

1. Introduction

Nuclear medicine is a medical imaging modality, often non-invasive, that provides metabolic and functional information *in vivo* in the format of dynamic or static images, representing the volumetric distribution of radiopharmaceuticals (1). Positron emission tomography (PET) is an imaging modality within nuclear medicine that uses positron emitter radiotracers and has excellent applicability in oncology, cardiology and neurology (2).

For decades, PET brain imaging has been widely used to study brain disorders, such as neurodegenerative diseases, dementia, epilepsy, neurodevelopmental and psychic disorders (3–5). Diagnosis of brain disorders with PET is accomplished by using specific radiotracers and analyzing brain activity (6). One of the most commonly used radiotracers, fluorodeoxyglucose labelled with ^{18}F ([^{18}F]FDG), can provide early signs of neuronal changes(7). [^{18}F]FDG is an irreversibly bound tracer that provides direct or indirect measurements of glucose consumption, thus energy production, such as the cerebral metabolic rate of glucose (8). Several studies have reported the possibility of using low activity injection for different PET radiotracers (9–14).

An increase in dementia cases in the elderly population is expected, which brings the need for better ways to detect and prevent symptoms earlier. In ageing, cognitive decline is typical, and it is usually aggravated by some neurodegenerative disease, such as Alzheimer's Disease (AD) (15). AD is characterized by progressive impairment, affecting cognition, memory and executive functions (15). In AD, low-uptake regions in [^{18}F]FDG-PET brain images are due to glucose metabolism impairment caused by neuronal loss (6). Thus, to assist in AD diagnosis, physicians use an uptake quantification tool and look for regions that present a reduced metabolic rate of glucose (low-uptake regions) (4).

PET image quantification of low-uptake regions is challenging, mainly due to low signal-to-noise ratio (SNR) and partial volume effects that affect the detectability of small lesions (4,9,16). However, the reliability of quantification can be improved during image reconstruction by using iterative reconstruction techniques (1,17,18). The most widely used iterative reconstruction algorithm is the ordered subset expectation maximization (OSEM). An advantage of this algorithm is the ability to better model the emission and detection process. The effects of attenuation, detector normalization, and contamination by scattering and randoms are corrected in the reconstruction algorithm (19). In specific for the AD population, a reduction in scan time is essential to limit head movements, impacting quantification and increasing patient comfort (19,20).

This work aims to identify optimized reconstruction parameters of [^{18}F]FDG-PET brain images aiming to reduce image acquisition time with minimal impact on quantification. For this, [^{18}F]FDG-PET images were acquired of a Hoffman 3D brain phantom, and image quality parameters and quantitative accuracy were evaluated for different reconstruction settings.

2. Materials and Methods

Data were acquired in a PET/computed tomography (CT) scanner (General Electric Medical System, Discovery 600; bismuth germanium oxide detector crystals) at the Brain Institute (BraIns), Porto Alegre, Brazil. This study was conducted by acquiring images from the Hoffman 3D brain phantom.

[^{18}F]FDG-PET images were acquired in a Hoffman 3D anthropomorphic brain simulator (Figure 1). This phantom consists of 40 acrylic slices (variable thickness, maximum of 3.0 mm) with a shape that simulates the regions of activity distribution. The different thicknesses produce a gray-to-white matter ratio (contrast) of 4:1.

Figure 1. Hoffman 3D brain phantom consists of a cylinder with 40 independent cross-sections. Source: BIODEX (2021).

PET data were acquired in list-mode (10 min) after the injection of 37 MBq of [^{18}F]FDG (25.6 kBq/ml). For comparison, the [^{18}F]FDG activity usually injected in the clinic ranges from 5 to 20 mCi (185 to 740 MBq) (21), and approximately 8% of the injected activity is absorbed by the brain (22). Thus, the resulting brain activity concentration ranges from 10 to 42 kBq/mL (considering an average brain weight and density of 1.3 kg (23) and 1.08 g/mL (24), respectively.

Images were obtained with the standard reconstruction algorithm for comparison: OSEM (300- mm FOV, 8 iterations, 16 subsets, 3.0-mm full-width half-maximum (FWHM) post-reconstruction smoothing filter, 192×192 voxels image matrix, 16-bits per pixel, 0.640 pixels/mm resolution, 1.56×1.56 mm^2 pixel size, and 47 axial slices of 3.27 mm thickness), as recommended by the manufacturer and used as the clinical settings for brain images at BraIns. The OSEM iterative reconstruction method is commercially known as Vue-Point HD® and consists of implementing the 3D-maximum likelihood-OSEM algorithm with all the corrections incorporated during the iterative process (25).

Attenuation correction was applied using a CT- based map acquired before PET. Further corrections required for quantification (detector normalization, data rebinning, decay, dead-time, scatter, and random incidences) were also applied. Static PET images are presented in a single frame and represent the average radioactive concentration for a given time interval. In this study, static PET images were generated using 10 min, 5 min, 2.5 min, and 1 min post-acquisition start.

2.1. Quantitative accuracy

Quantification accuracy were evaluated by measurements of RC, gray-to-white matter activity concentration ratio (contrast) and bias. The measurements were obtained by automatically generating volumes-of-interest (VOIs) in the structural image (CT) and transferring them to the static PET images.

The measured-to-true activity concentration ratio, also known as RC Eq. (1), represents the fraction of the true activity concentration (C_{true}) present in the final image. C_{true} (in Bq/mL) is calculated as the injected activity divided by the volume of water in the phantom, after correcting for decay and residual activity in the syringe.

$$RC = \frac{C_{VOI}}{C_{true}} \quad (1)$$

where C_{VOI} is the measured activity concentration (in Bq/mL) in a VOI. Finally, gray-to-white matter activity concentration ratio were calculated using Eq. (2). In this study, this measurement was referred to as contrast, as the WM was considering the background region.

$$Contrast = \frac{C_{GM}}{C_{WM}} \tag{2}$$

Quantification bias describes the difference between measured and expected activity concentrations. In this work, the percentage difference relative to the expected activity concentration at full statistics count-level (10 min) is used to estimate bias (YAN et al., 2016), as given by Eq. (3):

$$Bias\ (\%) = 100 * \frac{C_{meas} - C_{exp}}{C_{exp}} \tag{3}$$

where C_{meas} represents the measured mean activity concentration in a VOI, and C_{exp} the expected activity concentration.

2.2. Image Quality

Additionally, the image quality was assessed by means of noise, coefficient of variation (COV), SNR, and CNR. The measurements were obtained by automatically generating volumes-of-interest (VOIs) in the structural image (CT) and transferring them to the static PET images.

Image quality can be assessed using measurements such as COV, SNR, and CNR. The former is defined as the STD from GM voxel-wise activity concentration. Data variability can be measured by the COV, which is calculated as the ratio between the STD and the mean activity concentration. Finally, SNR and CNR are given by Eqs. (4) and (5), respectively. The latter is related to the visual ability to detect a small lesion (CARLIER et al., 2015).

$$SNR = \frac{C_{GM} - C_{WM}}{STD_{WM}} \tag{4}$$

$$CNR = \frac{RC}{COV} \tag{5}$$

where C_{GM} and C_{WM} are the GM and WM mean activity concentrations, respectively; and STD_{WM} is the WM standard deviation, which is considered the background region.

2.3. Comparison between reconstruction algorithms

In order to compare the analytical and iterative reconstruction methods available in the workstation at BraIns, PET images were reconstructed with different parameters and algorithms. First, [^{18}F]FDG-PET images from the brain simulator were reconstructed as follows:

i. OSEM (VUE Point HD®, 8 iterations, 16 subsets, 3.0-mm FWHM post-reconstruction smoothing filter, clinical protocol)

ii. Fourier rebinning (FORE) + filtered back projection (FBP) (enhanced Hanning smoothing filter, 4.8mm cutoff frequency) and

iii. FBP (enhanced Hanning smoothing filter)

Standard parameters were used for all reconstruction methods, changing only the acquisition time: 10 min, 5 min, 2.5 min, and 1 min. In this phase, the type of algorithm (analytical or iterative) and acquisition time (1 to 10 min) were evaluated by quantification measurements and image quality parameters.

2.4. Optimization of reconstruction parameters

In this part of the study, [^{18}F]FDG-PET images were additionally reconstructed with 4 iterations and 32 subsets. For these settings, we kept the same iterations-subsets product (updates) as the clinical protocol. For the new combination of iterations and subsets, static images were generated for 10 min, 5min, 2.5min, and 1min acquisition times, and different values of the post-smoothing FWHM filter (0 to 10 mm) were used. Quantification measurements and image quality parameters were obtained. Results were compared to the standard reconstruction using the same values of the post-smoothing filter (FWHM varying from 0 to 10 mm).

3. Results and Discussion

3.1. Brain Segmentation

Brain VOIs were automatically created from the CT image using in-house MATLAB® scripts (R2020a, *The MathWorks, Inc.*) by segmenting the GM (270 cm^3) and WM (160 cm^3) compartments of the brain phantom. The Hoffman 3D brain phantom CT acquisition had a total of 47 slices, from which slices 12 to 28 (center of the phantom) were used to create the masks used in the PET data extraction. Figure 2 shows the GM and WM masks created with our MATLAB® scripts. The results presented in this work were extracted using the eroded versions of these masks.

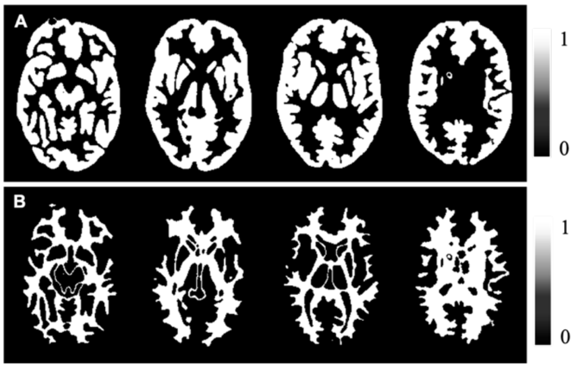

Figure 2. (A) GM and (B) WM masks (binary images) obtained by segmenting the CT image using in-house MATLAB® scripts.

3.1. Comparison between reconstruction algorithms

The reconstruction method OSEM presented the highest SNR (Figure 3A), the lowest quantification bias (Figure 3B) and GM-COV (Figure 3C), when compared to FORE+FBP and FBP for all acquisition times. The COV is less affected by the reconstruction method than by acquisition time. Signal-to-noise ratio and noise estimates for the 5 min reconstructions are similar to those obtained from the 10 min images, with less than 1% difference. SNR results from images reconstructed with OSEM were fairly constant (around 3%) for acquisition times ranging from 2.5 min to 10 min. Quantification bias decreases with the acquisition time, but all three methods presented values lower than 0.7% for 5 min. These results suggest that 5 min would be an adequate choice of acquisition time when compared to the current clinical settings available on this equipment.

3.2. Optimization of reconstruction parameters

Figure 4 shows the result of CNR for the images reconstructed using OSEM with 4 iterations and 32 subsets for a range of post-reconstruction smoothing filter FWHMs (0 = no filter to 10 mm), and acquisition times (1 to 10 min). For comparison, the result from the clinical standard OSEM reconstruction is shown as a point (asterisk), and results for the standard clinical reconstruction for post- reconstruction smoothing filter FWHMs ranging from 0 to 10 mm are shown as a dashed line. The CNR shown in Figure 4 is maximum when the post-reconstruction smoothing filter FHWM ranges from 3 to 6 mm and is comparable to the clinical protocol for all filters (dashed line) for the 5-min acquisition time.

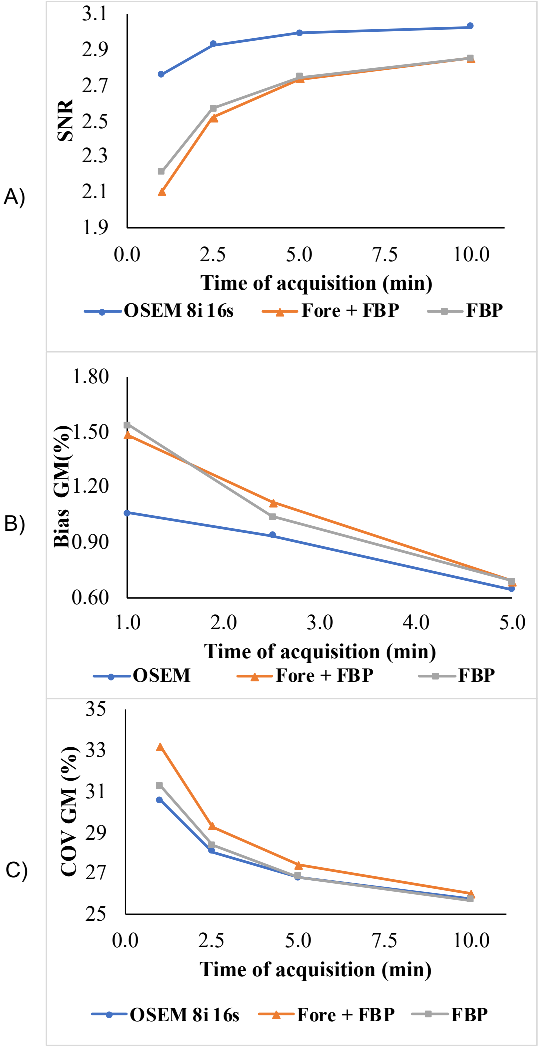

Figure 3. Results of (A) SNR, (B) GM bias (%) and (C) GM- COV (%) measurements for the reconstruction methods (OSEM, FORE+FBP, and FBP), as a function of the acquisition time.

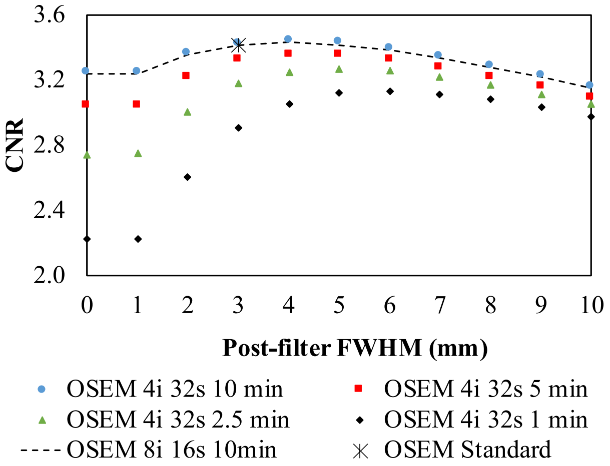

Figure 4. Results of CNR for the OSEM iterative reconstruction method (4 iterations, 32 subsets), plotted as a function of post- reconstruction smoothing filter FWHM. The star point represents the results of the clinical protocol (OSEM, 8 iterations, 16 subsets, 3 mm post-filter FWHM), and the dashed line represent the results of OSEM 8 iterations, 16 subsets 0 to 10 mm post- reconstruction smoothing filter FWHM.

Furthermore, when aiming for a 50% reduction in scan time, images smoothed with a post- reconstruction filter FWHM of 4mm yielded the maximum CNR results (3.4, approximately 2% less than the current clinical settings). Estimates of RC, GM-COV and SNR were comparable between the 5- min reconstruction (4 mm; 0.877, 26.2%, and 2.97, respectively) and the clinical reconstruction parameters (0.880, 25.8%, and 3.02, respectively). Quantification bias for the OSEM reconstruction method with 4 iterations and 32 subsets was -0,3% when images were reconstructed with 5 min and smoothed with a post-reconstruction filter FWHM of 4 mm.

Moreover, the contrast was comparable between the 5-min reconstruction with post-reconstruction smoothing filter FWHM of 4 mm (2.37) and the clinical reconstruction parameters (2.40). Leemans *et al.* (2015) obtained values of contrast ranging from 2.7 to 3.5, which were directly proportional to the number of iterations when reconstructed using OSEM with 1 to 12 iterations (32 subsets and 45 min acquisition time)[26]. In a multicenter study (22 PET centres), Habert *et al.*(2016) obtained values of contrast of 3.0 ± 0.3 (range: 2.34 to 3.77; 3 × 5 min dynamic image) for different equipment and routine iterative reconstruction methods[27]. The lower contrast obtained in this study was likely due to the shorter image acquisition and differences in equipment and vendor-specific reconstruction algorithms.

A post-reconstruction smoothing filter FWHM of 4 mm was chosen for [^{18}F]FDG-PET images reconstructed with a 5-min scan based on the results presented here. Such choice was confirmed by the remarkable similarity between the standard clinical protocol (Figure 5A) and images reconstructed with the optimized OSEM parameters (Figure 5B; the percentual difference map is shown in Figure 5C).

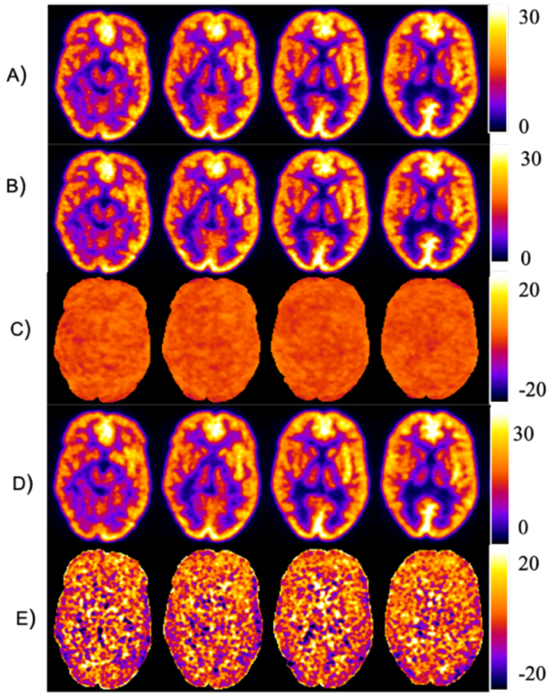

Figure 5. Visual comparison of [18F]FDG-PET images of the Hoffman 3D brain simulator reconstructed with (A) the clinical standard (OSEM, 8 iterations, 16 subsets, 3-mm FWHM, 10- min) and (B) the optimized protocol for a 5 min acquisition time (OSEM, 4 iterations, 32 subsets, 4-mm FWHM. The colorbar represents activity concentration (in kBq/mL). Images in line (C) show the percentual difference between (A) and (B).

Previous studies have shown the feasibility of reducing the dose and scanning time in neurological PET imaging studies without affecting diagnostic performance and quantitative assessments (11,26,28–31). In a study with patients with AD and frontotemporal dementia, Schiller *et al.* (2019) suggested the potential to reduce the typical 10 min acquisition time by a factor of 4 without compromising the quality of diagnosis (28). Soret *et al.* (2020) showed that the advantage of dose reduction is a significant decrease in the patient effective dose, which is non-negligible in longitudinal follow-up studies and in research protocols involving healthy volunteers (11). Lastly, Shkumat, Vali and Shammas (2020) showed the feasibility of time (or dose) reduction in the acquisition of [^{18}F]FDG-PET images in studies involving diagnosis, evaluation, and treatment of childhood epilepsy while maintaining the confidence of obtaining diagnostic-quality images (29).

Limitations of this study include the acquisition of [^{18}F]FDG-PET/CT data in a single hospital and a limited number of contrast ratios. Further studies, including a variety of equipment and reconstruction settings, and the use of a phantom that allows for a range of contrast ratios, are needed to confirm the results presented here (32). Furthermore, there is a restriction concerning the use a ^{18}F-tracer only, given that the use of higher positron energy radioisotopes would have led to statistical uncertainties due to the random nature of radioactive emissions (33). Additionally, the effect of including a point-spread function correction into the OSEM reconstruction algorithm will be evaluated.

Finally, we are currently investigating the feasibility of reducing the acquisition time by comparing the optimized OSEM parameters with the standard clinical settings. For this, retrospective [^{18}F]FDG-PET data from a clinical study that included individuals with AD will be used (previously approved by the Ethics Committee, CAAE: 00919018.6.0000.5336).

4. Conclusion

Our strategy to analyze the effect of the acquisition time reduction in image quality and quantification metrics in the Hoffman 3D brain phantom resulted in optimized OSEM reconstruction settings: 4 iterations, 32 subsets and 4 mm post-reconstruction smoothing filter FWHM for a 5 min acquisition time. The 5 min acquisition represents a 50% reduction in imaging time when compared to the standard clinical protocol. With this acquisition time, our results could represent an optimization both in dose costs and radiation protection. The reduction in scan time is significant for patients with neurodegenerative diseases, which results in an increase in patient comfort and limits the image artifacts produced by head movements.

Acknowledgement

This study was financed in part by the Coordenação de Aperfeiçoamento de Pessoal de Nível Superior – Brasil (CAPES) – Finance Code 001 and by CAPES- PRINT-PUCRS.

References

1. Saha GB. Basics of PET imaging: physics, chemistry, and regulations. Springer; 2015.
2. Cherry S, Sorenson J, Phelps M. Physics in Nuclear Medicine. 2012. 523 p.
3. Chauveau F, Boutin H, Van Camp N, Dollé F, Tavitian B. Nuclear imaging of neuroinflammation: a comprehensive review of [11 C] PK11195 challengers. Eur J Nucl Med Mol Imaging. 2008;35(12):2304–19.
4. de Araújo AS, Andrade MA, da Silva AMM. Efeito de Volume Parcial na Quantificação de Imagens PET de Indivíduos Idosos Saudáveis. Rev Bras Física Médica. 2018;
5. Banati RB, Newcombe J, Gunn RN, Cagnin A, Turkheimer F, Heppner F, et al. The peripheral benzodiazepine binding site in the brain in multiple sclerosis. Brain [Internet]. 2000 Nov;123(11):2321–37. Available from: https://academic.oup.com/brain/article- lookup/doi/10.1093/brain/123.11.2321
6. Jeckel CMM. O uso da Tomografia por Emissão de Pósitrons (pet) no diagnóstico das doenças neurodegenerativas do idoso. PAJAR - Pan Am J Aging Res. 2017 Aug;5(1):1.
7. Shokouhi S, Riddle W, Kang H. A new data analysis approach for measuring longitudinal changes of metabolism in cognitively normal elderly adults. Clin Interv Aging. 2017 Dec;Volume 12:2123–30.
8. Prando S, Ono CR, Robilotta CC, Sapienza MT. Methods for quantification of cerebral glycolytic metabolism using 2-deoxy- 2-[18 F]fluoroglucose in small animals. Res Biomed Eng. 2018 Sep;34(3):254–72.
9. Lim H, Dewaraja YK, Fessler JA. A PET reconstruction formulation that enforces non-negativity in projection space for bias reduction in Y-90 imaging. Phys Med Biol. 2018 Feb;63(3):035042.
10. Jian Y, Planeta B, Carson RE. Evaluation of bias and variance in low-count OSEM list mode reconstruction. Phys Med Biol. 2015 Jan;60(1):15–29.
11. Soret M, Piekarski E, Yeni N, Giron A, Maisonobe J-A, Khalifé M, et al. Dose Reduction in Brain [18F]FDG PET/MRI: Give It Half a Chance. Mol Imaging Biol. 2020 Jun;22(3):695–702.
12. Carlier T, Willowson KP, Fourkal E, Bailey DL, Doss M, Conti M. 90 Y -PET imaging: Exploring limitations and accuracy under conditions of low counts and high random fraction. Med Phys. 2015 Jun;42(7):4295–309.

13. Yan J, Schaefferkoetter J, Conti M, Townsend D. A method to assess image quality for Low-dose PET: analysis of SNR, CNR, bias and image noise. Cancer Imaging. 2016 Dec;16(1):26.

14. Grezes-Besset L, Nuyts J, Boellard R, Buvat I, Michel C, Pierre C, et al. Simulation-based evaluation of NEG-ML iterative reconstruction of low count PET data. In: 2007 IEEE Nuclear Science Symposium Conference Record. IEEE; 2007. p. 3009–14.

15. Hamdan AC, Bueno OFA. Relações entre controle executivo e memória episódica verbal no comprometimento cognitivo leve e na demência tipo Alzheimer. Estud Psicol. 2005;10(1):63–71.

16. Krempser AR, de Oliveira SMV, de Almeida SA. Avaliação do efeito de volume parcial na quantificação de atividade em imagens de PET/CT. Rev Bras Física Médica. 2012;6(2):35– 40.

17. Buvat I. Quantification in emission tomography: Challenges, solutions, and performance. Nucl Instruments Methods Phys Res Sect A Accel Spectrometers, Detect Assoc Equip [Internet]. 2007 Feb [cited 2015 Dec 21];571(1–2):10–3. Available from: http://linkinghub.elsevier.com/retrieve/pii/S0168900206018158

18. Boellaard R. Standards for PET Image Acquisition and Quantitative Data Analysis. J Nucl Med [Internet]. 2009 May 1 [cited 2017 Jul 9];50(Suppl_1):11S-20S. Available from: http://www.ncbi.nlm.nih.gov/pubmed/19380405

19. Tong S, Alessio AM, Kinahan PE. Image reconstruction for PET/CT scanners: past achievements and future challenges. Imaging Med. 2010 Oct;2(5):529–45.

20. lles J, Rosen A, Greicius M, Racine E. Prospects for Prediction: Ethics Analysis of Neuroimaging in Alzheimer's Disease. Ann N Y Acad Sci. 2007 Feb;1097(1):278–95.

21. Wardak M, Wong K-P, Shao W, Dahlbom M, Kepe V, Satyamurthy N, et al. Movement Correction Method for Human Brain PET Images: Application to Quantitative Analysis of Dynamic 18F-FDDNP Scans. J Nucl Med. 2010 Feb;51(2):210–8.

22. Waxman, A. D., Herholz, K., Lewis, D. H., Herscovitch, P., Minoshima, S., Mountz, J. M., & Consensus GID. Guideline for FDG PET Brain Imaging. 2009.

23. ICRP. ICRP Publication 106: Radiation Dose to Patients from Radiopharmaceuticals: A third amendment to ICRP Publication 53. 2008.

24. Dekaban, Anatole S.; Sadowsky D. Changes in brain weights during the span of human life: relation of brain weights to body heights and body weights. Ann Neurol Off J Am Neurol Assoc Child Neurol Soc. 1978;4(4):345–56.

25. Barber TW, Brockway JA, Higgins LS. The density of tissues in and about the head. Acta Neurol Scand. 1970 Mar;46(1):85–92.

26. GE HEALTHCARE. VUE Point HD: Bringing accuracy to PET reconstruction. Waukesha; 2008.

27. Leemans EL, Kotasidis F, Wissmeyer M, Garibotto V, Zaidi H. Qualitative and Quantitative Evaluation of Blob-Based Time- of-Flight PET Image Reconstruction in Hybrid Brain PET/MR Imaging. Mol Imaging Biol. 2015 Oct;17(5):704–13.

28. Habert M-O, Marie S, Bertin H, Reynal M, Martini J-B, Diallo M, et al. Optimization of brain PET imaging for a multicentre trial: the French CATI experience. EJNMMI Phys. 2016 Dec;3(1):6.

29. Schiller F, Frings L, Thurow J, Meyer PT, Mix M. Limits for Reduction of Acquisition Time and Administered Activity in 18 F-FDG PET Studies of Alzheimer Dementia and Frontotemporal Dementia. J Nucl Med. 2019 Dec;60(12):1764–70.

30. Shkumat NA, Vali R, Shammas A. Clinical evaluation of reconstruction and acquisition time for pediatric 18F-FDG brain PET using digital PET/CT. Pediatr Radiol. 2020 Jun;50(7):966–72.

31. Fällmar D, Lilja J, Kilander L, Danfors T, Lubberink M, Larsson E-M, et al. Validation of true low-dose 18F-FDG PET of the brain. Am J Nucl Med Mol Imaging. 2016;6(5):269–76.

32. Shan ZY, Leiker AJ, Onar-Thomas A, Li Y, Feng T, Reddick WE, et al. Cerebral glucose metabolism on positron emission tomography of children. Hum Brain Mapp. 2014 May;35(5):2297–309.

33. Caribé PRR V., Koole M, D'Asseler Y, Van Den Broeck B, Vandenberghe S. Noise reduction using a Bayesian penalized-likelihood reconstruction algorithm on a time-of- flight PET-CT scanner. EJNMMI Phys. 2019 Dec;6(1):22.

34. Caribé PRR V., Koole M, D'Asseler Y, Deller TW, Van Laere K, Vandenberghe S. NEMA NU 2–2007 performance characteristics of GE Signa integrated PET/MR for different PET isotopes. EJNMMI Phys. 2019 Dec;6(1):11.

Contact:
Samara Oliveira Pinto
MEDICOM, PUCRS
Avenida Ipiranga, 6681-Partenon, Porto Alegre, Brasil CEP 90619-900
samara.pinto@edu.pucrs.br